# Effects of Surface Structure on the Electrocatalytic Activity of Pt-based Nanoparticles: An X-ray Absorption Spectroscopy Study

by

Paul Nicholson Duchesne

Submitted in partial fulfilment of the requirements
for the degree of Doctor of Philosophy

at

Dalhousie University
Halifax, Nova Scotia
September 2016

# Table of Contents

# List of Tables

# List of Figures

## Abstract

With clean and renewable sources of energy being a major focus for modern societies, developing efficient means of energy storage is a necessity. Of the technologies currently available, electrochemical fuel cells stand to benefit most from advances in nanomaterials research, due to their reliance on (often Pt-based) electrode catalysts. Perhaps the greatest advantages of using nanoparticle electrode catalysts is their large specific surface area.

While structural characterization of nanoparticles (particularly their surface structure) can be a significant challenge, the use of X-ray absorption spectroscopy (XAS) can allow researchers to study samples beyond the scope of other techniques. Herein, a series of Pt-based nanoparticles is characterized through a combination of XAS techniques and other complementary methods of analysis in order to study the relationships between their surface structure and electrocatalytic activity.

Following a brief exploratory study on the ability of XAS techniques to elucidate the structure of few-atom Pt nanoclusters, focus is shifted to the preparation and electrocatalytic application of bimetallic Pt nanoparticles containing 3d, 4d, and 5d transition metals (Fe, Ag, and Au, respectively). The first attempts to characterize the structure of Pt–$FeO_x$ nanoparticles revealed a predominantly Pt core coated with Fe oxide rather than the anticipated intermetallic PtFe surface.

While this Pt-core/$FeO_x$ shell structure is poorly suited to catalytic applications, subsequent experiments revealed that this oxide coating was removed during electrochemical cycling to expose a highly active Fe-modified Pt surface. However, the large amount of inaccessible Pt located in the cores of these nanoparticles renders them less than ideally suited for catalytic applications. In order to achieve better surface localization of Pt, AgPt nanoparticles were next prepared via galvanic reaction of a Pt precursor salt with Ag nanoparticles.

Those AgPt nanoparticles with the lowest Pt contents were found to have surfaces bearing few-atom Pt clusters, but Ag is unstable under FAO and ORR electrocatalytic conditions; a more electrochemically stable elemental composition was clearly required. Finally, a synthesis employing simultaneous reduction of Pt and Au precursors resulted in PtAu nanoparticles with few-atom Pt surface clusters that were both stable and highly active.

## List of Abbreviations and Symbols Used

| | |
|---|---|
| $a$ | diameter of illuminated sample area |
| $A$ | photon absorption |
| ANOVA | analysis of variance |
| a.u. | arbitrary units |
| $b$ | absorption cell path length |
| $c$ | concentration of analyte |
| $CN$ | coordination number |
| CV | cyclic voltammetry |
| $d$ | sample thickness |
| $D$ | lens diameter |
| DFT | density functional theory |
| DIW | de-ionized water |
| DMF | N,N-dimethylformamide |
| $E$ | photon energy |
| $E_0$ | absorption edge energy |
| $E_{1/2}$ | half-wave potential |
| $E_a$ | applied potential |
| $E_{ads}$ | adsorption energy |
| $E_{adsorbate}$ | energy of adsorbate molecule |
| $E_{calc}$ | calculated energy |
| $E_e$ | equilibrium potential |
| $E_F$ | Fermi energy |
| $E_k$ | electron kinetic energy |
| $E_{surface}$ | energy of bare metal surface |
| $E_{surface+adsorbate}$ | energy of surface and bound adsorbate |
| ECSA | electrochemically active surface area |
| EDS | energy dispersive X-ray spectroscopy |
| EG | ethylene glycol |
| EXAFS | extended X-ray absorption fine structure |
| $F$ | Faraday constant |

| | |
|---|---|
| $f(k)$ | backscattering amplitude function |
| $f_o$ | objective focal length |
| FAO | formic acid oxidation |
| FCC | face-centred cubic |
| FT-EXAFS | Fourier-transformed EXAFS |
| GGA | generalized gradient approximation |
| $h$ | Planck constant |
| $\hbar$ | reduced Planck constant |
| HCP | hexagonal close-packed |
| HRTEM | high-resolution TEM |
| $I$ | transmitted photon intensity |
| $I_0$ | incident photon intensity |
| ICP-OES | inductively coupled plasma optical emission spectrometry |
| $IR$ | voltage drop |
| $j$ | current density |
| $j_0$ | exchange current density |
| $j_{specific}$ | specific current density |
| $k$ | photoelectron wave vector |
| $m_e$ | electron mass |
| $n$ | refractive index |
| $N$ | number of particles measured |
| $NA$ | numerical aperture |
| $n_e$ | number of electrons transferred |
| OAm | oleylamine |
| ORR | oxygen reduction reaction |
| PAW | projector-augmented wave |
| PEMFC | polymer electrolyte membrane fuel cell |
| PVP | polyvinylpyrrolidone |
| $R$ | bond length |
| $R_G$ | ideal gas constant |
| RCF | relative centrifugal force |

| | |
|---|---|
| RDE | rotating disk electrode |
| ROI | region of interest |
| RPBE | revised Perdew-Burke-Erzerhof |
| RPM | revolutions per minute |
| $S_0^2$ | amplitude scaling factor |
| SPR | surface plasmon resonance |
| $T$ | temperature |
| UV-vis | ultraviolet-visible |
| $V_{cell}$ | fuel cell operating voltage |
| $V_{Ag/AgCl}$ | potential relative to Ag/AgCl reference electrode |
| $V_{RHE}$ | potential relative to reversible hydrogen reference electrode |
| XANES | X-ray absorption near edge structure |
| XAS | X-ray absorption spectroscopy |
| $\alpha$ | activity of chemical species |
| $\delta(k)$ | backscattering phase function |
| $\Delta E_0$ | edge energy shift |
| $\Delta E_e$ | anode-cathode equilibrium potential difference |
| $\Delta l$ | point-to-point resolution |
| $\Delta\mu_0$ | atomic absorption edge jump |
| $\varepsilon$ | molar attenuation coefficient |
| $\eta$ | overpotential |
| $\eta_a$ | anodic overpotential |
| $\eta_c$ | cathodic overpotential |
| $\lambda$ | photon wavelength |
| $\lambda(k)$ | photoelectron mean free path |
| $\lambda_e$ | electron wavelength |
| $\mu$ | mass absorption coefficient |
| $\mu(E)$ | total absorption signal |
| $\mu_0(E)$ | atomic absorption intensity |
| $\rho$ | volumetric mass density |
| $\sigma^2$ | Debye-Waller factor |

| | |
|---|---|
| $\chi^2$ | goodness-of-fit parameter |
| $\chi(E), \chi(k)$ | isolated EXAFS signal |
| $\chi^2_{red}$ | reduced goodness-of-fit parameter |

## Acknowledgements

First, I would like to thank my supervisor, Prof. Peng Zhang. Throughout our time together, Prof. Zhang has been an endless font of optimism and enthusiasm, providing the support necessary to overcome whatever challenges might lie ahead. I would also like to thank my supervisory committee (Prof. Mary Anne White, Prof. Mark Obrovac, and Prof. Heather Andreas) for their guidance and advice during the course of this project; their contributions have undoubtedly shaped it for the better.

I would additionally like to thank all Zhang group members, past and present. Special thanks go to Mark MacDonald, Stephen Christensen, Daniel Padmos, and Daniel Chevrier for all their help and companionship over the years. I sincerely hope that we continue to work together for many years to come.

Thanks go out to the Beamline Scientists who have contributed their time and expertise to this project: Yongfeng Hu, Tom Regier, and Ning Chen of the Canadian Light Source, as well as Robert Gordon and Zou Finfrock of the Advanced Photon Source. Further thanks are extended to Guangxu Chen, Xiaojing Zhao, and Prof. Nanfeng Zheng of Xiamen University; Chris Deming and Shaowai Chen from the University of California, Santa Cruz; and Victor Fung and De-en Jiang from the University of California, Riverside, for their great collaborative contributions. Thanks also to Tim Crowtz and Prof. Jeff Dahn of Dalhousie University for RDE equipment access and training.

Finally, I want to thank my family and friends for encouraging and supporting me on my journey down this long academic road. To my selfless parents, my brother and sisters, and everyone else who has put up with me all these years: Thank You.

# Chapter 1 – Introduction

## 1.1 Nanoparticles

In recent years, nanotechnology has grown to become a major focus for many researchers around the world. Through a better fundamental understanding of nanomaterials and their properties, other areas of research have also benefitted greatly. From photostable dyes to superior catalysts for the synthesis of organic molecules, nanomaterials have had an impact on numerous developing technologies.[1,2] Thus, fundamental research in this field has the potential to extend the influence of nanotechnology to practical applications.

### 1.1.1 A History of Nanoparticles

By definition, nanomaterials are objects which measure less than 100 nm in at least one dimension.[3] Some common nanomaterial structures are presented in Figure 1.1. While perhaps the best-known examples of nanomaterials are polyhedral nanoparticles, years of research have led to the development of increasingly complex structures. From relatively simple nanorods/nanowires[4] and nanosheets[5] to composite metal/semiconductor photocatalysts,[6,7] advances in the synthesis and structural characterization of nanomaterials have driven this research relentlessly forward. While the controlled design and production of these artificial nanoparticles is a more recent discovery, very early instances of their use can be found in certain historical objects.

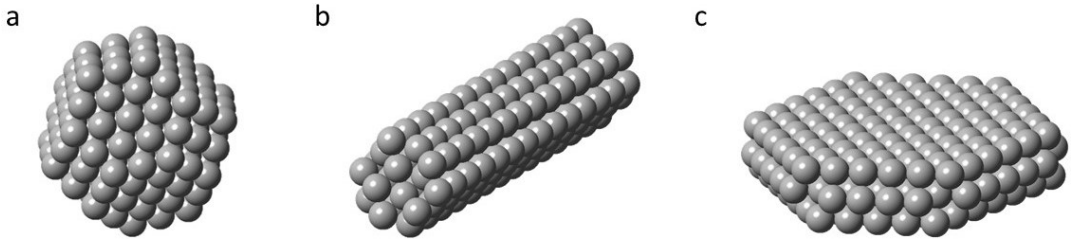


**Figure 1.1.** Examples of some common nanomaterial shapes, including (a) nanoparticle, (b) nanorod, and (c) nanosheet structures.

The earliest known examples of synthetic nanoparticles are found in art objects like the Lycurgus cup, a Roman artifact in which unique glass colouration (red in transmission, but green in reflection) is observed due to the presence of trace amounts of Au and Ag nanoparticles.[8] The nanoparticulate nature of these materials was likely lost on the cup's 4th century creators, however, as the first thoroughly scientific study of metal nanoparticles would not be revealed until Michael Faraday's seminal presentation at the Bakerian Lecture in 1857.[9] Faraday's studies exposed many key aspects of metallic nanoparticles that researchers still encounter today, including their synthesis via reduction from metal salts. The troublesome tendency of such suspensions to aggregate under certain conditions was also well documented, being well expressed by an excerpt from Faraday's lecture: "All endeavours to convert the violet [partially aggregated] gold back into ruby were either failures, or very imperfect in their results."[9] Despite the wealth of information presented in this paper, however, nanoparticles remained a mere curiosity for many years to come.

The field of nanoparticle research has since seen a dramatic rise in popularity, with the number of relevant publications increasing by at least 12 % annually since 1988 (as shown in Figure 1.2).[10] As a result of this rapid growth rate, over 80,000 relevant publications were produced in 2015, alone.[10] This boom in research activity has also dramatically expanded the breadth of the field; nanoparticles can now be produced using a variety of methods and tailored for applications in numerous fields, including cellular imaging, drug delivery, and catalysis.[6,11,12] At the heart of all these applications, though, lies the synthetic methods used to produce the nanoparticles.

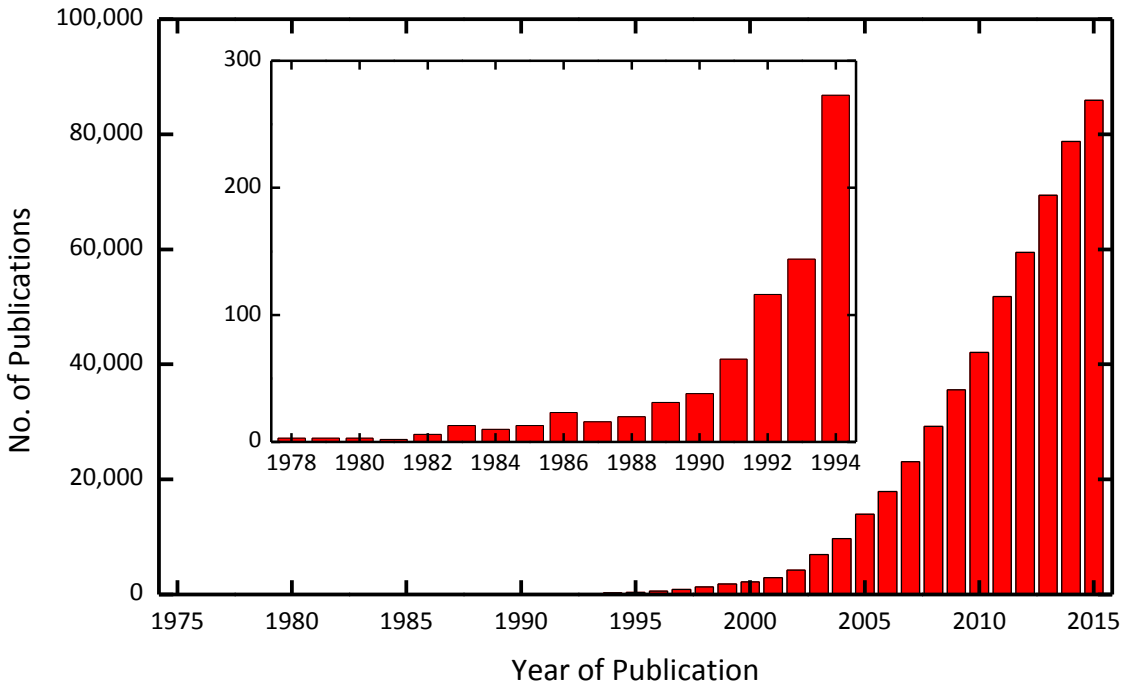


**Figure 1.2.** Plot of the number of publications containing the search term "nanopart*" as a topic since 1978 (via Web of Science database). The inset figure presents the same data, but is scaled to more clearly illustrate the fewer publications released between 1978 and 1994.

### 1.1.2 Modern Synthesis of Nanoparticles

The development of a more comprehensive understanding of nanoparticle synthesis is easily one of the most important aspects of the research field. Although the exact methods vary and have continue to evolve with time, nanoparticle syntheses can be divided into two categories: top-down and bottom-up. In a top-down synthesis, nanoparticles are generated by successively breaking down particles of a bulk material, typically via physical mechanisms such as ball milling,[13,14] laser ablation,[15] or sputter deposition.[16,17] Conversely, a bottom-up approach features a gradual assembling of nanoparticles from individual ions and molecules, as mediated by chemical reactions.[18] While both approaches have their respective advantages and disadvantages, the bottom-up approach is particularly appealing to those with backgrounds in chemistry due to its dependence on chemical reactions, which offer great potential for control and

modification of the nanoparticle product.

The specific reactions leading to bottom-up nanoparticle formation are largely dependent on the nature of the material; for example, metal nanoparticles are typically obtained via reduction of metal ions,[19] whereas oxides are frequently generated via induced precipitation or thermal decomposition.[20,21] In the case of metal nanoparticles, there are four primary components of a typical bottom-up synthesis: the metal precursor, the reducing agent, the reaction solvent, and the capping ligand.[19] Each of these components affects the size, shape, and stability of the resultant nanoparticles, allowing researchers to fine-tune their physical and chemical properties.

The major role of the reaction solvent is, naturally, to ensure the solubility of the other reaction components and product nanoparticles. Solvation depends primarily on the solvent used, but can be also modified to an extent by controlling the temperature at which the reaction is conducted.[19] The choice of reaction solvent also has important implications for the usefulness of these nanoparticles in certain applications. Nanoparticles intended for use in drug delivery or other *in vitro* applications, in particular, must be dispersible and stable under the aqueous conditions found in the human body.[19] Perhaps the most important factor in determining the suitability of nanoparticles for any application, though, is the choice of metal precursor.

The metal precursor in most bottom-up syntheses is a metal salt or complex that undergoes reduction by a reducing agent, leading to the assembly of nanoparticles. The choice of precursor is important due to both its degree of solubility in the reaction solvent and the nature of its counterions, the latter of which can have a significant effect on the structure of the product nanoparticles.[22,23] The fact that many transition metals are capable of adopting multiple stable oxidation states creates even more opportunities for

fine-tuning the reaction conditions. Finally, combining precursors of two or more different metals in a synthesis allows for the preparation of multi-metallic nanoparticles, which can result in drastic changes in nanoparticle properties relative to their monometallic forms.[24] It is, thus, clear that the metal precursor plays an important role in nanoparticle synthesis; however, its usability is contingent on the availability of an appropriate reducing agent.

Reducing agents may be organic (*e.g.*, citric or ascorbic acid) or inorganic (*e.g.*, sodium borohydride) in nature, and can exhibit a range of reduction potentials.[19] In either case, the "strength" (*i.e.*, reduction potential) of the reducing agent can impact nanoparticle size by determining whether nucleation or particle growth processes predominate during the synthetic reaction.[19] In general, whereas weaker reducing agents tend to generate larger nanoparticles by promoting particle growth over nucleation, stronger reducing agents have the opposite effect and tend to produce smaller nanoparticles.[19] Another important consideration when selecting a reducing agent is how easily it can be removed during subsequent sample purification. Solid materials tend to be more challenging to remove without also losing some of the product nanoparticles; thus, employing more easily separated liquid or gaseous reducing agents can greatly simplify the purification process.[25,26] Perhaps the most significant reaction component of a nanoparticle synthesis, though, is the capping ligand.

The primary function of capping ligands is to mediate the growth and stability of nanoparticles, both during and after their synthesis.[19] These ligands are typically organic molecules or polymers bearing functional groups capable of interacting with nanoparticle surfaces.[19] Ligand-surface interactions vary in strength and may be covalent, electrostatic, or physical in nature.[19] In order to impart good stability, these ligands must interact

strongly with both the nanoparticle surface and reaction solvent, and also be either sufficiently bulky (Figure 1.3a) or charged (Figure 1.3b) to prevent the metal surfaces from coming into contact with one-another.[19] In addition to the wide range of capping ligand molecules that exist, combinations of different ligands can be employed to further fine-tune the reaction conditions.[25]

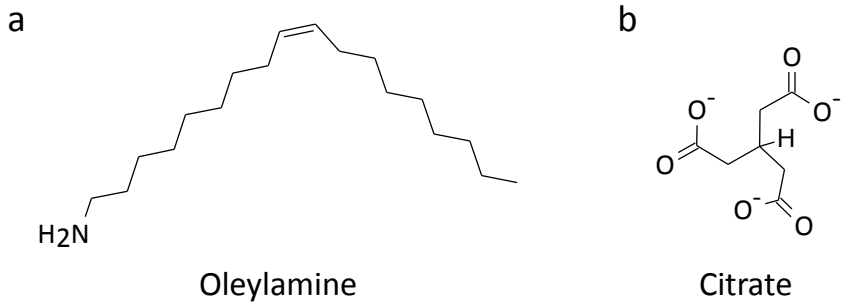


**Figure 1.3.** Structures of some representative capping ligands used to stabilize nanoparticles via (a) steric and (b) electrostatic repulsion forces.

In addition to their role in maintaining stability, ligands also influence nanoparticle structure and properties in a number of ways. Both higher ligand concentrations and stronger surface-binding interactions result in in the formation of smaller particle sizes, while lower concentrations and weaker binding interactions tend to favour larger particles.[19] With regard to surface structure, even small molecules such as carbon monoxide can strongly bias the formation of surfaces with specific indices via preferential binding at certain sites.[19,27] Finally, ligands can also be used to impart further functionality to metal nanoparticles by conjugating biologically active molecules to their surfaces either directly or via a connecting ligand. These molecule-bound nanoparticles may then be used in order to provide better control over the localization of a drug within the body.[12]

With the primary parameters involved in bottom-up metal nanoparticle synthesis

having been discussed, the significant complexity involved in these reactions is now clear. Although not all parameter combinations will result in successful syntheses, a wide range of possible reaction conditions does exist. Manipulation of these synthetic parameters can be used for anything from fine-tuning specific nanoparticle properties to producing samples with novel compositions and structures. In either case, it is important to understand the essential properties of nanoparticles that make research in this field so interesting.

### 1.1.3 Properties of Nanoparticles

Although they have been a subject of scientific research for decades,[28] nanoparticles have only in recent years begun to see use in commercial products. Ferromagnetic iron oxide nanoparticles, for example, are now used as magnetic resonance imaging contrast agents, thermotherapy agents, and more,[29] while the antimicrobial action of Ag nanoparticles has led to their incorporation into clothing and textiles.[30] Other applications of nanoparticles, such as fuel cell catalysis, are beginning to emerge,[31,32] but are still under development.[33] Regardless of the specific application, however, much of nanoparticles' appeal can be attributed to their small size.

Emergent properties are exhibited by some nanoparticles as a result of electronic quantum confinement effects.[34,35] Metal nanoparticles, for example, tend to experience collective excitations of their surface electrons in a phenomenon known as surface plasmon resonance (SPR).[6] For some metal nanoparticles, such as those made from Ag and Au, the required excitation energy falls in the visible region of the electromagnetic spectrum, allowing them to be employed as labelling agents in various chemical and biological systems.[6] Even more dramatic changes in behaviour are observed in

nanoparticles below *ca.* 2 nm in diameter; once this lower size threshold is reached, the continuous metallic band structure breaks down into more discrete energy levels, resulting in the emergence of molecule-like properties such as optical fluorescence.[36] This phenomenon is commonly observed in small Au nanoparticles (less that *ca.* 2 nm), which are often referred to as nanoclusters to emphasize their smaller size and resemblance to polynuclear clusters more commonly seen in inorganic chemistry research.[36] Although not all metal nanoparticles exhibit useful optical properties, many have other potential applications, such as the catalytic activity demonstrated by Pt.

### 1.1.4 Nanoparticle Fuel Cell Catalysts

Pt nanoparticles can be employed to perform a wide range of chemical reactions, including the catalysis of electrode reactions in fuel cells.[37] Fuel cells are electrochemical devices used to generate energy from simple chemical feedstocks. Although they are not yet widely utilized, some types of fuel cells are beginning to break into the commercial market.[31,32] Polymer electrolyte membrane fuel cells (PEMFCs) are particularly well-suited to automotive applications due to their high energy density,[38] as is exemplified by modern vehicles like the Toyota Mirai.[39] Unfortunately, the performance of these PEMFCs is ultimately limited by the rate of the oxygen reduction reaction (ORR) at the cathode.[38] Because this reaction is enhanced by using Pt metal as a catalayst,[38] perhaps the most obvious approach would be to increase catalyst loading at the electrode; however, such catalyst materials are expensive and the availability of Pt would be insufficient to satisfy the growing worldwide demand for automobiles.[40] In addition, simply increasing catalyst loading has been demonstrated to yield diminishing returns in terms of catalytic performance.[41] As a result, finding alternative means of improving

these electrode catalysts is crucially important.

Given the wide range of reactions that can be catalyzed by Pt nanoparticles, it is no surprise that extensive efforts have been made to understand the source of their activity in terms of their structure and electronic properties.[42–44] Due to their exceptionally small size (and the correspondingly low proportion of inaccessible atoms within the particle core) nanoparticles have a very high “atom economy".[45] As is shown in Figure 1.4a, as nanoparticle diameter decreases, the number of total atoms decreases as the proportion of atoms located at surface sites increases. Also shown (Figure 1.4b) is an image illustrating the core (blue) and surface (red) sites in a nanoparticle of *ca.* 1 nm in diameter. By thus maximizing the number of catalytically active atoms located at accessible surface sites, less material is required and costs can be significantly reduced. Unfortunately, the improvements afforded by this size advantage are insufficient to overcome the issues of cost and availability; additional measures need to be taken to improve these Pt-based catalysts.

Another promising approach to improving catalyst performance is to carefully control the facets formed at the surface of nanoparticles. Experiments have shown that different metal surfaces, defined using Miller indices, exhibit differing levels of catalytic activity.[23,27,46,47] Thus, by preferentially forming more-active facets (*e.g.*, via the use of small-molecule protecting agents[27]) shape-controlled nanoparticles can exhibit enhanced catalytic activity. These activity enhancements are limited, however, by the need for well-ordered surfaces. This dependence results in a minimum size for nanoparticles that may be synthesized in this way, thereby also limiting the atom economy of the catalyst. Fortunately, a more promising approach to improving nanoparticle performance is via the combination of multiple metals.

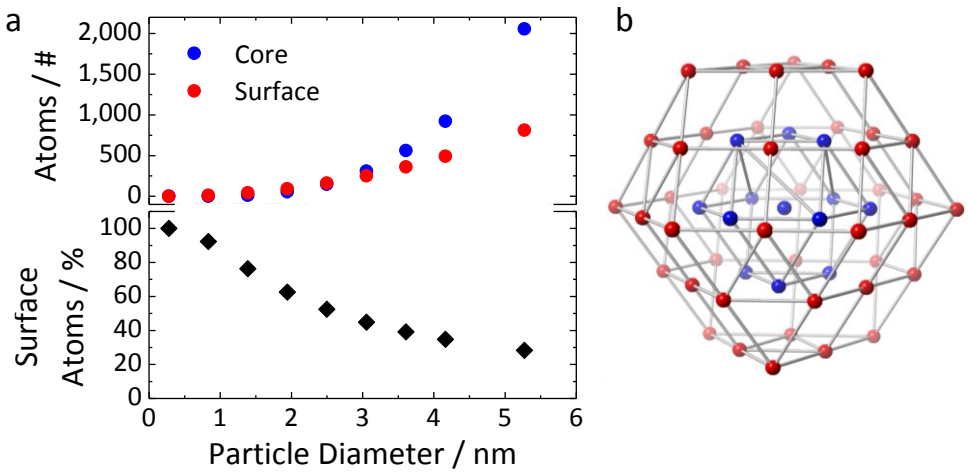


**Figure 1.4.** (a) Plots describing core and surface atom counts and proportional distributions in nanoparticles less than 6 nm in diameter, and (b) a model nanoparticle of *ca.* 1 nm in diameter with core and surface atom sites indicated in blue and red, respectively.

In the case of Pt, the controlled formation of bimetallic nanoparticles using transition metals such as Fe and Ni can result in both increased activity and, thus, reduced material cost.[47–49] This increase in activity means that less catalyst material is required to obtain the desired catalytic performance. Consequently, nanoparticles made from even expensive materials can be reasonably used to accomplish real-world tasks. For some applications, such as catalyzing reactions involving small carbon-based molecules, the susceptibility of Pt surfaces to carbon monoxide "poisoning" (*i.e.,* irreversible binding) makes it a particularly poor catalyst.[50] In these cases, the contaminant carbon monoxide is generated by reaction such as the partial oxidation of methanol or decomposition of formic acid.[51,52] Through the formation of Pt-based bimetallic nanoparticles, however, it is also possible to obtain catalysts which are highly resistant to surface poisoning.[53]

Incorporating other metals into Pt nanoparticles also imparts customizability via the distribution of the component metals within the nanoparticle. Depending on the tendency of the component metals to segregate or mix, multi-metallic nanoparticles may take on a variety of structures. Heterostructured, core-shell, surface island, random alloy,

and intermetallic nanoparticles (illustrated in Figure 1.5) can all be prepared using a variety of synthetic methods.[54,55] Differentiation between these structures is important, as their atomic distributions can produce a variety of different surface structures and, thus, have a strong effect on their respective catalytic activities.[54,55] Among these possible structures, few-atom (or even single-atom) Pt surface islands offer optimal distribution of Pt, with few or no Pt atoms being located in the particle core. However, achieving such as structure will require carefully selected synthetic methods as well as the availability of techniques capable of accurately measuring the nanoparticle structure.

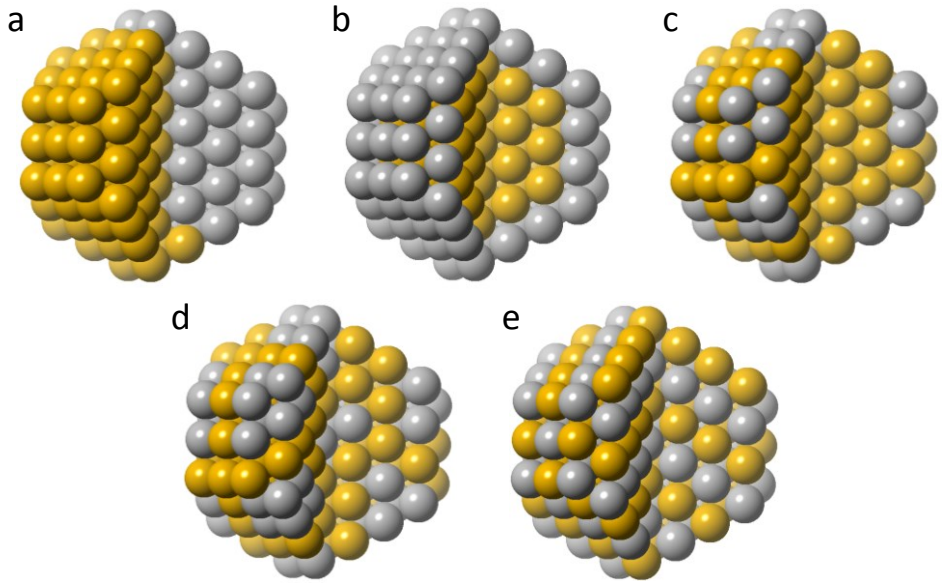


**Figure 1.5.** Nanoparticle models with (a) heterostructured, (b) core-shell, (c) surface island, (d) random, and (e) intermetallic alloy morphologies.

## 1.2 Motivation and Thesis Objectives

Finding new means of meeting the growing global demand for energy is a major driving factor in scientific research, a trend which will persist into the foreseeable future. However, it is no longer sufficient to just provide this energy; as much as possible, energy must be generated renewably and with minimal emission of pollutants and greenhouse

gases. Due to their minimal chemical emissions and ability to store energy generated via environmentally friendly means, the potential utility of electrochemical fuel cells as energy storage systems makes them an important avenue of research. Fundamental research into materials contributing to their development is, thus, similarly valuable.

In addressing this issue, three key concepts are emphasized: the suitability of X-ray absorption spectroscopy (XAS) techniques for the characterization of surface structure in Pt-based alloy nanoparticles, the use of complementary characterization techniques to help confirm the surface structures inferred using XAS, and the correlation of this structural information with the catalytic behavior of the nanoparticles studied. In this way, a greater understanding of the catalytic reactions occurring at the surface of these Pt-based materials will be obtained. Due to its importance in nanoparticle production, a minor emphasis is also placed on the use of simple synthetic methods requiring little subsequent work-up or purification.

## 1.3 Thesis Structure

Following the general introduction to nanomaterials provided in Chapter 1, background information regarding instrumental techniques employed throughout this thesis are presented in Chapter 2. Due to the variety of samples and measurements conditions studied in the course of the research, specific information regarding each technique will be provided in each subsequent chapter.

Chapter 3 describes a first foray into the synthesis and characterization of Pt-based nanoparticles. The fluorescent properties of these Pt nanoclusters were investigated using ultraviolet-visible (UV-vis) spectroscopy and explained using structural information obtained through the implementation of XAS techniques. It was revealed that the

structure of these nanoclusters can be well characterized using XAS, but that they did not have the metallic structure desired for electrocatalytic applications.

Chapter 4 presents a study of the structure and ORR electrocatalytic activity of carbon-supported nanoparticles prepared including both Pt and Fe in the reaction mixture. In addition to electrochemical and XAS analyses, these nanoparticles were studied using transmission electron microscopy (TEM) and energy dispersive X-ray spectroscopy techniques. *Ab initio* calculations were also used in order to support the experimental results. In this case, metallic nanoparticles were successfully obtained and shown to have good electrocatalytic ORR activity. The localization of Pt at the nanoparticle core was, however, not ideal, and concerns were raised regarding the stability of surface Fe species under electrocatalytic conditions.

In Chapter 5, the Pt–$FeO_x$ nanoparticles presented in Chapter 4 are further studied in order to investigate the effects of strong acids and cycled potentials on their surface structure. Again, TEM, cyclic voltammetry (CV), and XAS techniques were employed in this investigation. More extensive characterization of the electrocatalytic activity of these nanoparticles was also presented. It was found that significant surface modification occurred during electrochemical treatment, leading to the conclusion that performing *in situ* or post-catalysis characterization is critical to understanding the true active structure of nanoparticle catalysts.

Chapter 6 explores the use of a two-step synthetic procedure to prepare core-shell AgPt nanoparticles. UV-vis spectroscopy, TEM, and XAS techniques were used to closely study the surface structure of these nanoparticles, with *ab initio* calculations again being used to support the experimental results. While all AgPt nanoparticles shared the same general Ag-core/Pt-shell structure, those with the lowest Pt content also exhibited

very small Pt clusters at their surfaces, however these nanoparticles were not characterized electrochemically.

Chapter 7 describes a thorough characterization of PtAu nanoparticles prepared using a one-step synthesis. TEM, CV, XAS, and X-ray photoelectron spectroscopy (XPS) results were employed to obtain structural information. Once again, surface clusters of Pt atoms were observed in the low Pt-content Au-core/Pt-shell nanoparticle samples. The formic acid oxidation reaction at the surface of these nanoparticles was also explored, with support from *ab initio* calculations performed using density functional theory. It was found that excellent formic acid oxidation activity was exhibited by these samples, due to the apparent ability of few-atom Pt clusters to avoid self-poisoning by CO.

Finally, Chapter 8 summarizes the conclusions from previous chapters and explains their relevance to the outlined research goals. Future avenues of research for this project are also discussed, pertaining to both nanoparticle catalysis and XAS characterization of nanomaterials. While much progress has been made, there is also still room to explore.

# Chapter 2 – Experimental Methods

A range of experimental techniques has been employed in the characterization of the Pt-based nanoparticles discussed in this thesis. In order to provide some basic familiarity with these experimental techniques, relevant background information is provided herein. Greater descriptive depth is provided for techniques that play more significant roles in this research, particularly those with which readers are likely to be less familiar. Due to the use of different conditions and equipment for many experiments, the specifics of experimental parameters and equipment are provided in each chapter, individually.

## 2.1 X-ray Absorption Spectroscopy

### 2.1.1 The Need for XAS Techniques

The rarity of high yield nanoparticle syntheses makes it challenging to produce the relatively large quantities of material required for many conventional techniques.[58] Furthermore, the few-nanometer size of these nanoparticles limits the usefulness of techniques such as powder X-ray diffraction, which rely upon the existence of long-range order within the sample.[59] Conversely, techniques such as $^{195}$Pt nuclear magnetic resonance spectroscopy require a sample to contain fewer atoms of the target element (on the order of tens of atoms) than are typically present in nanoparticles (typically hundreds to thousands of atoms, or more).[60] For all but the smallest nanoparticles, peak broadening caused by the relatively large number of atoms severely limits the amount of structural information that can be obtained using $^{195}$Pt NMR.[61] Fortunately, techniques capable of reliably characterizing nanoparticle catalysts are available. XAS is sensitive enough to be

performed on just milligrams of material and powerful enough that detailed electronic and structural data can be obtained from a wide range of materials, including even liquid and amorphous samples.[62] For these reasons, XAS has been widely adopted by nanoparticle researchers as an invaluable tool for studying the structure and properties of nanoparticles.[63]

### 2.1.2 Background and History

Since their discovery, X-rays have been employed in a variety of applications, including medical and material science studies.[64–66] In the early days, X-rays used in XAS measurements were generated in research laboratories using X-ray tubes and detected through the use of photographic plates in conjunction with a single-crystal monochromator.[67] As the quality of data obtained using XAS improved, oscillatory variations in the measured absorption amplitudes were eventually observed. Initially referred to as "Kronig structure" after the German researcher Ralph Kronig who developed the first theory for their analysis, these features eventually came to be known as extended X-ray absorption fine structure (EXAFS).[67] Despite these advantages, the relatively low intensity of laboratory-based X-ray sources limited the widespread use of the XAS technique; it was not until the arrival of dedicated synchrotron facilities that this technique was revolutionized and became able to capture the attention of the broader scientific community.[67]

Since the advent of synchrotron X-ray sources, the time required to obtain good-quality data from a sample has decreased from hours or days to mere minutes, or even seconds.[68] The X-ray beams generated at synchrotrons by the acceleration of high-velocity electrons are very intense and well-monochromated, making possible this

extraordinary forward leap in performance.[67] The critical role played by synchrotron technology in advancing the use of XAS is neatly encapsulated by the words of Dr. Farrel Lytle, an instrumental contributor to the field of XAS throughout the course of his career: "In one trip to the synchrotron we collected more and better data in three days than in the previous ten years. I shut down all three X-ray spectrometers in the Boeing laboratory. A new era had arrived!".[67]

XAS offers a number of advantages when it comes to sample analysis. This technique is both non-destructive and sensitive, requiring just a few milligrams of the target element for data acquisition. More importantly, though, XAS allows for element-specific characterization of materials, due to the characteristic absorption edge energies of each element.[69] This can be especially useful for samples containing two or more elements of interest, as it affords multiple perspectives into the overall structure and electronic properties of the material.

In addition to the aforementioned general advantages, XAS is particularly useful in the study of metal nanoparticles. Although XAS spectra represent an average over all atoms in sample, the small size of nanoparticles means that a relatively large proportion of their constituent atoms are present at the particle surface. This enables the surface atoms of the nanoparticles to be studied without such a large background from atoms located in the bulk of the particle.[63] In the case of bimetallic nanoparticles, coordination number (*CN*) values determined from fitting of the EXAFS data can be used to qualitatively determine the distribution of elements within the particle: lower *CN*s correspond to surface-located atoms, whereas higher *CN*s indicate preferential localization in the particle cores.[63] These advantages render XAS techniques ideally suited for the characterization of catalytically active nanoparticles. Explaining how XAS

is able to provide these advantages, however, requires a deeper understanding of the underlying physical phenomena.

### 2.1.3 XAS Mechanisms and Theory

When an atom absorbs a sufficiently energetic X-ray photon, a core-level electron is excited to a valence or continuum energy level,[69] as illustrated in Figure 2.1. In a typical experiment, an XAS spectrum is acquired by measuring the absorption of a transmitted X-ray beam through the sample (*e.g.*, a metal foil or compacted pellet of powder). The extent of absorption is measured from the intensity of the transmitted X-ray beam, $I$, relative to its initial intensity, $I_0$, as shown in the following equation:

$$I = I_0 e^{-\mu \rho d}, \tag{2.1}$$

wherein $\mu$ is the mass absorption coefficient of the target element, $\rho$ is the density of the sample material, and $d$ is the thickness of the sample material.[70] It is important to note, however, that while all spectra obtained using XAS are element-specific (*i.e.*, only atoms of the target element are counted), they do represent an average over all atoms of that target element within a sample.

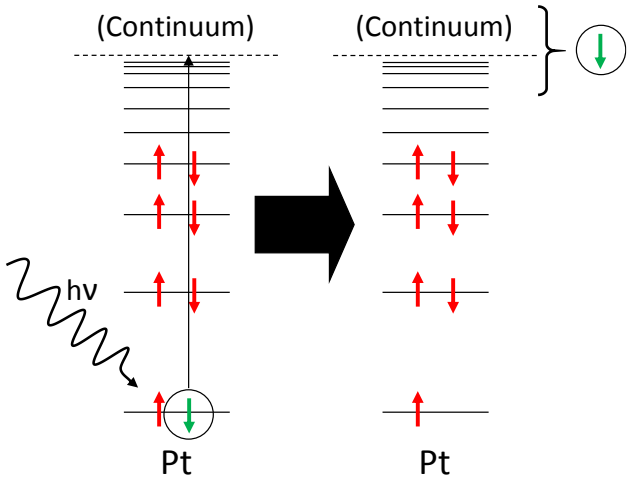


**Figure 2.1.** A simplified energy level diagram illustrating the origin of XAS spectra from the excitation of a core-level electron (circled) to valence or continuum states (*i.e.*, via photoelectron emission).

As is shown in Figure 2.2, a typical XAS spectrum can be divided into two main sections: the XANES (X-ray absorption near edge structure) region and the EXAFS region. For X-rays with energies within *ca.* 30 eV of the absorption edge energy of the target atom, excited core-level electrons are promoted to fill vacancies in the valence orbitals; these electronic transitions give rise to the major features in the XANES spectrum of an element.[69] X-rays with greater energies are sufficient to ionize atoms of the target element, resulting in photoejection of core-level electrons.[69]

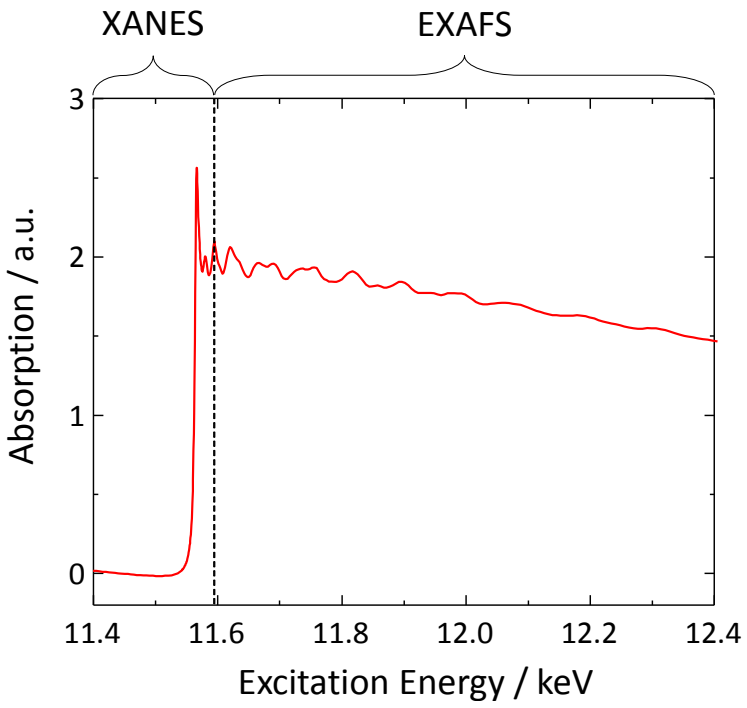


**Figure 2.2.** A representative spectrum obtained by performing XAS measurements at the Pt $L_3$ absorption edge, illustrating the general XANES and EXAFS regions.

The mechanism giving rise to the observed EXAFS oscillations is rather complex, but years of investigation have led to it becoming well understood.[67,69] Due to the fact that XAS is inherently dependent on electronic excitations, the magnitude of absorption in the EXAFS spectrum is controlled by both the initial and final states of the excited atom.[69] When an absorption event occurs, photoelectrons are emitted from the excited atom in all

directions (see Figure 2.3a).[69] As they travel away from the absorbing atom, photoelectrons interact with neighbouring atoms in the sample and are scattered. A portion of these scattered photoelectrons return to the excited atom (see Figure 2.3b), where they alter the probability of subsequent electronic excitations.[71] The range of this backscattering effect is, however, limited.

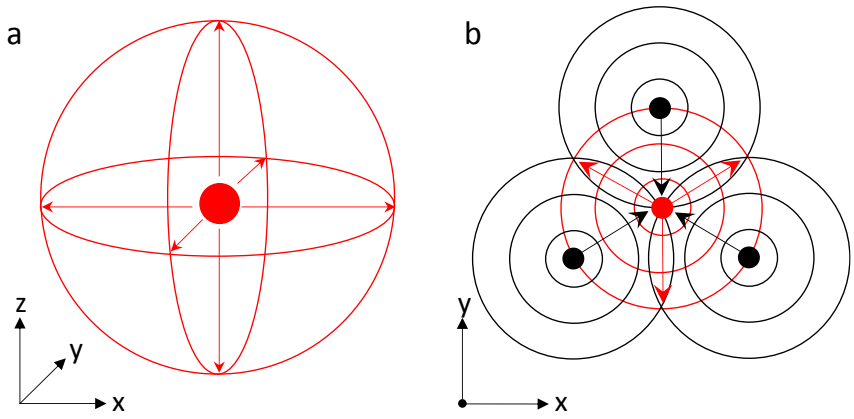


**Figure 2.3.** Simplified diagrams illustrating (a) the omnidirectional emission of photoelectrons from the absorbing atom (red) and (b) backscattering of photoelectrons from neighbouring atoms (black) following X-ray absorption. The red and black arrows illustrate the direction of propagation for photoelectron waves.

The distance traveled by photoelectrons in the given material is not infinite, but rather limited by their inelastic mean free path.[69] The inelastic mean free path of an electron depends not only on the nature of the material is passes through, but also on the electron's kinetic energy.[72] Photoelectrons generated in XAS have kinetic energies, $E_k$, equal to the difference between the incident X-ray energy, $E$, and the absorption edge energy, $E_0$, of the target atom, as per:

$$E_k = E - E_0.^{64} \tag{2.2}$$

Based on the typical inelastic mean free paths of electrons generated in XAS, the maximum range of EXAFS characterization is limited to tens of nanometers.[69] This range is more than sufficient for applications of XAS in nanoparticle research, however, and the spectra so obtained can yield large amounts of information.

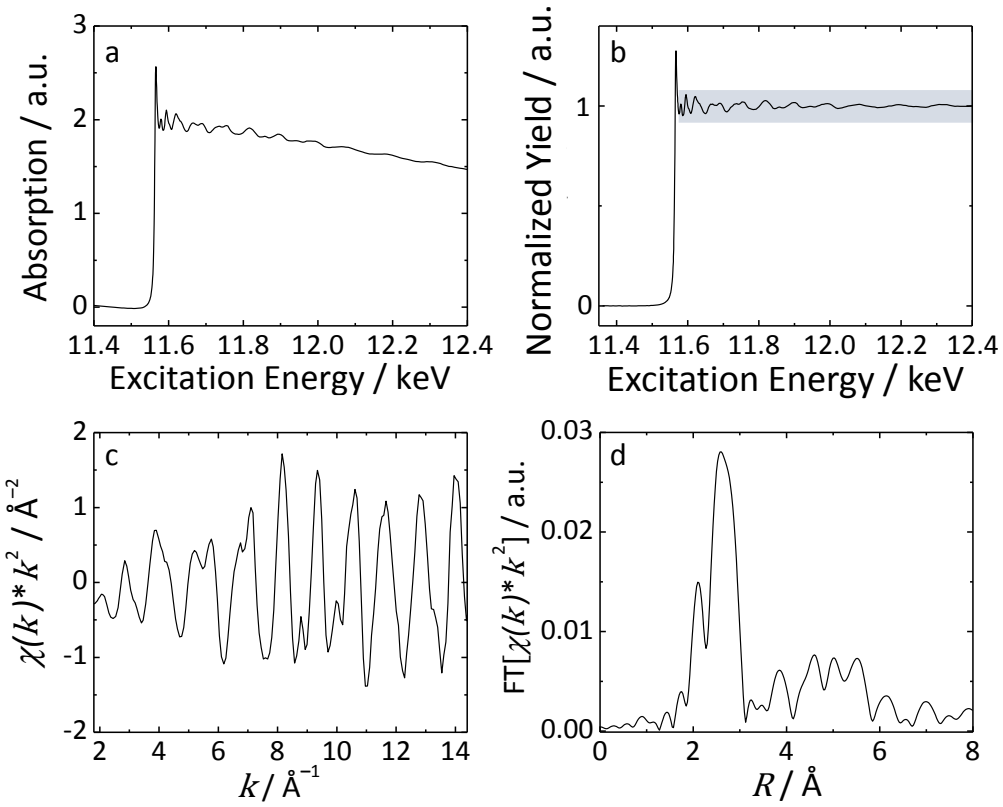


**Figure 2.4.** The stages of EXAFS data work-up, including (a) raw and (b) background-subtracted/ normalized XAS spectra, (c) the isolated EXAFS signal, and (d) the Fourier-transformed EXAFS (FT-EXAFS) spectrum. The shaded (grey) region in (b) highlights the region of the XAS spectrum from which the EXAFS data in (c) are isolated.

The work-up required for XANES spectra can be accomplished in very few steps. The raw XAS spectrum (see Figure 2.4a) is first background-subtracted by fitting simple polynomial functions to the pre- and post-edge regions, and then normalized to the edge jump (see Figure 2.4b). In contrast, EXAFS spectra must be isolated from the raw absorption spectrum using the full, multi-step process shown in Figure 2.4. After background-subtracting and normalizing the raw spectrum, a spline is fitted to the EXAFS data and the following is equation used to obtain the isolated EXAFS signal, $\chi(E)$, as shown in Figure 2.4c:

$$\chi(E) = \frac{\mu(E) - \mu_0(E)}{\Delta\mu_0}, \tag{2.3}$$

wherein the total XAS signal in the post-edge region, $\mu(E)$, is background-subtracted by the smooth atomic X-ray absorption signal, $\mu_0(E)$, and normalized relative to the atomic absorption edge jump, $\Delta\mu_0$.[69] Finally, the EXAFS spectrum is Fourier-transformed, resulting in a radial distribution function describing the relative locations of neighbouring atoms in the atomic lattice (see Figure 2.4d). After having been so processed, these sample spectra are ready for detailed analysis.

### 2.1.4 Analysis of XANES Spectra

In XANES spectra, the first peak immediately following the absorption edge sample is often referred to as the "white line." This stems from the historical use of photographic plates as primitive area detectors for transmitted X-rays. The greater absorption of X-rays by the sample at this point in the spectrum results in less exposure of the plates and a visibly whiter colouration, as is illustrated by the diagrammatic plate in Figure 2.5.[67,73] As mentioned previously, the white line corresponds to allowed excitations of core level electrons to vacancies in the valence orbitals of the given atom.[74] As a result, its position and intensity can be used to infer information regarding the electronic environment of the target element.

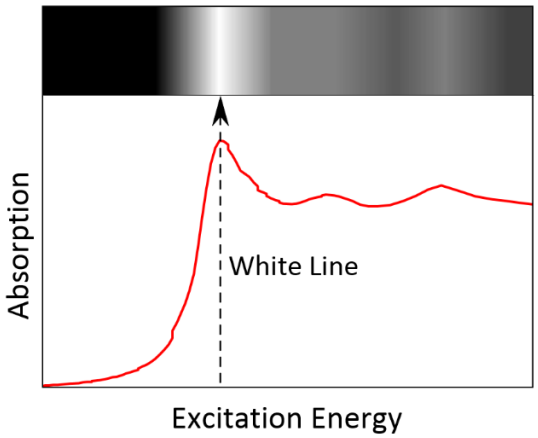


**Figure 2.5.** Illustration showing the white line position of a XANES spectrum as would be recorded using (top) diagrammatic photographic plate exposure and (bottom) modern absorption detection methods.

At the simplest level, the distinct features in the XANES region can be used as a spectral "fingerprint" that is representative of a given material. For more in-depth characterization, linear combination fitting can also be used to deconvolve spectra arising from mixtures of distinct chemical phases by using spectra from known reference materials.[75] Significant features may also be present just prior to the spectral absorption edge; these so-called pre-edge features can provide additional structural information about the sample.[74] For example, the pre-edge feature in the Fe K-edge absorption spectrum represents an s-to-d bound-state transition. While this electronic transition is normally spin-forbidden, it can become allowed if p-d orbital mixing occurs as a result of the Fe atom's coordination environment.[74] The intensity of resulting feature is, thus, representative of the local structure at Fe sites in the material. While the information afforded by such analysis can be substantial, additional methods of data analysis continued to be developed as X-ray technology evolved. In addition to the wealth of information that can be obtained from analysis of the XANES region, EXAFS analysis can be used to infer significant information regarding the local structural environment of the element of interest.

### 2.1.5 Analysis of EXAFS Spectra

In comparison with most XANES analysis procedures, EXAFS analysis of samples can be considerably more complex. Due to the fact that core-level absorption edges span a very large range of energies, it is helpful to describe EXAFS spectra in terms of wave vector, $k$, instead of excitation energy, as follows:

$$k = \frac{\sqrt{2m_e(E - E_0)}}{\hbar} \tag{2.4}$$

wherein $m_e$ is the mass of an electron, $E$ is the photon energy, $E_0$ is the absorption edge

energy for the target element, and $\hbar$ is the reduced form of Planck's constant.[69] The amplitudes of EXAFS spectra are often scaled by some multiple of this wave vector in order to offset the gradual decay of signal intensity at higher energies. While this form of spectrum provides some room for qualitative interpretation, fitting the data at this point requires extensive knowledge of the sample phase, as all scattering paths are convolved into a single waveform. Fourier-transformation of this EXAFS data allows contributions from neighbouring atoms to be displayed as a function of distance from the excited atom. By exclusively selecting the region of the spectrum corresponding to the desired interactions, the data can be fitted without worrying about contributions from the numerous other scattering paths.[69]

Fitting of the FT-EXAFS spectra is usually performed using commercial or freely available software packages such as FEFF8 in conjunction with WinXAS or Demeter (formerly IFEFFIT).[76–78] FEFF8 software is designed to perform various computations related to XAS using a Green's function approximation; determination of scattering amplitude and phase shift functions used for FT-EXAFS fitting, as well as simulation of XANES spectra, and even charge transfer between atoms can be calculated using this method.[78] Both WinXAS and Demeter software are designed for XAS data work-up and fitting, while also providing some miscellaneous tools to aid in data analysis. In brief, prior to fitting an FT-EXAFS spectrum, a Cartesian structural model representative of the sample being studied is first generated from crystallographic coordinates using modelling software (*e.g.*, Crystalmaker[79]). Next, amplitude and phase-shift functions are calculated using FEFF8, with the Cartesian coordinates as input. Having obtained these amplitude and phase-shift functions for each scattering path in the structural model, it is now possible to fit the FT-EXAFS spectrum.

Once processed, the FT-EXAFS spectrum can then be fitted using WinXAS or Demeter, allowing the values of certain structural parameters to be extracted. Experimental spectra are fitted using the following function:

$$\chi(k) = \sum \frac{CN \cdot S_0^2 f(k)}{kR^2} \cdot e^{-2k^2\sigma^2} \cdot e^{\frac{-2R}{\lambda(k)}} \cdot \sin\big(2kR + 2\delta(k)\big), \qquad (2.5)$$

such that $\chi(k)$is the amplitude of the function at wave vector $k$, $CN$ is the coordination number of the scattering atom located at distance $R$, $S_0^2$ is the amplitude scaling factor, $f(k)$ and $\delta(k)$ are the backscattering amplitude and phase shift functions, $\sigma^2$ is the Debye-Waller factor, and $\lambda(k)$ is the photoelectron mean free path.[69] Among these parameters $S_0^2$, *CN*, $R$, and $\sigma^2$ are usually allowed to vary during fitting, with the addition of an edge energy shift ($\Delta E_0$) parameter used to account for differences between the experimental absorption edge energy from the XANES spectrum and the calculated value for the scattering paths determined using FEFF8.[80] While the method used to obtain these structural parameters is universal, estimation of their associated uncertainties is less well established.

### 2.1.6 Quantification of Uncertainty in EXAFS Fitting

The quantification of uncertainty in structural parameters determined from EXAFS fitting is an issue that has long plagued users of the technique.[81–83] A handful of quantification methods, with varying degrees of rigorousness, has been reported in the literature, including static estimates (typically ± 20 to 25 % for *CN*s and ± 0.02 Å for bond lengths)[84,85] and variation of a single parameter while monitoring resulting change in the goodness-of-fit parameter, $\chi^2$.[86,87] A large number of publications, however, ignore the issue entirely. It appears that the most rigorous error determination method in use by researchers is that implemented by Demeter XAS analysis software.[77] The strength of this

method stems from the fact that it incorporates several key factors, including correlation between fitted parameters, the number of degrees of freedom available during fitting, and the magnitude of noise in the experimental FT-EXAFS spectrum.[83]

Demeter and its predecessor, IFEFFIT, are freely available from the developers, and so these software packages are almost ubiquitously used in the analysis of XAS data. However, the additional control afforded by commercial software such as WinXAS makes it preferable for some tasks. Unlike Demeter, WinXAS does not take into consideration the $\chi^2$, and defaults to the use of a too-low "error parameter". This less-robust approach results in unrealistically small uncertainties for both low- and high-noise sample spectra (as presented in Figure 2.6). In order to address this issue, a method of reproducing the uncertainty determination methods of Demeter was developed and implemented.[88] The calculations required for this method are tedious to perform manually, and so the simple computer program "Analyzer v0.1" was written in order to streamline the process. This program was used for uncertainty determination in Chapters 3 and 7. Chapters 4, 5, and 6 employed the IFEFFIT package as it offers the ability to simultaneously fit spectra with shared variables, an option that is not available using WinXAS/Analyzer v0.1.

Using this procedure, the average peak amplitude was first computed over the range of 15 to 25 Å in the FT-EXAFS spectrum; because this spectral region contains almost exclusively noise from the experimental data, it can be used to approximate the uncertainty contained therein.[83] This value is then used as the WinXAS error parameter during the fitting process, resulting in slightly more accurate uncertainties for the parameter values. The corresponding $\chi^2$ value for the fit is divided by the number of degrees of freedom for the fit, yielding the reduced chi-squared value, $\chi^2_{red}$. Finally, the

improved uncertainty values from WinXAS are multiplied by $\chi^2_{red}$ to give the correct uncertainties for each parameter value, as shown in Table 2.1. While this more-robust method of uncertainty determination lends further credibility to the use of XAS techniques in the characterization of nanoparticles, it is important to also consider the importance of studying samples using complementary methods of analysis.

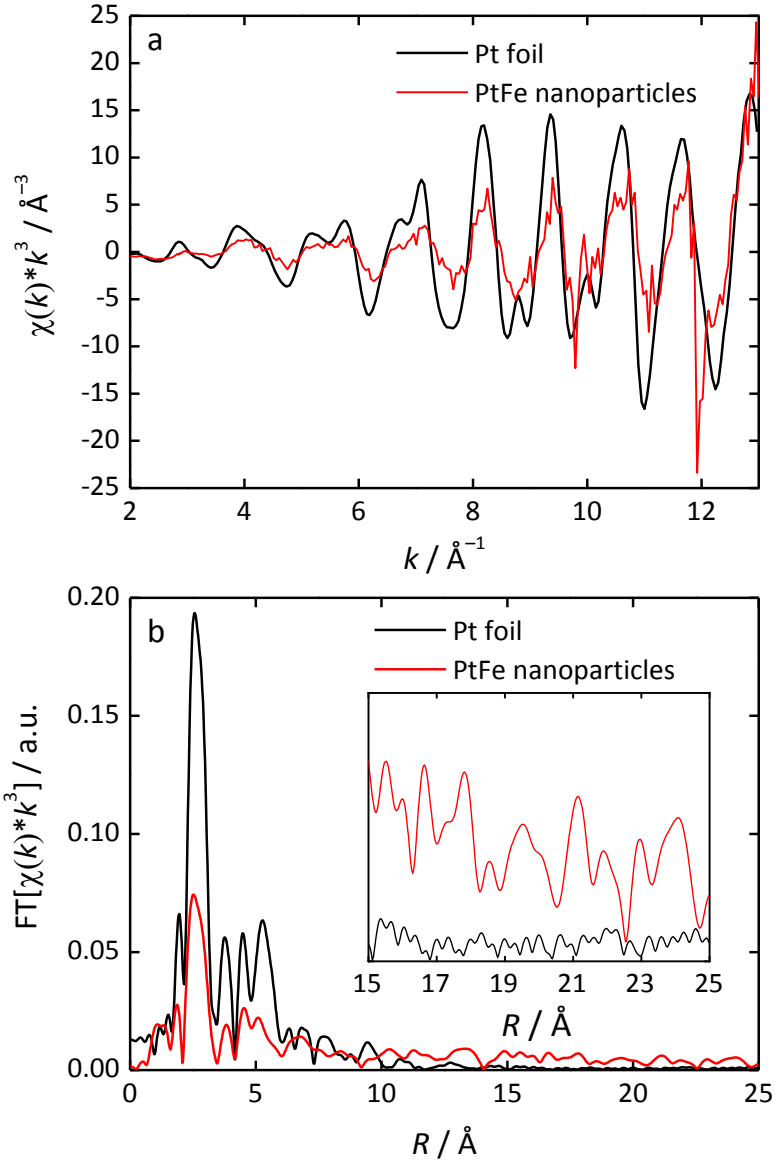


**Figure 2.6.** Plots of Pt $L_3$-edge (a) EXAFS and (b) FT-EXAFS spectra obtained from samples with relatively low (Pt foil) and high (PtFe nanoparticles) background noise. Inset in (b) is an enhanced view of the spectral region used to quantify the noise present in experimental data.

**Table 2.1.** Parameter values and uncertainties (treated as one standard deviation) for FT-EXAFS spectra as determined using various types of software. Uncertainties marked with an asterisk (*) indicate that this parameter was held constant during data fitting.

| Sample | Software | Parameter | | | | | | | | | |
|---|---|---|---|---|---|---|---|---|---|---|---|
| | | $S_0^2$ / a.u. | | $CN$ / a.u. | | $R$ / Å | | $\sigma^2$ / $10^{-3}$ Å$^2$ | | $\Delta E_0$ / eV | |
| Pt Foil (Low Noise) | WinXAS | 0.910 | ± 0.002 | 12 | ± 0* | 2.7687 | ± 0.0001 | 4.27 | ± 0.01 | 5.6 | ± 0.02 |
| | Artemis | 0.96 | ± 0.05 | 12 | ± 0* | 2.769 | ± 0.002 | 4.6 | ± 0.3 | 5.5 | ± 0.5 |
| | Analyzer v0.1 | 0.91 | ± 0.03 | 12 | ± 0* | 2.769 | ± 0.002 | 4.3 | ± 0.2 | 5.6 | ± 0.4 |
| PtFe Nanoparticles (High Noise) | WinXAS | 0.910 | ± 0* | 4.0 | ± 0.2 | 2.752 | ±0.002 | 2.8 | ± 0.3 | 5.2 | ± 0.5 |
| | Artemis | 0.96 | ± 0* | 3.8 | ± 0.6 | 2.760 | ± 0.008 | 2.8 | ± 0.8 | 5 | ± 2 |
| | Analyzer v0.1 | 0.91 | ± 0* | 4.0 | ± 0.6 | 2.752 | ± 0.006 | 2.8 | ± 0.9 | 5 | ± 1 |

## 2.2 Complementary Nanoparticle Characterization Techniques

### 2.2.1 Transmission Electron Microscopy

The small size of nanoparticles places them beyond the resolution of traditional optical microscopy. The limit on spatial resolution in microscopy is determined by the Rayleigh criterion, as defined according to the following equation:

$$\Delta l = 1.220 \frac{f_o \lambda}{D}, \tag{2.6}$$

wherein $\Delta l$ is the point-to-point resolution, $f_o$ is the objective focal length of the microscope, $\lambda$ is the wavelength of light passing through the lens, and $D$ is the diameter of the lens.[89] Although instrumental limitations from focal length and lens diameter are also a factor, spatial resolution in optical microscopy is fundamentally limited by the ability of the human eye to detect only visible light. This limit is determined by the Abbe diffraction limit: [90,91]

$$a = \frac{\lambda}{2n \sin\theta} = \frac{\lambda}{2(NA)}, \tag{2.7}$$

Wherein $\lambda$ is the wavelength of light being diffracted, $n$ is the refractive index of the material at the given wavelength, $a$ is the diameter of the illuminated sample area, and $NA$ is the numerical aperture ($n \sin\theta$), which has a maximum value of *ca.* 1.5 in modern instruments. Because human vision is limited to the visible spectrum, optical microscopy has an inherent, diffraction-limited resolution of *ca.* 200 nm.[90,91] Thus, it is necessary to use alternative methods to achieve resolution suitable for the characterization of nanoparticles.

The construction of the first transmission electron microscope by Knoll and Ruska allowed the barrier set by optical microscopes to finally be overcome.[92] TEM imaging is largely analogous to optical microscopy, with a few notable differences. Instead of using optical photons, a beam of electrons is generated by a thermionic filament and accelerated towards a sample using a strong electric field.[93] Due to the fact that electrons, like all subatomic particles, also exhibit wave-like properties, they can be used to image samples much as photons are used. The equation

$$\lambda_e = \frac{h}{\sqrt{2m_e E_{\mathrm{k}}}} \tag{2.8}$$

describes the relationship between the wavelength, $\lambda_e$, and kinetic energy of an electron, $E_{\mathrm{k}}$, with $h$ being the Planck constant.[94] Furthermore, while diffraction limitations also apply to electrons, the fact that electron detectors can accommodate very high energies allows for much shorter wavelengths than can be achieved using photons.[94]

A simple schematic diagram of a transmission electron microscope is presented in Figure 2.7. Unlike photons, electrons cannot be refracted using conventional optical lenses;

instead, they must be collimated and focused using "magnetic lenses" consisting of carefully controlled electromagnetic fields.[95,96] Electrons generated by the thermionic filament are first accelerated using a high applied voltage (on the order of $10^{-4}$ to $10^{-5}$ V) and then collimated by the condensing lens. The resulting focused beam of electrons passes through the sample, being partially scattered by the electrons therein; those electrons which are transmitted through the sample are then refocused by the objective and projection lenses onto a phosphor or charge-coupled device screen for detection to create an image.[93,96] The much-enhanced point-to-point resolution afforded by this technique relative to optical microscopy has allowed for TEM imaging to be routinely used in the characterization of nanoparticles.

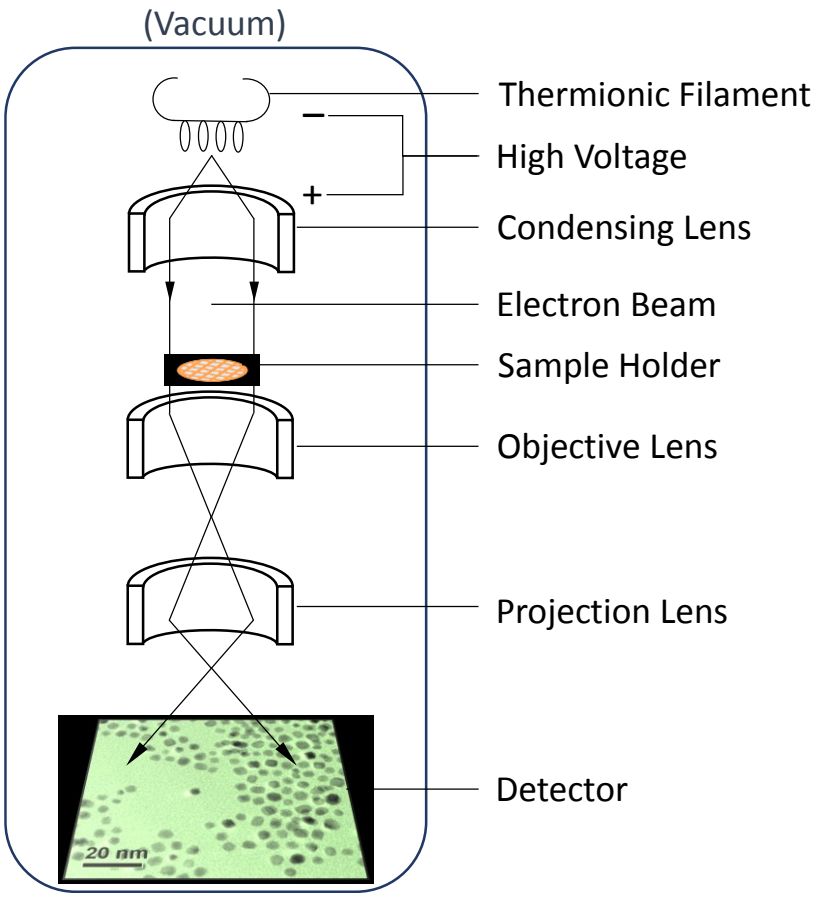


**Figure 2.7.** Simple schematic diagram of a transmission electron microscope. The major components and path of the electron beam are indicated.

Finally, some TEM instruments can also be used to gather information regarding the elemental compositions of samples by performing energy-dispersive X-ray spectroscopy (EDS) measurements. For these measurements, X-ray emission occurs when electrons within the sample material are excited to higher energy states by the incident electron beam; as these electrons relax back to the ground state, they may emit X-ray photons via fluorescence mechanisms.[97] The X-ray photons emitted from the sample material are then differentiated based on their energies using a specialized detector.[97] Using this technique allows for a quick measurement of the elemental composition of a sample, and can even allow for elemental mapping of sufficiently large nanoparticles.[94,98,99] In order to obtain more specific information regarding the surface structure and electronic properties of nanoparticles, however, other analytical techniques are required.

### 2.2.2 Ultraviolet-visible Spectroscopy

UV-vis spectroscopy is a simple bench-top analytical technique that is frequently employed in both the identification and quantification of chemical samples.[100–102] This technique is often used to study the absorption and fluorescence arising from nanoparticles or nanoclusters that exhibit optical properties;[101] however, it can also be useful for studying the reactions of organic molecules at catalyst surfaces.[100] Although advances in the portability and quality of UV-vis systems continue to be made,[102] the underlying principles are universal.

In UV-vis spectroscopy, an absorption event occurs when the energy of an incident photon matches the difference in energies between a ground-state electron and a corresponding higher-energy ("excited") state.[103] The magnitude of absorption that occurs is described by the Beer-Lambert law,

$$A = \log\left(\frac{I_0}{I}\right) = \varepsilon bc, \tag{2.9}$$

wherein $A$ is the measured absorption, $I$ is the intensity of light transmitted through the sample, $I_0$ is the intensity of light incident on the sample, $\varepsilon$ is the molar attenuation coefficient of the absorbing species, $c$ is the concentration of the species in the sample, and $b$ is the path length of the cell.[104,105] Measurements are typically made using a linear cell geometry, as shown in Figure 2.8.[105] UV-vis absorption techniques performed in this manner can be used to provide insight into the surface structure of nanoparticles whose absorption spectra feature SPR absorption bands.

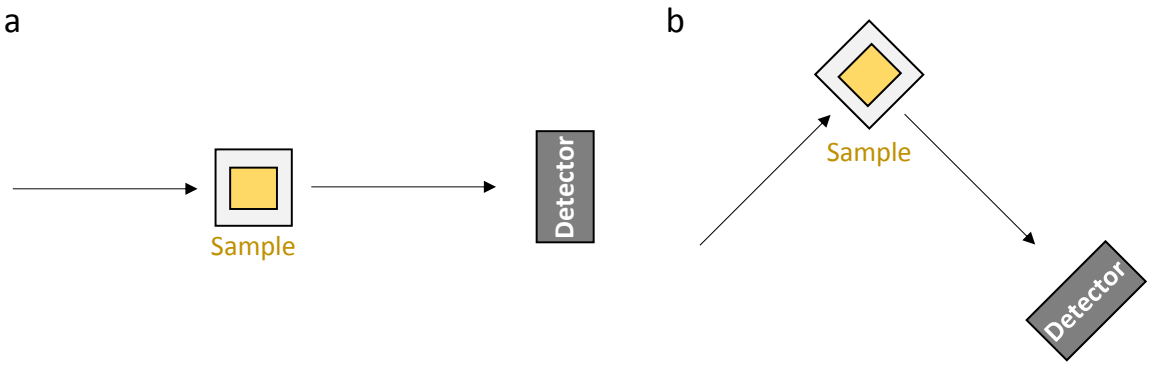


**Figure 2.8.** Common detector geometries used in UV-vis (a) absorption and (b) fluorescence spectroscopy.

It has been well established that the positions of peaks corresponding to SPR absorption are highly dependent on nanoparticle size and geometry.[6] In general, larger particles exhibit greater red-shifting of their SPR peaks.[6] This effect is, perhaps, most evident in the case of metallic nanorods, in which two distinct SPR peaks may be observed: one corresponding to excitations occurring in the longitudinal direction, and one in the lateral direction.[6] Furthermore, in the case of multi-metallic nanoparticles, these bands can become shifted or extinguished due to the presence of atoms with different electronic properties being present at the particle surface.[6,106] While these factors all contribute to the

utility of UV-vis spectroscopy, absorption is not the only mechanism that can be used in the characterization of nanoparticles.

Once generated via photon absorption, excited electrons have several potential processes through which they can lose energy and return to their ground states: vibrational relaxation, external conversion, internal conversion, fluorescence, and phosphorescence all fall into this category.[107] Among these processes, fluorescence (releasing energy via emission of a photon) is most commonly used to characterize samples.[108] In order to minimize interference from transmitted or scattered photons in the fluorescence signal, the detector is oriented perpendicular to the incident photon beam (as shown in Figure 2.8).[108] Because the spectra obtained from UV-vis fluorescence spectroscopy arise from electronic transitions, they can provide information about electronic energy levels that is complementary to UV-vis absorption data.[108] This is especially useful in the study of very small nanoclusters, which can exhibit interesting optical properties as a result of metal-ligand charge transfer and related phenomena.[109,110] Many catalytically active metal nanoparticles, including those constituted of Pt, do not exhibit interesting optical behaviour; the electronic properties of these nanoparticles are, thus, better characterized using alternative techniques.

### 2.2.3 Cyclic Voltammetry

Electrochemical techniques are useful tools for the analysis of nanoparticles, particularly those intended for use in catalytic applications, and can provide information complementary to that obtained using XAS.[63] It has long been known that electrochemical techniques like CV are well-suited for the characterization of surface structure in noble metal alloys.[111] Fortunately for nanoparticle researchers, this

applicability also extends to characterizing the surfaces of noble metal nanoparticles.[17] In addition to providing measurements of catalytic activity and electrochemically active surface areas (ECSAs), CV can also be used to probe substrate binding affinities, providing insight into reactions occurring at catalyst surfaces.[27,112] The following section specifically addresses the use of CV in the characterization of electrocatalysts relevant to the ORR and formic acid oxidation (FAO) reaction.

Overpotential, $\eta$, is the difference between the potential applied to an electrode, $E_a$, and the equilibrium potential of a redox couple, $E_e$, as described by the equation

$$\eta = E_a - E_e. \tag{2.10}$$

Overpotential is a very strong driver of electrochemical reactions, with values on the order of $10^2$ to $10^3$ mV being able to effect tenfold increases in the observed current densities of a given reaction.[113] The dependence of current density, $j$, on overpotential is often described using the Tafel equation:

$$\log j = \log j_0 \pm \frac{\alpha n_e F}{2.3 R_G T}\eta, \tag{2.11}$$

wherein $j_0$ is the (non-zero) exchange current density (*i.e.*, current density when $\eta = 0$), $\alpha$ is the charge transfer coefficient, $n_e$ is the number of electrons transferred in the reaction, $F$ is the Faraday constant, $R_G$ is the ideal gas constant, and $T$ is the temperature; the term immediately preceding $\eta$ is positive for anodic reactions and negative for cathodic reactions.[113] When the logarithm of current density is plotted against overpotential, extrapolation of the linear region to its point of intersection with the logarithmic current density axis yields the value of $\log(j_0)$ for the reaction. The slope of the linear region is the Tafel slope and affords additional information regarding the mechanism of the electrochemical reaction. Finally, overpotential also plays an important role in the cell

voltage of a fuel cell, $V_{cell}$, as follows:

$$V_{cell} = \Delta E_e - \eta_a - \eta_c - IR, \tag{2.12}$$

wherein $\Delta E_e$ is the difference between the equilibrium potentials of the anodic and cathodic redox couples, $\eta_a$ is the anodic overpotential, $\eta_c$ is the cathodic overpotential, and $IR$ is the voltage drop due to the resistance of the electrolyte solution.[113]

When discussing reactions at electrode surfaces, at least three keys steps are involved: mass transport of the reactant species to the electrode surface, electron transfer between the electrode and the reactant species, and mass transfer from the electrode surface back to solution.[113] In reality, reactions may be significantly more complex than this and could involve processes such as adsorption to the electrode surface, bond breakage/formation, multiple electron transfer, and phase formation. For electrocatalysts, adsorption is often an important factor, as it can serve to reduce reaction overpotentials by decreasing reaction energy barriers and/or providing alternate reaction pathways.[113] It is important to note that because many catalytic reactions involve both the formation and breaking of adsorption bonds, intermediate binding site-reactant bond strengths are actually preferable over very strong interactions.[113] If the bonds formed are too strong, the product molecule will be difficult to dissociate from the binding sites and remain bound, blocking further reactivity; conversely, if the bonds are too weak, the reactant will not interact as strongly with the binding sites, thereby also resulting in decreased reactivity. Characterization of these electrode reactions can be conveniently performed via CV experiments.

CV experiments can be used to provide both qualitative and quantitative information regarding the reactions occurring at an electrode surface.[113] A three-

electrode setup is commonly employed in CV experiments that study materials with potential electrocatalytic applications, as illustrated in Figure 2.9.[37,114,115] When it is necessary to control the gas content of an electrolyte solution, a gas bubbler or diffuser is used to purge the solution with a reactive (*e.g.*, $O_2$ for measuring ORR activity) or inert (*e.g.,* Ar for determining ECSAs) gas, as required for the experiment being performed.[115] The use of a variety of reference electrodes can be found in the literature; when using CV to study Pt-based electrocatalysts, however, using a Pt wire or mesh for the counter electrode is common procedure. While a number of reference electrodes should perform satisfactorily, those containing chloride or other strongly adsorbing counterions may have a negative effect on the catalytic activity of Pt-based materials and are not recommended for such studies.[116,117]

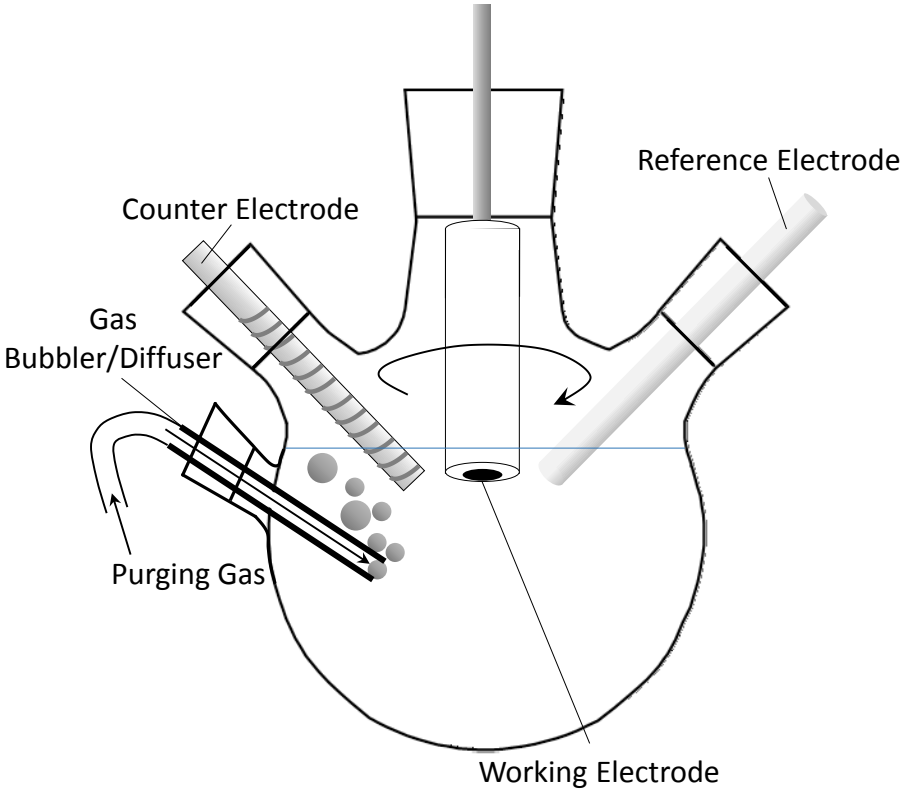


**Figure 2.9.** Simple schematic illustrating the important components of a typical three-electrode setup: RDE working electrode, Pt counter electrode, reference electrode, and gas bubbler/diffuser.

Finally, the working electrode used in the measurement of electrocatalytic activity is often a glassy carbon rotating disk electrode (RDE), onto which nanoparticle samples are deposited for characterization.[115] When nanoparticle electrocatalysts are characterized using CV, they are often first deposited onto a support material in order to promote their electrical conductivity and prevent particle aggregation. This support is often a simple carbon black powder, but various other materials may also be used, including graphene, carbon nanotubes, and metal oxides.[16,19]

Both the ORR and, to a lesser extent, the FAO reaction are of particular research interest due to their applicability to fuel cell systems.[38,118] Such experiments are performed under conditions very similar to those used for simple CV experiments, except that the fuel molecule is added to the electrolyte solution.[46] In the ORR, this means saturating the electrolyte solution with bubbled $O_{2(g)}$, whereas the FAO reaction requires preparing a solution containing both the electrolyte and formic acid fuel at the correct concentrations.[46] Once the electrochemical setup is ready, data acquisition can begin.

In a CV experiment, the potential applied to the working electrode is swept linearly from a low potential to a high potential and back, as illustrated in Figure 2.10a.[119] At each step in this potential sweep, the resulting current is measured, thereby providing insight into the reactions occurring at the surface of the working electrode.[119] A representative cyclic voltammogram obtained using a commercial Pt/C catalyst material (HiSPEC 3000) is shown in Figure 2.10b. Characteristic peaks corresponding to hydrogen desorption (*i*), surface oxide formation (*ii*), and surface oxide reduction (*iii*) are indicated.[120,121] These regions can be used to infer information regarding the surface structure of catalysts, including their respective ECSAs.[122]

As an example of catalytic activity measurement using CV, a typical

voltammogram obtained from this Pt/C catalyst in electrolyte solution containing 0.1 M formic acid is presented in Figure 2.10c. The drastic increase in peak intensity from the forward sweep (*iv*) to the reverse sweep (*v*) following the stripping of CO from the electrode surface (*vi*) reflects the significance of surface poisoning by CO, which is a major obstacle to the use of Pt in catalyzing the reactions of small molecules like formic acid and methanol.[37,118] These results thus provide invaluable insight into the reactions occurring at nanoparticle surfaces.

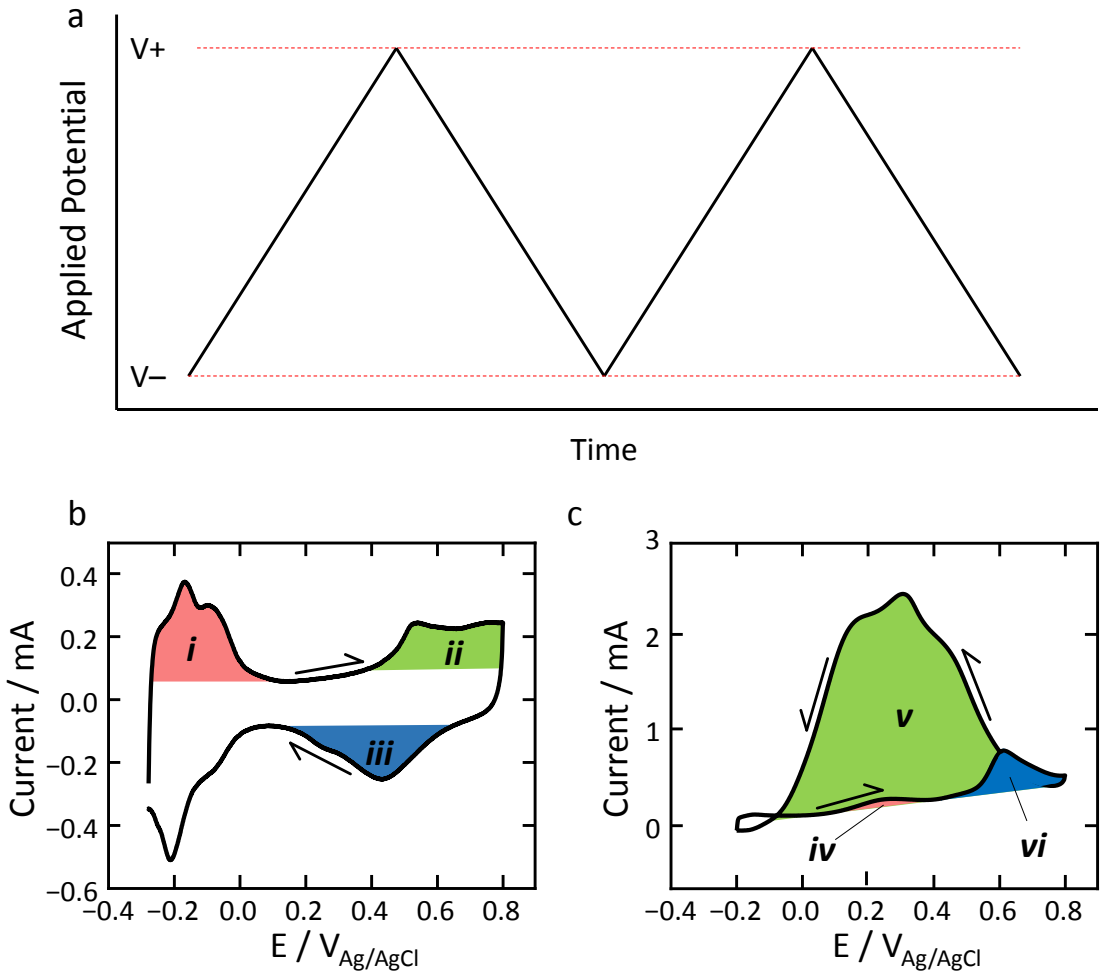


**Figure 2.10.** (a) Illustration of the linear voltage sweeps used in CV measurements, and representative voltammograms obtained from a commercial Pt/C catalyst in $Ar_{(g)}$-saturated (b) perchloric acid and (c) perchloric acid/formic acid electrolyte solutions. Highlighted regions indicate (a) peaks due to (*i*) hydrogen desorption, (*ii*) partial Pt surface oxidation, and (*iii*) Pt surface reduction reactions on the Pt/C catalyst; and (b) FAO activity on the (*iv*) forward and (*v*) reverse potential sweeps, as well as (*vi*) a significant peak corresponding to surface poisoning by CO.

# Chapter 3 – Local Structure of Fluorescent Pt Nanoclusters

Adapted with permission from Reference 119:
Reproduced by permission of the Royal Society of Chemistry
Duchesne, P.N.; Zhang, P. "Local Structure of Fluorescent Platinum Nanoclusters"
*Nanoscale,* **2012**, *4* (14), 4199-4205.


## 3.1 Contributions

PND synthesized the Pt nanoclusters, acquired and analyzed UV-vis absorption and fluorescence spectroscopy data, acquired and analyzed XAS data, and wrote the manuscript. PZ supervised PND and helped with manuscript revision.

## 3.2 Foreword

One relatively recent development in the field of nanoparticles has been the controlled synthesis of increasingly small particles. These "nanoclusters" tend to have discrete atomic compositions, and can exhibit behavior not observed in larger nanoparticles. This chapter focuses on determining the structure of Pt nanoclusters prepared using a simple and convenient method. The suitability of XAS techniques for characterizing these materials is demonstrated, and methods are developed for application to future nanoparticle samples.

## 3.3 Introduction

Recent experiments have revealed that some small metal nanoparticles exhibit unexpected optical fluorescence behaviour;[26,124–126] these nanoparticles are often referred to as "nanoclusters" due to the fact that they are smaller than 2 nm in diameter, and so approach the scale of molecular clusters sometimes observed in the field of inorganic

chemistry.[127,128] For such nanomaterials, the conduction band structure seen in bulk metals breaks down as the number of atoms in the cluster is reduced, resulting in the formation of discrete electronic energy levels and giving rise to their optical fluorescence.[129] Metal nanoparticles and fluorescent nanoclusters composed of Ag, Au , Pd, and Pt have recently been prepared using a simple, "surfactant-free" approach that employs N,N-dimethylformamide (DMF) as both the surface-protecting ligand and reducing agent, in addition to its more common role as a solvent.[26,124,125,130] Based on preliminary experimental results, applications of such nanoclusters have been suggested in promising fields such as bio-detection and catalysis.[26,124,125]

Various characterization methods have been employed in the study of these nanoclusters, but uncertainty still remains regarding their local structure. It was hypothesized that XAS could be a very useful technique for addressing this issue. To this end, Pt $L_3$-edge XAS measurements were conducted for a series of fluorescent Pt–DMF nanoclusters prepared using the aforementioned "surfactant-free" approach. By implementing EXAFS and XANES techniques in conjunction with UV-vis absorption and fluorescence spectroscopies, the local structures and oxidation states of the samples were investigated. While not strictly related to the catalytic applications of bimetallic Pt nanoparticles, studying these simpler, monometallic nanoclusters provided an opportunity to obtain better familiarity XAS techniques and the extent to which it can be used to infer structure-property relationships in nanoparticles.

## 3.4 Experimental Methods

### 3.4.1 Materials

Hydrogen hexachloroplatinate(IV) hexahydrate (99.9%, Alfa Aesar), N,N-dimethylformamide (ACS Grade, ACP Chemicals, Inc.), and acetonitrile (laboratory grade) were used in this reaction. De-ionized water (18.2 MΩ·cm) was obtained from a Barnstead NANOpure® DIamond™ UV water purification system. All reagents and solvents were used as received, without further purification.

### 3.4.2 Synthesis

Samples were synthesized following the procedure outlined by Kawasaki *et al.*[26] In accordance with this procedure, 200 mL of DMF were placed in a 250 mL round-bottom flask attached to a reflux condenser and heated to 140 °C while being stirred magnetically at 600 RPM. A quantity of 0.2 mmol $H_2PtCl_6 \cdot 6H_2O$ (*i.e.*, the Pt precursor) was then dissolved in 2 mL of de-ionized water and added to the pre-heated DMF. Aliquots of 50 mL were removed from the flask after 2, 4, 8, and 24 h of reaction time. After cooling, a small amount of solution (1 mL) was taken from each aliquot for analysis using UV-vis absorption and fluorescence spectroscopic techniques before being recombined with the remainder of the aliquot. Each aliquot was vacuum dried on a Schlenk line equipped with a solvent trap before being finally transferred to a small sample vial and stored under argon to prevent oxidation. The 0 h sample was obtained by dissolving a small amount of the precursor material in de-ionized water.

### 3.4.3 UV-vis Spectroscopy

UV-vis absorption spectra were recorded using a Cary 100 Bio UV-visible spectrophotometer and fluorescence spectra were recorded using a Cary Eclipse

Fluorescence Spectrometer, both by Varian, Inc.). For each sample, 1 mL of the reaction mixture was diluted using DMF in a 1 cm path length quartz cuvette to a total volume of 3 mL. UV-vis absorption spectra were recorded over the range of 200 to 700 nm and fluorescence scans were performed using excitation wavelengths from 300 to 600 nm (with a step size of 10 nm) and a recorded emission spectrum from 300 to 700 nm. Background subtraction was performed using a de-ionized water or DMF standard, as appropriate.

### 3.4.4 X-ray Absorption Spectroscopy

Pt nanocluster samples were prepared for XAS analysis by dissolving the dried materials in approximately 2 mL acetonitrile. These diluted suspensions were then transferred to Teflon® liquid-sample cells equipped with Kapton® film windows to facilitate transmission of the X-ray beam.

Samples were analyzed using the Sector 20-BM beamline of the Advanced Photon Source at Argonne National Laboratory in Argonne, IL. A standard transmission mode configuration was employed, with an in-line metal reference foil used for energy calibration. X-ray monochromation was performed using a Si(111) double-crystal monochromator in conjunction with a rhodium-coated silicon focusing mirror; in order to help reject higher harmonics of the selected wavelength, the mirror was detuned to pass only 60% of the incident beam intensity.

Data processing for both EXAFS and XANES analyses was performed using the commercial software WinXAS.[76] In order to obtain meaningful information from the EXAFS data, it was necessary to reduce the number of free-running parameters in the fitting algorithm by making some reasonable assumptions. Based on a knowledge of the

reaction mixture composition and exploratory fitting of the FT-EXAFS spectra, it was determined that the two primary scattering paths observed in the experimental spectra could be identified as Pt–O/N and Pt–Cl interactions, with determined bond lengths of *ca.* 2.01 Å and *ca.* 2.32 Å, respectively.[131–134] Distinguishing between paths arising from Pt–O and Pt–N scattering interactions was impossible due to the similarities in size and atomic number between these two elements, and so a single path (referred to hereafter as Pt–O) was used to account for both.

The $\sigma^2$ values of the Pt–O and Pt–Cl scattering paths were then assumed to be equal, an effective approach demonstrated by W.A. Spieker *et al.* in their study of $H_2PtCl_6 \cdot 6H_2O$ speciation in aqueous media using EXAFS analysis.[134] Likewise, the $\Delta E_0$ values for the Pt–Cl and Pt–O paths were also assumed to be equal, based on the fact that values for these parameters should be similar in any reliable fitting of experimental data.[80] Furthermore, the sum of Pt–O and Pt–Cl *CN*s for the 0 h sample was fixed at 6 (full coordination for the octahedral $Pt^{4+}$ complex) in order to obtain an appropriate $S_0^2$ value.[134] Applying this $S_0^2$ value to subsequent samples, however, resulted in unreasonable total *CN*s. Due to the fact that XANES results (*vide infra*) suggested that all of the nanocluster samples exist as $Pt^{2+}$ species, a second $S_0^2$ value was determined for the $Pt^{2+}$ complexes observed in later samples by assuming a total *CN* of 4 for the 24 h sample (the optimal number for such a square planar complex).

## 3.5 Results and Discussion

### 3.5.1 UV-vis Spectroscopy

UV-vis absorption and fluorescence spectra were recorded as the reaction

progressed and are depicted in Figure 3.1. Strong similarities were observed between these experimental results and those reported in the literature, indicating that the correct product had been obtained.[26] As the reaction progressed, the peak at *ca.* 460 nm in the UV-vis spectrum of the precursor material quickly disappeared and was replaced by a broad absorption at shorter wavelengths (*ca.* 400 nm) that gradually increased in intensity. For the fluorescence spectra, a broad, low-intensity peak slowly developed at *ca.* 470 nm during the course of the reaction. Whereas the peak width remained largely unchanged, this peak continually increased in intensity while becoming slightly red-shifted as the reaction progressed. This red-shifting may have been a result of the changes in coordination environment and oxidation state suggested by EXAFS and XANES analyses.

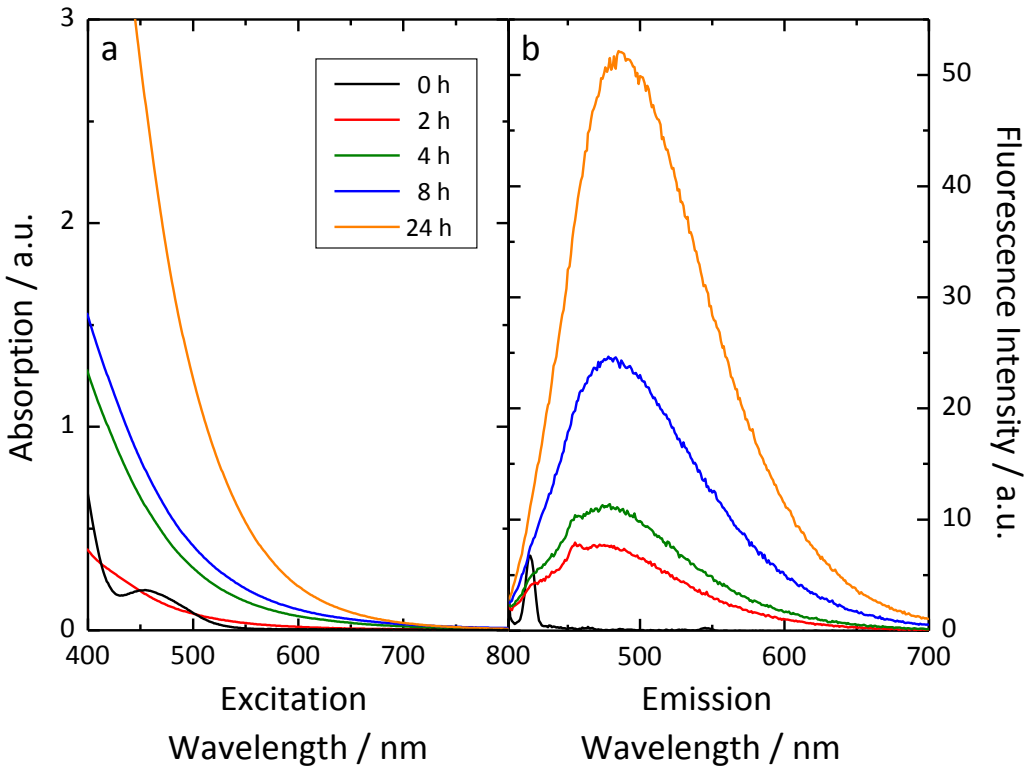


**Figure 3.1.** Plots of UV-vis (a) absorption and (b) fluorescence spectra obtained from as-synthesized fluorescent Pt nanoclusters in DMF after having cooled to room temperature. The small peak near 420 nm in the 0 h fluorescence spectrum is due to scattering of the excitation beam. Adapted with permission from Reference 119.

### 3.5.2 EXAFS Data Analysis

XAS measurements were performed on sample aliquots isolated from the reaction vessel after various lengths of time. For the purpose of qualitative comparison, Figure 3.2 shows the isolated EXAFS spectra for these samples. In general, the amplitude of each spectrum is proportional to the coordination number of the absorbing atom, but is also affected by constructive and destructive interference resulting from electrons backscattering from different atoms within the sample.[135] As a result, a decrease in coordination number could be inferred from the amplitude reduction observed between the precursor material and the longer-duration samples; however, in order to quantify this observation, a more thorough analysis of the FT-EXAFS is required.

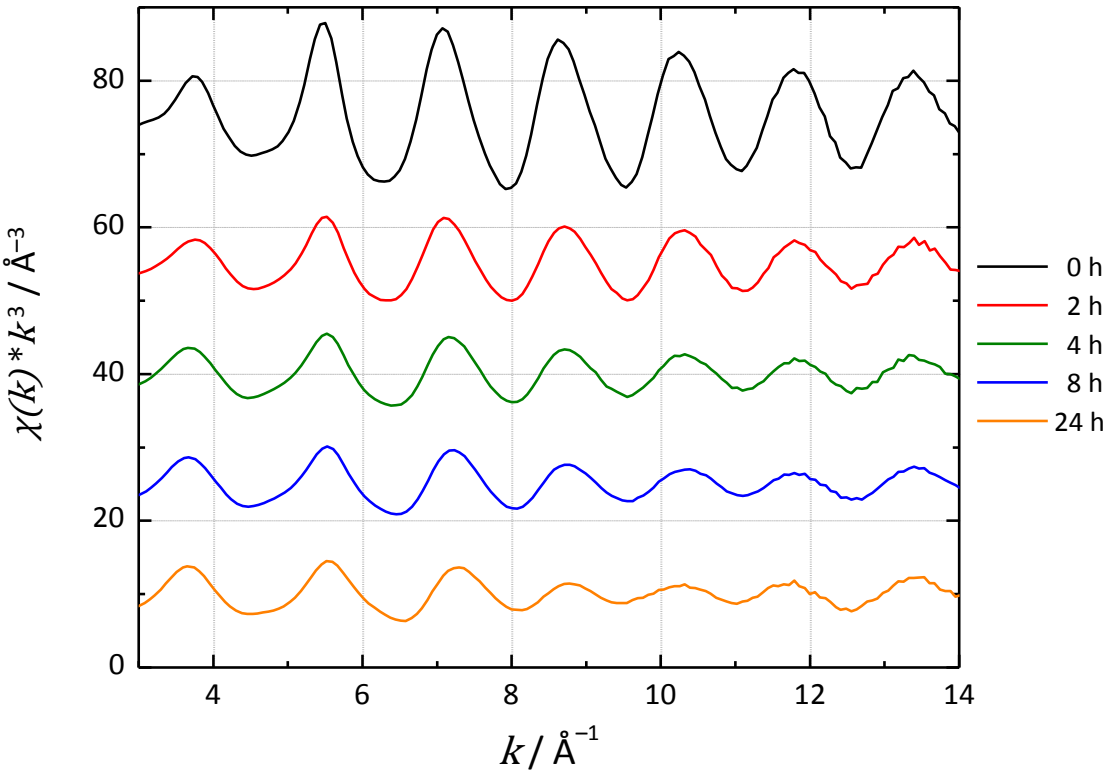


**Figure 3.2.** EXAFS spectra ($k^3$-weighted) obtained via absorption measurements at the Pt $L_3$-edge. Fluorescent Pt nanoclusters prepared with various reaction times were dissolved in acetonitrile prior to performing these measurements. Adapted with permission from Reference 119.

A comparison of the FT-EXAFS spectra is provided in Figure 3.3. Two dominant peaks are observed in each spectrum at *ca.* 1.5 Å and 2 Å, corresponding to Pt–O and Pt–Cl scattering paths, respectively. From these spectra, it can be qualitatively seen that the degree of Pt–Cl coordination had undergone a rapid initial decrease by the two hour mark, followed by a slower continuous decrease in successive samples. A slow, simultaneous increase in Pt–O coordination was also observed, indicating a gradual replacement of the initially-present chloride by nitrogen- or oxygen-containing species.

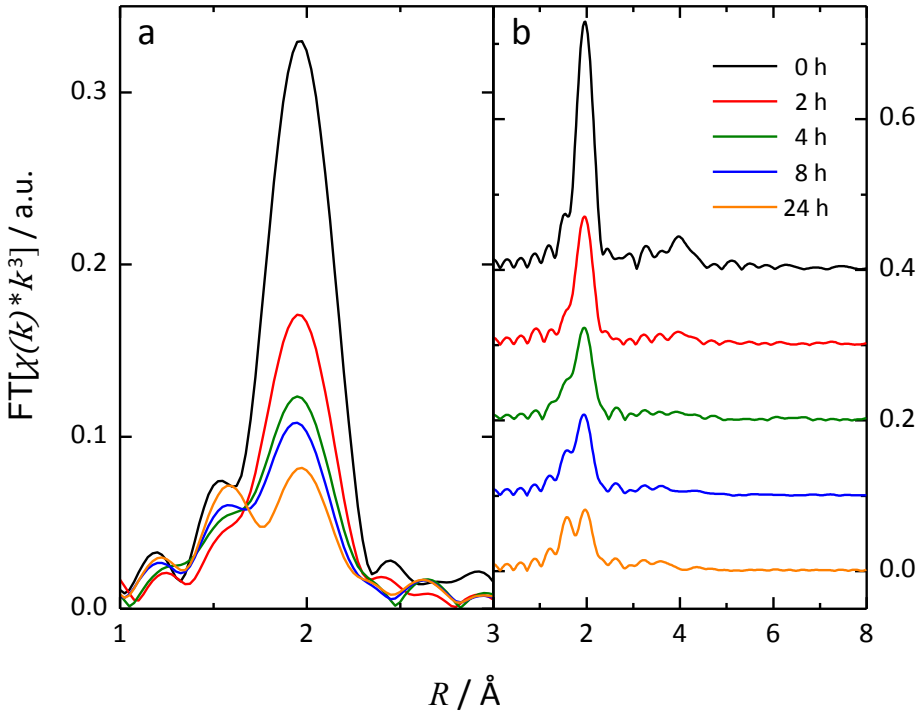


**Figure 3.3.** (a) Overlapped and (b) offset FT-EXAFS spectra ($k^3$-weighted) obtained from Pt $L_3$-edge EXAFS spectra. Adapted with permission from Reference 119.

Fitting results for samples isolated after various reaction times are shown in Figure 3.4. Good agreement was observed between the experimental data and fitted equations in all samples. It is important to note that these fits were performed only over a region of interest between 1.25 Å to 2.33 Å. Physical parameter values extracted in the course of this process are presented in Table 3.1. The associated uncertainties were determined using Analyzer v0.1 software, as described in Section 2.1.6.

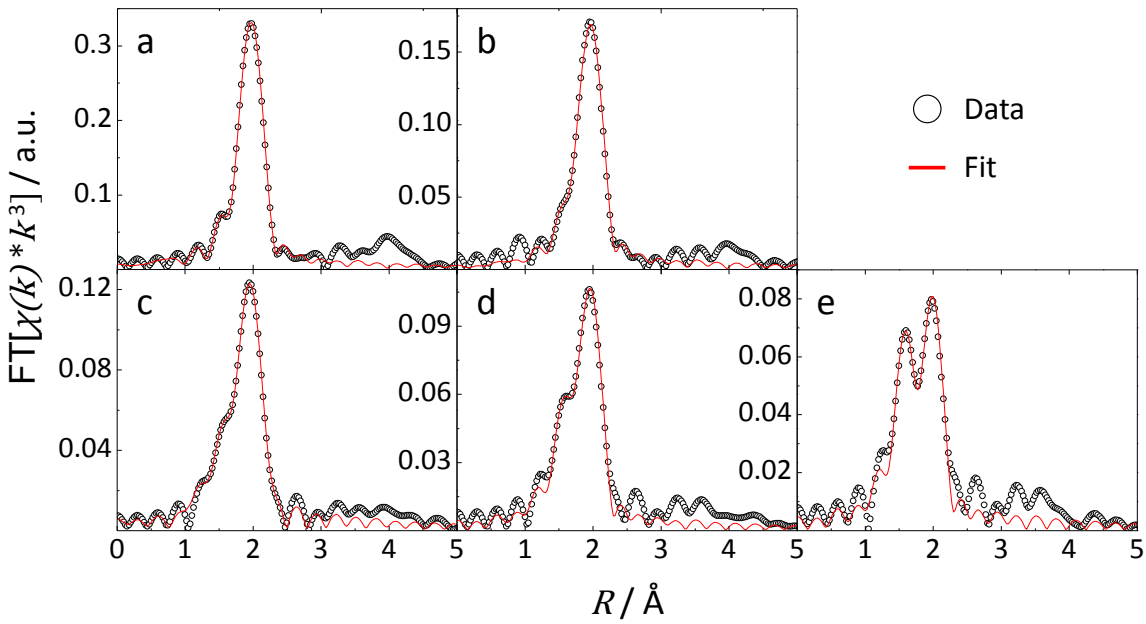


**Figure 3.4.** Experimental and fitted Pt $L_3$-edge FT-EXAFS spectra of Pt nanocluster samples prepared over the course of (a) 0, (b) 2, (c) 4, (d) 8, and (e) 24 hours. Adapted with permission from Reference 119.

**Table 3.1.** Values obtained for *CN*, *R*, $\sigma^2$, and $\Delta E_0$ parameters via fitting of Pt $L_3$-edge FT-EXAFS spectra. Uncertainties in the last decimal place of each value are indicated in parentheses (treated as one standard deviation). Values indicated by an asterisk (*) indicate a shared uncertainty, due to these values being correlated to a maximum total CN of 6. Adapted with permission from Reference 119.

| Reaction Time / h | Scattering Path | *CN* / a.u. | *R* / Å | $\sigma^2$ / $10^{-3}$ Å$^2$ | $\Delta E_0$ / eV |
|---|---|---|---|---|---|
| 0 | Pt–O | 1(1)* | 2.11(9) | 2.8(9) | 5(2) |
| | Pt–Cl | 5(1)* | 2.325(9) | | |
| 2 | Pt–O | 0.8(3) | 2.08(2) | 2.7(5) | 5.6(8) |
| | Pt–Cl | 3.6(4) | 2.318(4) | | |
| 4 | Pt–O | 1.5(2) | 2.03(2) | 3.1(8) | 4(1) |
| | Pt–Cl | 2.9(4) | 2.309(5) | | |
| 8 | Pt–O | 1.7(3) | 2.02(2) | 3(1) | 3(2) |
| | Pt–Cl | 2.5(4) | 2.305(7) | | |
| 24 | Pt–O | 2.2(1)* | 2.001(7) | 2.9(6) | 3(1) |
| | Pt–Cl | 1.8(1)* | 2.303(6) | | |

In order to better illustrate trends in these data, important structural parameters (*CN*, *R*, and $\sigma^2$) and their corresponding uncertainties are plotted in Figure 3.5. As suggested qualitatively by the EXAFS spectra, an abrupt reduction in total *CN* was initially observed due to a significant reduction in *CN* for the Pt–Cl scattering path. This is indicative of a reduction of the octahedral $Pt^{4+}$ precursor species to some $Pt^{2+}$ species, which (as a $d^8$ Pt-group metal) should prefer a four-coordinate square-planar geometry.[136] In terms of bond length, a slight reduction seemed to occur for both scattering paths, although the effect was more pronounced for Pt–O than Pt–Cl bonds. This likely represents a change from the initial coordination by water molecules to coordination by other O- and N-bearing species as the reaction progresses.[134] The value of $\sigma^2$ is interpreted physically as a measure of the disorder (both static and thermal) within the scattering paths of a sample,[80] with the values for all samples being similar in magnitude.

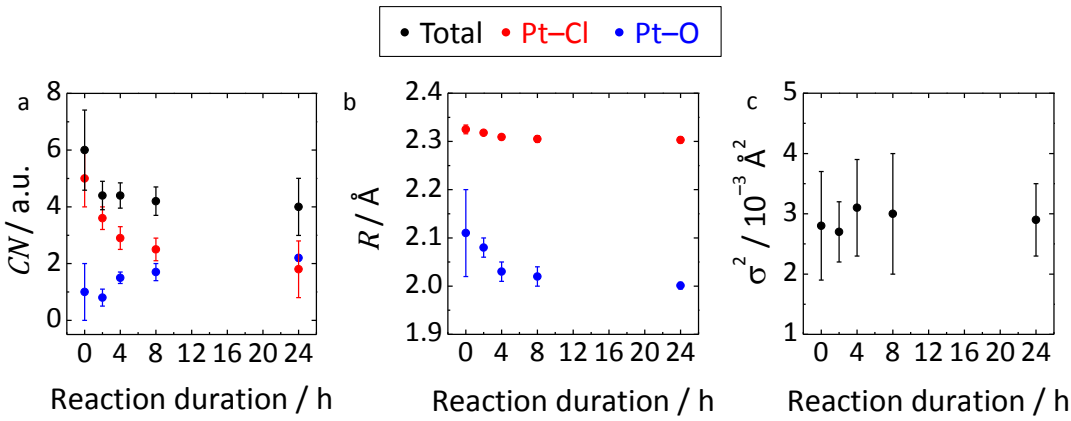


**Figure 3.5.** Plots illustrating the obtained (a) coordination number, (b) bond length, and (c) Debye-Waller factor parameter values and corresponding uncertainties for Pt nanoclusters prepared with different reaction durations. Adapted with permission from Reference 119.

### 3.5.3 XANES Data Analysis

From the comparison of XANES spectra in Figure 3.6a it can be seen that all samples had relatively similar absorption edge profiles; however, as is more clearly shown in Figure 3.6b, a marked decrease in the intensity of both the white line and post-

edge features was observed between the precursor material and the later samples. More quantitative information was obtained from these spectra by integrating the area beneath the white line region of each, according to the method of Sham *et al.*, and then calculating the number of vacancies (or "holes") in the Pt 5d electron orbitals.[137] Except for the 8 h sample, for which only three data points were available, these values were averaged from four independently measured integrals taken over the range $E_0$ − 10 eV to $E_0$ + 10 eV. Calculations were performed by assuming a d-hole count of 4 for the $Pt^{4+}$ precursor species and using a count of 1.334 for the Pt foil reference, as computed by Mattheiss and Dietz.[138]

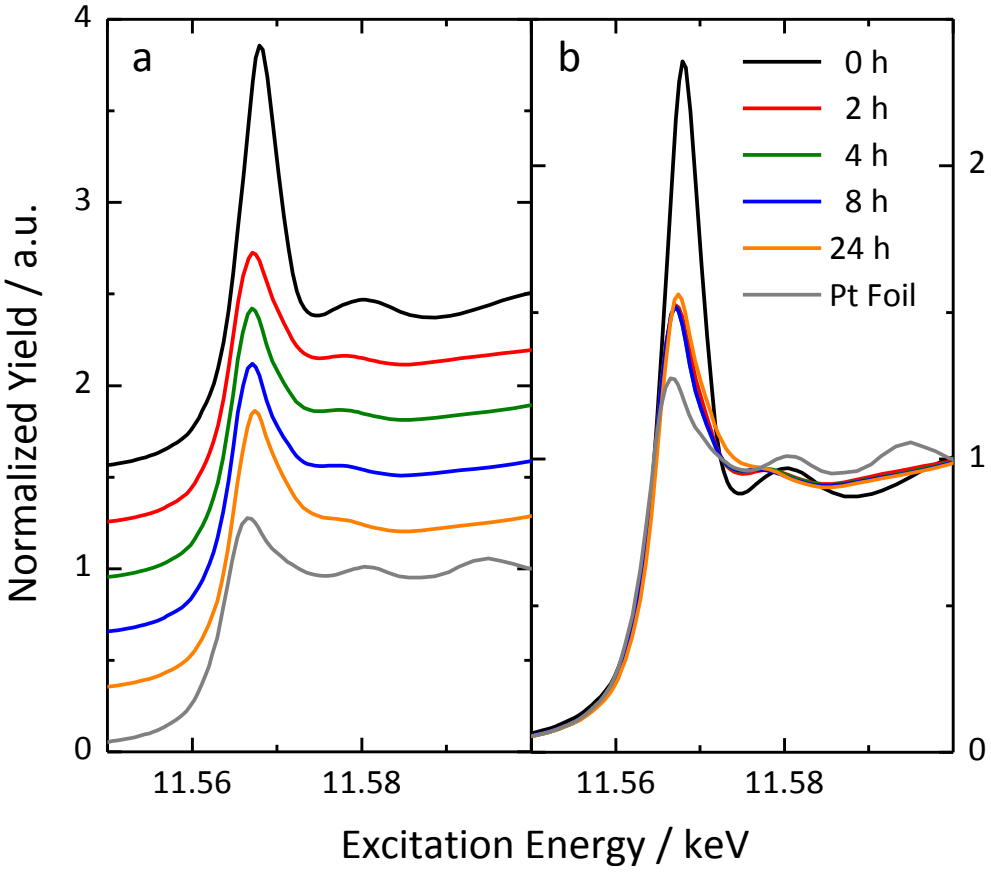


**Figure 3.6.** (a) Overlapped and (b) offset Pt $L_3$-edge XANES spectra obtained from Pt nanoclusters prepared with different reaction durations and a Pt foil reference sample. Reproduced with permission from Reference 119.

As shown in Figure 3.7, all samples except for the precursor material (0 h, with a d-hole count of *ca.* 4) exhibited d-hole counts of *ca.* 2; this result suggests a rapid reduction of the initial $Pt^{4+}$ species to $Pt^{2+}$ in less than 2 h. Additionally, a slight increase in the d-hole count was observed for the 24 h sample, which may indicate the replacement of Pt–N coordination by Pt–O, in which case the more electron-withdrawing, oxygen-containing ligand is coordinated to the Pt centre.

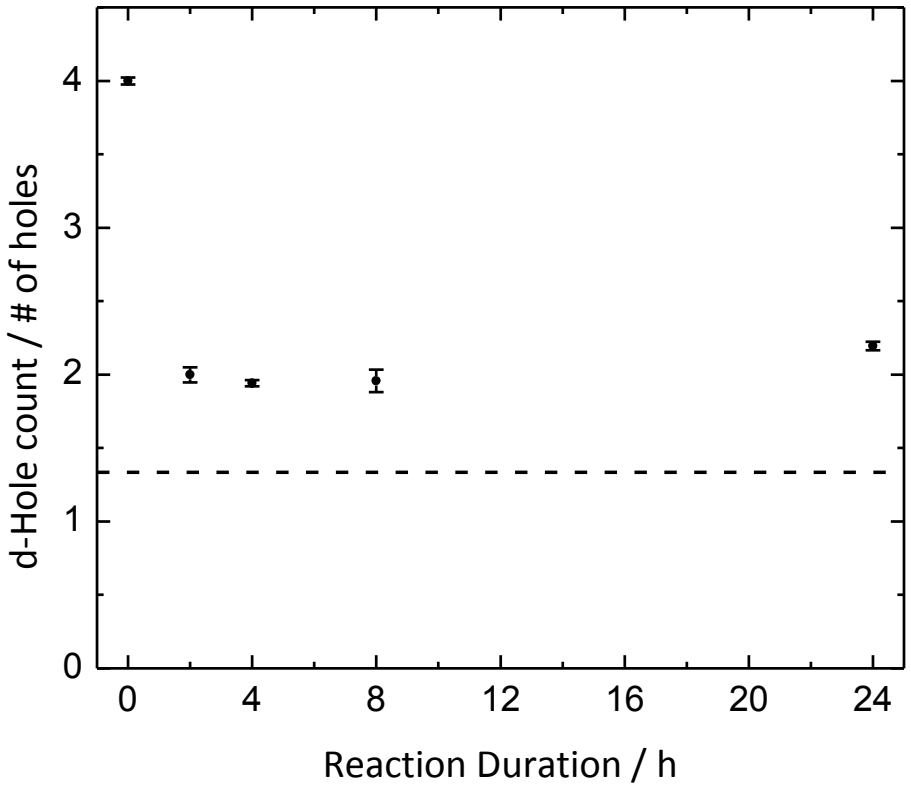


**Figure 3.7.** Calculated d-hole counts for Pt nanocluster samples obtained via integration of the Pt $L_3$-edge white line peak. Error bars indicate the 99% confidence interval for each value. The dashed line represents the computed d-hole count for metallic Pt. Reproduced with permission from Reference 119.

### 3.5.4 Further Discussion

The combined implications of these experimental results are interesting enough to warrant further discussion here. Both the optical absorption and fluorescence peaks increased in intensity as the reaction progressed, and a red-shift was observed in the emission spectra from samples taken at later reaction times. Based on this continued

evolution of these spectra, and those obtained from XAS measurements, it appears that the synthetic reaction continued throughout the 24 h duration of the synthesis. The EXAFS and XANES results also indicated a significant reduction in oxidation state from the initial $Pt^{4+}$ precursor salt after just 2 h, based on observed low total Pt *CN*s and reduced white line intensity, respectively.

It seems evident that reduction of the $Pt^{4+}$ precursor to $Pt^0$ was not achieved, as the XANES spectra indicate that all samples were still oxidized relative to metallic Pt. Notably, it has been reported that DMF is a very weak reducing agent, and is unable to convert $Pt^{4+}$ to $Pt^0$ under ambient conditions without requiring many days of reaction time.[139] Further supporting this observation is the notable absence of a significant contribution from Pt–Pt scattering paths in the FT-EXAFS spectra (attempts to fit Pt–Pt scattering paths to the experimental data inevitably failed despite repeated attempts to overcome the problem).

It is important to realize that nanoclusters such as these, containing only a few atoms in total, will not exhibit the separate metallic core and molecular surface binding modes as larger clusters (*e.g.*, $Au_{25}$, $Au_{38}$, and $Au_{144}$).[140] However, even if each atom is effectively a member of the surface and no metallic core exists, interactions between adjacent surface Pt atoms should still contribute to a measurable Pt–Pt peak in the FT-EXAFS spectrum.[141] It is worth noting, though, that marked deviations of the metal–metal bond lengths (relative to those seen in the corresponding bulk metals) may be observed in very small clusters.[142–144] When all the aforementioned evidence is taken into consideration, it seems logical to conclude that the products of this synthesis are not metallic, but more closely resemble an inorganic complex.

Due to the fact that XAS spectra represent an average of all atomic environments

for the element of interest within a sample, it may be that the apparent $Pt^{2+}$ oxidation state is the result of a mixture of $Pt^0$ and $Pt^{4+}$ species. Such an occurrence could also be consistent with *CN* values obtained from the EXAFS refinements if the $Pt^0$ species were less than four-coordinate in nature. A three-coordinate arrangement is sometimes observed when Pt is coordinated to one or more alkene-type ligands, although four-coordinate $Pt^0$ complexes are also common; thus, it is not possible to verify the presence of $Pt^{2+}$ on the basis of these XAS data alone.[145–148] Appealing to the results of the X-ray photoelectron spectroscopy (XPS) from the original synthetic paper,[26] however, yields convincing evidence in favour of the presence of $Pt^{2+}$ species, as is discussed later in this section.

With regard to the structure of the nanoclusters, the solvent used in this reaction (DMF) is itself capable of coordinating to metal centres;[149] however, the amide nitrogen atom bears sterically demanding methyl groups which might make it a poor nucleophile for the Pt atom. However, as in any redox reaction, the reduction of the $Pt^{4+}$ precursor requires that some other species in the reaction medium must be oxidized. DMF contains an aldehyde functional group that could easily be oxidized to a carboxylic acid, thereby producing a molecule more capable of coordinating Pt as a bidentate ligand.[125,130] If such ligands are present in solution, they might also be able to serve as bridging ligands to form polynuclear Pt complexes, as has been demonstrated both directly and by analogy with Pd in the scientific literature;[150–155] even simple chloride ions ($Cl^-$) have been observed to act as bridging ligands between $Pt^{2+}$ centres in complexes.[156]

There are two types of $Pt^{2+}$ complexes reported to exhibit optical fluorescence: Pt atoms coordinated to ligands like polypyridine, and dinuclear complexes in which charge transfer between two Pt atoms is possible.[157,158] Based on the experimental results

discussed previously, it has been proposed that a di- or poly-nuclear Pt complex might be responsible for the fluorescence observed in these DMF-reduced samples. While no Pt–Pt peak could be conclusively found in the experimental data, it is possible that an indirect or weak, and therefore unusually long, bond could be present.

Long bonds (on the order of 3 Å or more) are sometimes observed between Au atoms in nanoparticles,[141] and bonds of similar lengths can be seen in previously reported di- and poly-nuclear Pt complexes.[151,155] Thus, it is not unreasonable to suppose that similar bonding could be responsible for the fluorescent behaviour observed in these Pt–DMF nanoclusters. This notion of small, inorganic clusters is also consistent with the mass spectrometry results reported by Kawasaki *et al.*,[26] which suggest that these nanoclusters primarily ranged in size from four to six Pt atoms. As a result, these nanoclusters are likely composed of $Pt^{2+}$ sub-units held together by bridging ligands and/or weak Pt–Pt bonding interactions.[155]

Further evidence in favour of $Pt^{2+}$ formation is also available. As mentioned previously, similar syntheses using DMF have also been performed to generate nanoclusters from metals such as Ag, Pt, and Au.[26,125,130] Notably, only those reactions using Ag showed conclusive evidence of metallic nanoparticle formation, and accomplishing this required the addition of a suitable surfactant to produce a stable colloidal suspension.[130]

Furthermore, the aforementioned Au and Pt nanoclusters were characterized using various techniques, including XPS. It was observed that the Pt and Au $4f^{7/2}$ peaks reported in the respective articles[26,125] indicated greater binding energies for the products than are typical for the elements in their metallic states, a discrepancy that the authors attributed to a “nanosize effect”. Although an increase in binding energy has been

observed in the case of *ca.* 1 nm nanomaterials, such shifts are not typically as large as those reported for the metal-DMF products.[159,160] It is also worth noting that these reported binding energies are very similar to those published for molecular $Pt^{2+}$ and $Au^{+}$ species in general,[161–168] and are in particular agreement with previously reported values for the respective metal ion complexes with DMF.[139] Likewise, if the observed white line intensities and *CN*s from the experimental results (described previously) were due to an average of $Pt^{0}$ and $Pt^{4+}$ species, distinct peaks corresponding to these oxidation states should be (but are not) observed in the corresponding XPS spectra.[169]

Following a number of literature searches for "fluorescent platinum nanoclusters," a few additional articles were found on the subject. One article, in particular, claimed to have successfully synthesized fluorescent Pt nanoclusters, but the species thus produced were stabilized by a type of dendrimer known to exhibit similar fluorescence behaviour upon becoming oxidized. As a result some uncertainty exists as to the origin of the fluorescent activity.[170] Nonetheless, the results of their analysis using mass spectrometry are in good agreement with those published by Kawasaki *et al.*;[26] unfortunately, though, no attempt was made to identify the oxidation state of the product.[170]

Finally, one study did provide convincing evidence of metallic Pt production (via XPS analysis), but the observed fluorescence for the samples was very poor in comparison with both Au nanoclusters prepared using the same method and the DMF-synthesized nanoclusters reported herein.[171] Overall, those publications which were actually relevant to the subject did not report evidence contrary to our proposed non-metallic nanocluster theory.

## 3.6 Conclusions

In summary, results have been presented detailing the local structure and oxidation states of a series of Pt nanoclusters prepared with various reaction durations. FT-EXAFS fitting has shown that the Pt–Pt bonding seen in metallic nanoclusters is lacking in these compounds, and that evolution of the local structure occurs primarily due to changes in the metal–ligand coordination environment. Analysis of XANES data and literature reviews have indicated that the oxidation state of Pt in these samples is neither $Pt^0$, as expected, nor a combination of $Pt^0$ and $Pt^{4+}$, but instead $Pt^{2+}$. Based on these findings, it is proposed that a non-metallic, likely multinuclear Pt cluster is responsible for the observed fluorescence behaviour. Although the evidence currently available is insufficient to elucidate the exact structure of the observed products, the utility of XAS characterization methods in determining the structure of Pt-based samples has been well demonstrated. While the anticipated metal nanoparticle structure was not observed, investigations performed on more complicated bimetallic nanoparticle samples provide an opportunity to more fully demonstrate the capabilities of this technique.

# Chapter 4 – Local Structure, Electronic Behavior and Surface Reactivity of CO-reduced Pt-$FeO_x$ Nanoparticles

Adapted with permission from Reference 168:
Duchesne, P.N.; Chen, G.; Zheng, N.; Zhang, P. "Local Structure, Electronic Behavior and Surface Reactivity of CO-reduced Platinum-Iron Oxide Nanoparticles" *J. Phys. Chem. C,* **2013**, *117* (49), 26324-26333.


## 4.1 Contributions

PND and GC (College of Chemistry and Chemical Engineering, Xiamen University) synthesized the Pt–$FeO_x$ nanoparticles and deposited them onto the carbon powder support. High-Resolution TEM (HRTEM) image acquisition and EDS peak integration were performed by GC and analyzed by PND. PND acquired and analyzed CV and ORR activity data, performed XAS measurements and data analysis, conducted *ab initio* calculations, and wrote the manuscript. PZ supervised PND and helped with manuscript revision. NZ (College of Chemistry and Chemical Engineering, Xiamen University) supervised GC and helped with manuscript revision.

## 4.2 Foreword

The study presented in Chapter 3 explored the significant potential of XAS techniques for investigating the structure of Pt-based nanomaterials. This sort of analysis is fairly straightforward for pure Pt materials, but becomes more difficult for multi-metallic nanoparticles. Additionally, the Pt nanoclusters studied previously did not have the metallic structure required for many catalytic processes. In order to address both of these issues, this chapter describes the characterization of a series of larger nanoparticles synthesized using Pt and Fe. Emphasis is placed on the use of a "clean" synthesis and

easy sample purification, XAS characterization at both Pt and Fe absorption edges, and an initial exploration of electrocatalytic activity in the ORR.

## 4.3 Introduction

Energy generation and storage are essential for the sustenance of technology in our modern societies. As a result, much interest is focused upon such topics of research, which include batteries, supercapacitors, fuel cells, and novel hybrids thereof.[34,173–177] While the status quo leans heavily toward the use of batteries, developing technologies such as PEMFCs continue to improve, having sufficiently high energy densities to be practical for motor vehicle applications.[175,178] A major limiting factor in the further development of high-performance fuel cells is the low efficiency of the ORR occurring at the cathode; this cathodic ORR reaction remains an active area of research, with evidence indicating that it can be alleviated by employing the appropriate electrocatalysts.[34]

Finely dispersed Pt metal (often supported on some form of carbon or metal oxide) is the premier catalyst employed in many chemical reactions, including the ORR in PEMFCs.[179–183] Unfortunately, the high cost and low abundance of Pt are prohibitive for many developing technologies. The most common approach is to employ high-surface-area nanoparticles, which can help compensate for these drawbacks by maximizing the available surface area per unit mass of Pt.[34] Further improvements may also be gleaned by incorporating less costly 3d metals into the catalyst in order to minimize the amount of Pt required without reducing its activity. Thus, syntheses of nanoparticles comprising binary and even ternary Pt alloys are currently being explored.

Nanoparticles of many elemental compositions can be created by incorporating other metals, a process which could be crucial in the development of efficient and

affordable catalysts for fuel cell applications.[184,185] It has been demonstrated that the formation of homogeneous 3d–5d metal alloys can even enhance the observed activity of Pt catalysts.[48,186,187] Correlation of this enhanced Pt catalytic activity with a number of measurable structural and electronic parameters has been previously attempted. Both structural features (decreased Pt–Pt bond lengths and formation of a Pt-rich surface "skin") and electronic effects (lowering of the Pt d-band position relative to the Fermi energy and reduced d-electron density at Pt) have been observed to correlate with high activity in Pt alloy catalysts.[188] However, causation is still a matter of some debate.

In addition to the elemental composition of the nanoparticles, the synthetic method used in their production can also be an important factor. Many different synthetic methods may be employed in order to obtain pure and bimetallic Pt and nanoparticles; however, recently developed methods employing protecting molecules and reducing agents that are both multifunctional and easily removed during subsequent purification (such as the method employed herein) allow for cleaner and more reproducible syntheses.[23,53,189–191] In light of these encouraging developments, the value of further advancement in this field is readily apparent. Unfortunately, advances are hindered by the inherent difficulty in characterizing the structure of such complex materials and will likely require the use of specialized techniques.

As active electrocatalysts, Pt-based materials are readily characterized using electrochemical methods, such as cyclic and linear sweep voltammetry using a three-electrode RDE cell.[192] HRTEM is useful for measuring the general structure of nanomaterials and can even be used to measure lattice spacing in crystalline samples, but is incapable of providing specific information regarding local atomic structure.[193] By comparison, XAS is able to provide more specific information regarding both electronic

properties and local atomic structure for a wide range of sample types.[194] XAS has also been previously used to provide accurate structural and electronic information for a variety of nanomaterials, including mono- and bimetallic nanoparticles,[159,195] and nanoclusters.[123,177]

The selectivity and sensitivity afforded by XAS are often simply not obtainable using more conventional methods, which could prove damaging to the sample materials.[74,196] Furthermore, the utility of XAS in characterizing bimetallic nanoparticle catalysts has already been well demonstrated using analogous metals such as Au and Pd.[197,198] Employing these X-ray techniques to study the structure–property relationships of the nanoparticle samples allows the features responsible for their enhanced activity to be understood. This information can then be used to develop more highly active nanoparticle catalysts.

Herein is reported the synthesis of a series of nearly monodisperse platinum–iron oxide (Pt–$FeO_x$) nanoparticles using a clean CO-reduction method; with the term "$FeO_x$" being used to encompass a range of possible oxidized Fe species, including oxides, hydroxides, and oxyhydroxides. Their local structure and electronic behavior were studied using XANES and EXAFS measurements of the Pt $L_3$- and Fe K-edges. The CO-reduction method allowed for the synthesis of high-quality nanoparticles (*i.e.*, near-monodisperse particle sizes and controlled compositions), enabling a reliable investigation of their structural and electronic properties. This structural and electronic information was then correlated with the surface reactivity of these nanoparticles in the ORR.

## 4.4 Experimental Methods

### 4.4.1 Materials

Iron(II) acetylacetonate ($Fe(acac)_2$, 99.95% trace metal basis) and *n*-butylamine (99.5%) were purchased from Sigma-Aldrich. Platinum(II) acetylacetonate ($Pt(acac)_2$, minimum 48.0% Pt), HiSPEC 3000 carbon-supported Pt catalyst (Pt/C, ≤ 500 ppm impurities), and Nafion® (5% w/w in water/1-propanol) were purchased from Alfa Aesar. Oleylamine (OAm, C18-content 80-90%) was purchased from Acros Organics. Vulcan XC-72 carbon powder was purchased from Cabot. All reagents and solvents were used as received, without further purification.

### 4.4.2 Synthesis of Pt–$FeO_x$ Nanoparticles

Nanoparticle samples with varying elemental compositions were synthesized according to a synthetic procedure previously employed by Chen *et al.*[189] In a typical synthesis, a 0.1 mM total concentration of metal ions was used. $Pt(acac)_2$ was first dissolved in 3 mL OAm and purged with carbon monoxide gas before being charged to a pressure of 1 atm. This mixture was heated from room temperature to 60 ˚C over a 10 min period in order to ensure complete dissolution. The temperature was then increased to 120 ˚C over a 10 min period in order to induce the nucleation of Pt seed nanoparticles and held constant for 30 min. A 2 mL solution of $Fe(acac)_2$ in OAm was quickly injected into the reaction vessel and the temperature raised to 200 ˚C over a 20 min period in order to incorporate Fe into the seed nanoparticles. After a further 30 min, the reaction vessel was removed from heat and allowed to gradually cool to room temperature. The product nanoparticles were purified and precipitated by adding 1 mL of hexanes and 5 mL of anhydrous ethanol (laboratory grade) to the reaction mixture and then centrifuging the

resulting suspension at 6,000 RPM for 2 min. After decanting the supernatant solution, the product nanoparticles were re-dispersed in hexanes/ethanol and purified twice more using the aforementioned procedure before finally being dispersed in 1 to 2 mL of hexanes.

This synthetic approach was described as "clean" relative to more common methods, as the reaction mixture is simplified considerably by the fact that both OAm and CO serving as surface-protecting ligands in addition to their respective roles as solvent and reducing agent. As a result, fewer by-products are present post-synthesis. Furthermore, the gaseous nature of CO and its oxidation product, $CO_2$, under standard conditions renders them easily removed from the final reaction mixture. Similarly, excess OAm can be simply decanted following precipitation and centrifugation of the nanoparticle product. By contrast, the dissolved protecting ligands used in other methods tend to precipitate during purification and can prove troublesome to separate. Experiments have also shown that the scale of the reaction can be doubled (to yield *ca.* 40 mg of product) without negatively affecting nanoparticle yield or morphology.

### 4.4.3 Deposition onto XC-72 Carbon Powder

After being purified, nanoparticle suspensions were precipitated by adding three to four volume equivalents of ethanol and then centrifuged at 6,000 RPM for 2 min. After decanting the supernatant, sufficient carbon powder was added to achieve the desired catalyst loading (*i.e.*, 30 wt% Pt) and the carbon/nanoparticle mixture was dispersed in *n*-butylamine at an approximate concentration of 1 $mg \cdot mL^{-1}$. The resulting suspension was simultaneously mixed and sonicated for several minutes in a 50 mL round-bottom flask. This suspension was purged with nitrogen and sealed in order to minimize oxygen

exposure, then allowed to stir for 48 h. Finally, centrifugation was employed to isolate the carbon-supported nanoparticle product; after being thrice washed with ethanol and centrifuged, the product was dried under flowing nitrogen and stored in a Parafilm®-sealed sample vial. This ligand-exchange and washing process also served to help remove OAm ligand molecules from the nanoparticle surfaces, thereby increasing the number of binding sites available for electrocatalysis.

### 4.4.4 Electron Microscopy

Samples used for HRTEM and EDS analyses were prepared using identical methods. A small portion of catalyst material was suspended in ethanol and drop-cast onto a Formvar-coated copper HRTEM grid. All measurements were performed by Guangxu Chen at Xiamen University in Fujian, China. The instrument was operated in bright field mode on a Tecnai F-30 high-resolution transmission electron microscope operated at 300 kV. Nanoparticle diameters were measured using MacBiophotonics ImageJ image processing software in conjunction with the respective HRTEM micrographs of each sample.[199] Relative elemental compositions were calculated from the integrated peak areas corresponding to Pt and Fe.

### 4.4.5 Cyclic Voltammetry

Prior to electrocatalytic activity testing, Pt–$FeO_x$ and Pt/C samples were drop-cast onto a mirror-polished glassy carbon electrode. Approximately 1 mg of the supported catalyst material was dispersed in a 40 vol% solution of isopropanol in de-ionized water and mixed with 0.04 mL Nafion® solution to form a catalyst ink. The Pt concentration of this ink was subsequently determined using inductively coupled plasma atomic absorption spectroscopy. Sonication for *ca.* 1 min was sufficient to thoroughly disperse the catalyst

material, 20 μL of which were deposited onto a glassy carbon electrode in 5 μL aliquots and allowed to dry under a gentle flow of air while rotating slowly (*ca.* 5 Hz) to produce a uniform film; this film was then stabilized by applying an additional 1 μL Nafion® solution and allowing the surface to dry completely before immersing it in the electrolyte solution. Sample loadings for RDE voltammetry experiments were confirmed using inductively coupled plasma optical emission spectroscopy. A commercial, carbon-supported Pt catalyst (HiSPEC 3000, 20 wt% Pt loading), hereafter referred to as Pt/C, was also used as a reference material for structural characterization and electrocatalytic studies.

Electrochemical measurements were obtained using a RDE apparatus from Pine Instrument Company, in the laboratory of Prof. Jeff Dahn at Dalhousie U/niversity. A rotation rate of 1,600 RPM was used for all experiments. A 0.1 M perchloric acid solution was used as the electrolyte in all measurements, and all glassware was boiled in deionized water prior to use and handled carefully to prevent contamination. A three-electrode system was employed, with a mirror-polished glassy carbon RDE working electrode, a simple Pt wire counter electrode, and a Koslow mercury/mercurous sulfate reference electrode. Prior to electrochemical testing, samples were cycled repeatedly (30 to 50 times) between 0.03 or 0.05 $mV_{RHE}$) and 1.2 $V_{RHE}$ in $Ar_{(g)}$-saturated perchloric acid solution until voltammograms became reproducible. ORR voltammograms were recorded while the electrolyte solution was saturated with or $O_{2(g)}$, respectively.

### 4.4.6 X-ray Absorption Spectroscopy

XAS measurements were performed using the Sector 20-BM beamline of the Advanced Photon Source at Argonne National Laboratory in Argonne, IL. Samples were

measured either as pure powders (given a sufficient volume of material) or dispersed in a solid matrix of boron nitride. A cryostat was used to maintain a sample temperature of 50 ± 1 K during measurements; these low-temperature conditions allowed for better-quality XAS data to be obtained via suppression of thermal vibrations, which significantly affect oscillation intensity and can result in lowered signal-to-noise ratios. A double-crystal Si(111) mirror monochromator was used for wavelength selection and, in combination with a Rh-coated Si focusing mirror, detuned to 80 % in order to reject higher harmonics; sample data were collected using either a gas ionization chamber or a 12-element Ge fluorescence detector, depending on the sample concentration. Data workup and FT-EXAFS fitting were performed using the IFEFFIT software suite.[77]

Information regarding the fitting of Pt $L_3$-edge EXAFS spectra (*k*-range used for Fourier-transformation, region of interest (ROI) used for peak fitting, *etc.*) is summarized in Table 4.1. Data ranges were selected in order to include as much of each spectrum as possible in the fits while excluding excessively noisy regions of the data, and thus differ slightly between samples.

**Table 4.1.** Conditions used for the fitting of the Pt $L_3$-edge FT-EXAFS spectra. Reproduced with permission from Reference 168.

| Sample | *k*-Weight | *k*-Range / $Å^{-1}$ | ROI / Å | Fitted Paths |
|---|---|---|---|---|
| $Pt_{90}Fe_{10}$ | 2 | 2.5 to 13.0 | 1.9 to 3.1 | Pt-Fe \| Pt-Pt |
| $Pt_{70}Fe_{30}$ | 2 | 2.5 to 11.0 | 1.6 to 3.1 | Pt-Fe \| Pt-Pt |
| $Pt_{50}Fe_{50}$ | 2 | 2.5 to 10.0 | 1.6 to 3.2 | Pt-Fe \| Pt-Pt |
| Pt-C | 2 | 2.5 to 13.0 | 1.5 to 3.1 | Pt-O \| Pt-Pt |

### 4.4.7 *Ab Initio* Calculations

*Ab initio* calculations of electronic properties were performed using FEFF8 software.[78] A modified version of FEFF8.4 was employed, in which the initial electron configuration for Fe was modified from $[Ar]3s^2 3d^6 4s^1 4p^1$ to a more typical value of $[Ar]3s^2 3d^8$. This change was made in order to prevent anomalous charge transfer from Pt to Fe due to the unusual default orbital occupations. The optimized structural models were based upon those from a previously published paper by Wang *et al.*[200]

## 4.5 Results and Discussion

### 4.5.1 EDS and HRTEM Characterization

Representative EDS spectra for purified Pt–$FeO_x$ nanoparticles were obtained by Guangxu Chen and are shown in Figure 4.1a. Measurements were taken at multiple sites on each sample grid and averaged in order to more accurately determine relative elemental compositions. On the basis of Pt and Fe peak areas, final atomic compositions of $Pt_{90}Fe_{10}$, $Pt_{70}Fe_{30}$, and $Pt_{50}Fe_{50}$ were obtained, thereby confirming the incorporation of Fe into the as-synthesized nanoparticles. Relative uncertainties in these composition measurements were approximately 10 atom% for all samples; however, these compositions differed markedly from the molar ratios of Pt and Fe used in preparing the nanoparticles (3:1, 1:1, and 1:2, respectively). This phenomenon could be explained by either sampling error or incomplete incorporation of Fe into the nanoparticle product. It is well-known that bulk analysis using transmission electron microscopes is limited by the mean free path of the electrons within the sample material. The applied acceleration voltage (300 kV), however, should easily permit electron transmission through these

nanoscale Pt–$FeO_x$ materials (as per the Kanaya-Okayama depth penetration formula);[201] thus, effects from sampling error should be negligible. Subsequent UV-vis spectroscopy analysis revealed that the pale yellow supernatant recovered following purification of the nanoparticles contained measurable amounts of $Fe^{3+}$; this provided strong evidence for the incomplete incorporation of the Fe precursor molecules into the final product, thereby explaining the relatively low measured Fe content.

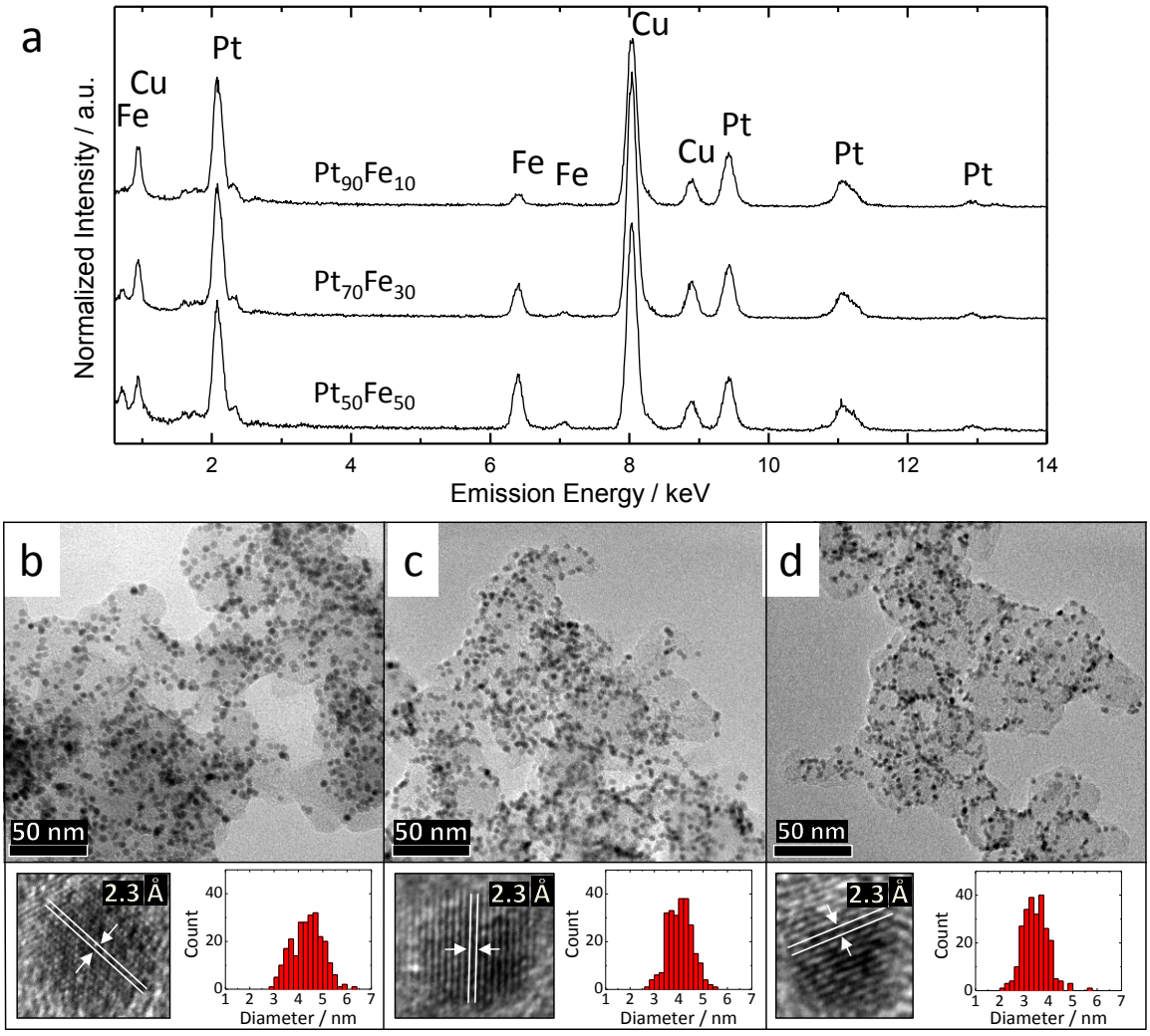


**Figure 4.1.** (a) EDS spectra of $Pt_{90}Fe_{10}$, $Pt_{70}Fe_{30}$, and $Pt_{50}Fe_{50}$ nanocatalysts normalized to the Pt $L_\alpha$ peak intensity (*ca.* 9.5 keV); representative HRTEM images and (lower right) corresponding particle size distributions (N = 250) of (b) $Pt_{90}Fe_{10}$, (c) $Pt_{70}Fe_{30}$, and (d) $Pt_{50}Fe_{50}$ carbon-supported nanoparticles are also shown. White lines and arrows in the images of individual nanoparticles indicate lattice spacings observed in the HRTEM image. Adapted with permission from Reference 168.

Representative HRTEM images depicting the carbon-supported Pt–$FeO_x$ nanocatalysts are shown in Figure 4.1b-d. Nanoparticles appear in high contrast, while the significantly larger XC-72 carbon support particles (*ca.* 40 nm in diameter) are less distinct. Also shown for each sample are high-magnification micrographs (lower left) and histograms (lower right), illustrating the respective lattice fringes and size distributions for each sample. These images indicate that the carbon-supported nanoparticles were well-dispersed with little to no aggregation, thereby maximizing their available surface areas. Mean Pt–$FeO_x$ nanoparticle diameters of 4.4 ± 0.6 nm, 4.0 ± 0.5 nm, and 3.5 ± 0.5 nm were obtained for $Pt_{90}Fe_{10}$, $Pt_{70}Fe_{30}$, and $Pt_{50}Fe_{50}$, respectively. ANOVA testing revealed that these values were significantly different at the 99.9 % confidence level and indicated a trend toward decreasing particle size with increasing Fe content.

The observed trend in particle size is readily explained by the fact that the total concentration of metal ions used in each synthesis was held constant; as a result, the concentration of Pt ions is lower during the growth phase for samples with greater Fe content, resulting in decreased particle sizes. By comparison, the mean nanoparticle diameter for Pt/C from TEM is smaller than those of the Pt–$FeO_x$ samples, at just 2.8 ± 0.7 nm.[202] The high uniformity of elemental compositions and size distributions for these nanoparticles was essential in accurately determining their structural properties. Large variations in size and/or composition would make attempting to correlate these qualities with other observed properties (*e.g.*, electrocatalytic activity) unfeasible due to the differences between individual particles.

Parallel lines in each high-magnification image (see Figure 4.1b-d) illustrate lattice fringes corresponding to Pt(111) planes in the featured particle. Mean lattice spacings of 2.30 ± 0.05, 2.31 ± 0.03, and 2.28 ± 0.02 Å were observed for $Pt_{90}Fe_{10}$,

$Pt_{70}Fe_{30}$, and $Pt_{50}Fe_{50}$, respectively. These values were determined from the lattice fringes of multiple particles in each sample and are consistent with values for face-centred cubic (FCC) Pt. Interestingly, even in samples containing nearly equal amounts of Pt and Fe, lattice fringes corresponding to either metallic Fe or iron oxide phases were not clearly visible. This could be explained by the fact that amorphous materials do not register as clearly in TEM images, as evidenced by the use of amorphous carbon films on many TEM grids.[203] However, EXAFS analysis (*vide infra*) provides evidence of direct Pt–Fe bonding interactions, suggesting that even if discrete iron $FeO_x$ nanoparticles were also formed during synthesis, the Pt-Fe nanoparticles likely comprise a metallic Pt core and an amorphous $FeO_x$ surface layer. Unfortunately, nanoparticles such as these often cannot be reliably characterized using conventional techniques, such as X-ray diffraction.[204] Therefore, in order to verify our hypothesis, structural analysis was performed using XANES and EXAFS, which are well-suited to probing the local structure of both nanocrystalline and amorphous materials from an element-specific perspective.

### 4.5.2 Pt $L_3$-Edge and Fe K-Edge XANES Analysis

XANES spectra corresponding to both Pt–$FeO_x$ nanoparticles and relevant reference samples are presented in Figure 4.2. It should be noted that these data reflect the as-synthesized nanoparticle materials, and that the structure of these samples may change *in situ* during catalytic testing. In the case of the Pt $L_3$-edge, the white line represents a 2p to 5d electronic transition; thus, its intensity is reflective of the occupation of the 5d orbitals; lower occupation results in greater white line intensity and vice versa.

The shape of the near-edge region is sensitive to both the phase and oxidation state of the element of interest; thus, the strong similarities in fine structure between the

Pt $L_3$-edge XANES spectra of the Pt–$FeO_x$ nanoparticles and the Pt foil (shown in Figure 4.2a) illustrate the metallic FCC character of Pt in these samples. The Pt–$FeO_x$ nanoparticles possessed d-electron densities lower than that of Pt foil but greater than that of Pt/C, indicating a degree of oxidation intermediate between the two references. However, no correlations were observed between these white line intensities and other structural or electronic properties. This absence of correlations was attributed to the combination of factors contributing to the d-electron density of Pt, including particle size, surface oxidation, and Fe content. In order to gain another perspective on this problem, XANES measurements were also performed on the Pt–$FeO_x$ samples at the Fe K-edge.

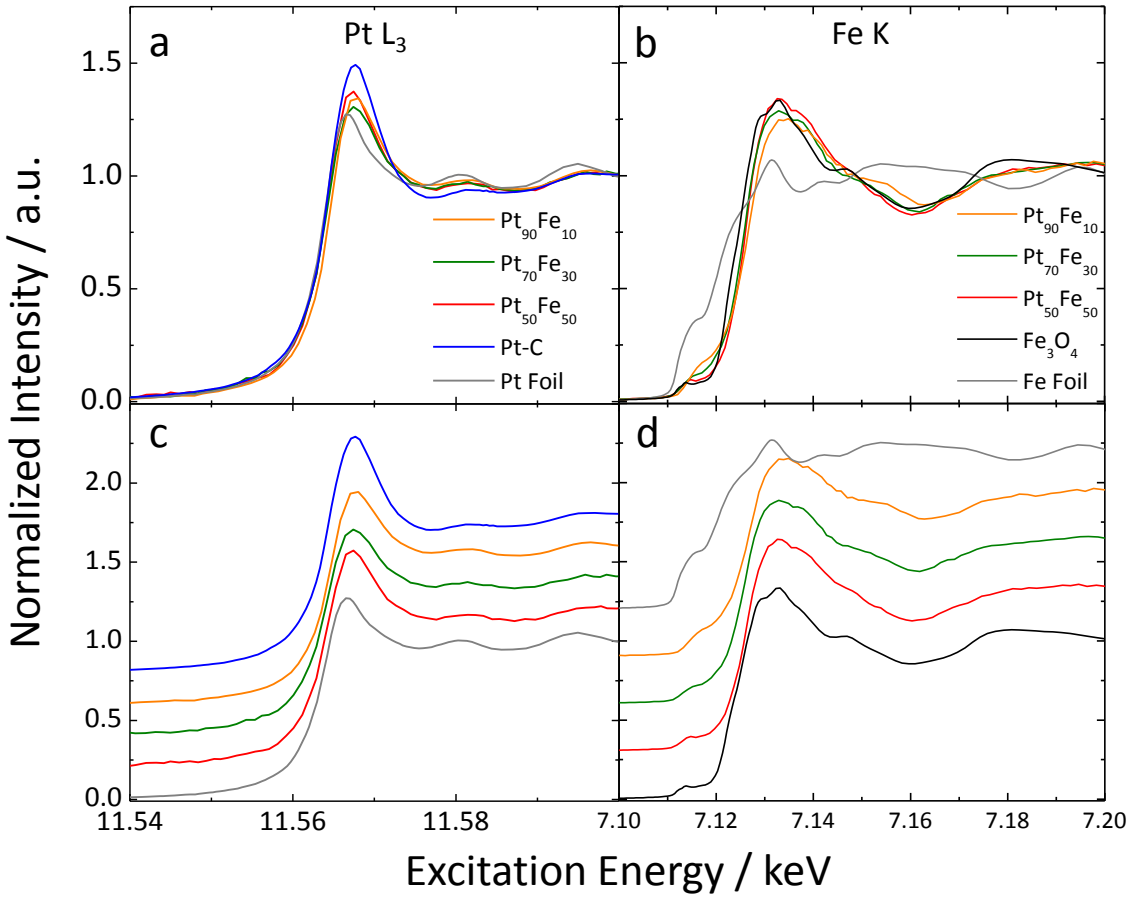


**Figure 4.2.** Overlapped (a) Pt $L_3$- and (b) Fe K-edge XANES spectra of carbon-supported Pt–$FeO_x$ nanoparticles and some relevant reference compounds. Stacked (c) Pt and (d) Fe spectra are included in order to better illustrate similarities in near-edge features. Adapted with permission from Reference 168.

Fe K-edge XANES spectra of the Pt–$FeO_x$ electrocatalysts are shown in Figure 4.2b. K-edge white lines represent an s-to-p electronic transition, and thus, their peak intensities do not correlate with d-electron density as do those of $L_3$-edges. Still, the overall shape of the XANES region can be used as a spectral fingerprint to provide insight into the observed phase. Such analyses revealed that Fe species within the sample more closely resembled the $Fe_3O_4$ reference than Fe foil, indicating that Fe was present primarily in an oxidized state. Unfortunately, due to significant structural disorder of the $FeO_x$ phase and strong similarities between the XANES spectra of various Fe oxides,[205] its exact phase could not be determined.

The relative amount of low-valent Fe (*i.e.*, $Fe^0$) in each sample does, however, still significantly influence overall peak shape. A greater abundance of low-valent Fe is reflected in both the increased intensity of the pre-edge feature at just before 7.12 keV and the reduced intensity of the most intense peak near 7.13 keV. Close inspection of the trend for these two features in Figure 4.2b reveals that the relative amount of low-valent Fe in the nanoparticles increases in the order $Pt_{50}Fe_{50} < Pt_{70}Fe_{30} < Pt_{90}Fe_{10}$. On the basis of this result, it seems likely that the low-valent Fe exists at the interface between Pt and $FeO_x$, being stabilized by the interaction with the Pt surface. In contrast, the high-valent Fe likely exists farther from the Pt surfaces, or as discrete $FeO_x$ nanoparticles. When the atomic Fe:Pt ratio is increased, a thicker layer of $FeO_x$ would be also expected, resulting in a relative decrease in the amount of low-valent Fe. While this analysis afforded important insight into the nanoparticles' structure, more quantitative information regarding the local structure was also obtained via EXAFS data analysis and fitting.

### 4.5.3 EXAFS Analysis and Fitting

Qualitative information regarding the structure of Pt in the Pt–$FeO_x$ samples can be obtained from the Pt $L_3$-edge EXAFS spectra presented in Figure 4.3. By comparing Pt/C and Pt–$FeO_x$ nanoparticles to the Pt foil reference, it can be seen that all of these samples are very similar to one another and exhibit spectra characteristic of FCC lattices. The increased noise in spectra obtained from Pt–$FeO_x$ nanoparticles containing a larger proportion of Fe (*i.e.*, $Pt_{70}Fe_{30}$ and $Pt_{50}Fe_{50}$) is likely the result of increased background absorption by Fe species. Nevertheless, visible oscillations are observed up to and beyond 12 $Å^{-1}$, providing ample data for the fitting of Fourier-transformed spectra.

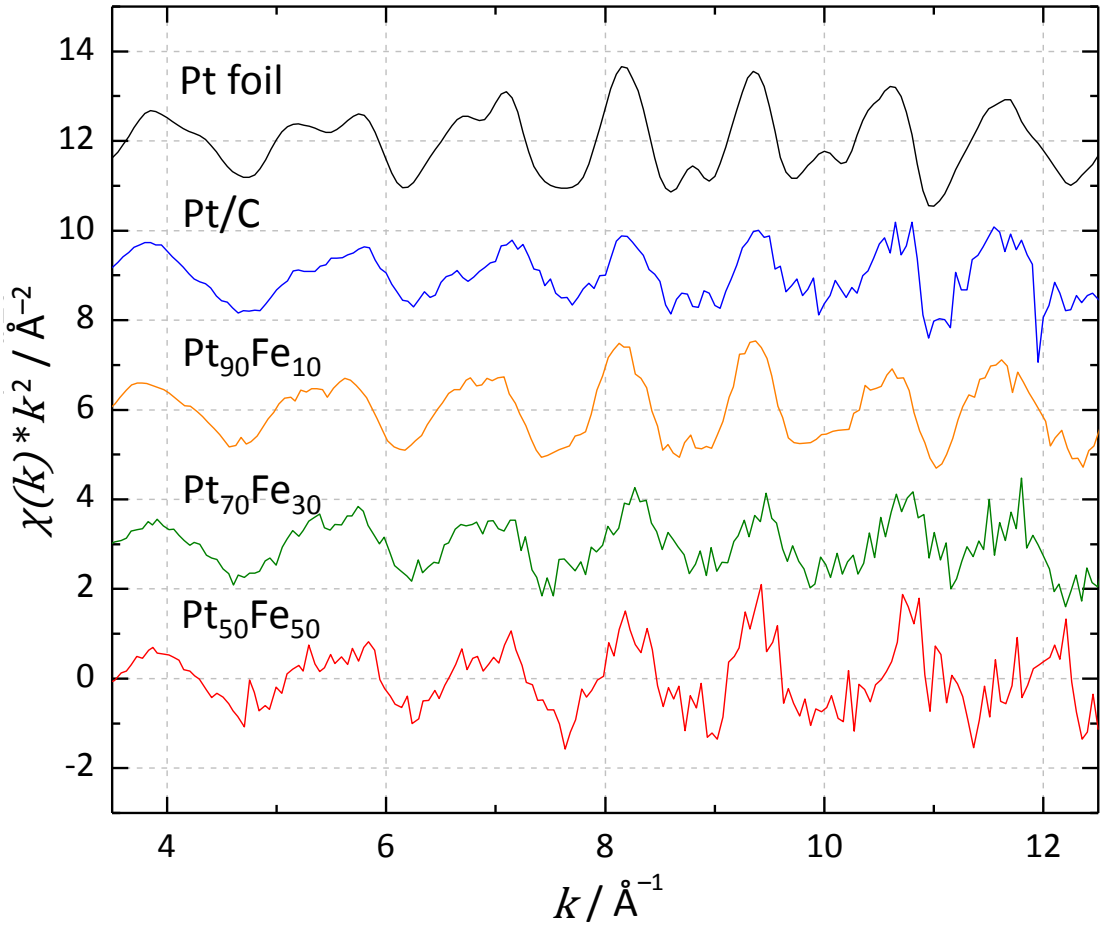


**Figure 4.3.** Pt $L_3$-edge EXAFS spectra ($k^2$-weighted) for Pt–$FeO_x$ nanoparticles and reference materials. Reproduced with permission from Reference 168.

Fitted, Pt $L_3$-edge FT-EXAFS spectra for Pt–$FeO_x$ nanoparticles and a commercial Pt/C reference are shown in Figure 4.4; structural parameter values obtained from these fits are presented in Table 4.2. A *k*-weight of 2 was selected for fitting these data in order to give more emphasis to the low-intensity Pt−Fe scattering path, which would be harder to resolve from the Pt−Pt path using the typical *k*-weight of 3, due to the fact that higher *k*-weights preferentially emphasize contributions from heavier elements. The observed similarities between Pt−Fe *CN*s indicated similar degrees of Pt–Fe bonding from the perspective of Pt in all Pt–$FeO_x$ samples (*i.e.*, *CN*s of 1 to 2). These values were much lower than those expected for intermetallic $Pt_3Fe$ or PtFe nanoparticles, suggesting that much of the Fe present in the samples was not intermixed directly with Pt, but instead existed as a $FeO_x$ shell atop the observed Pt core.

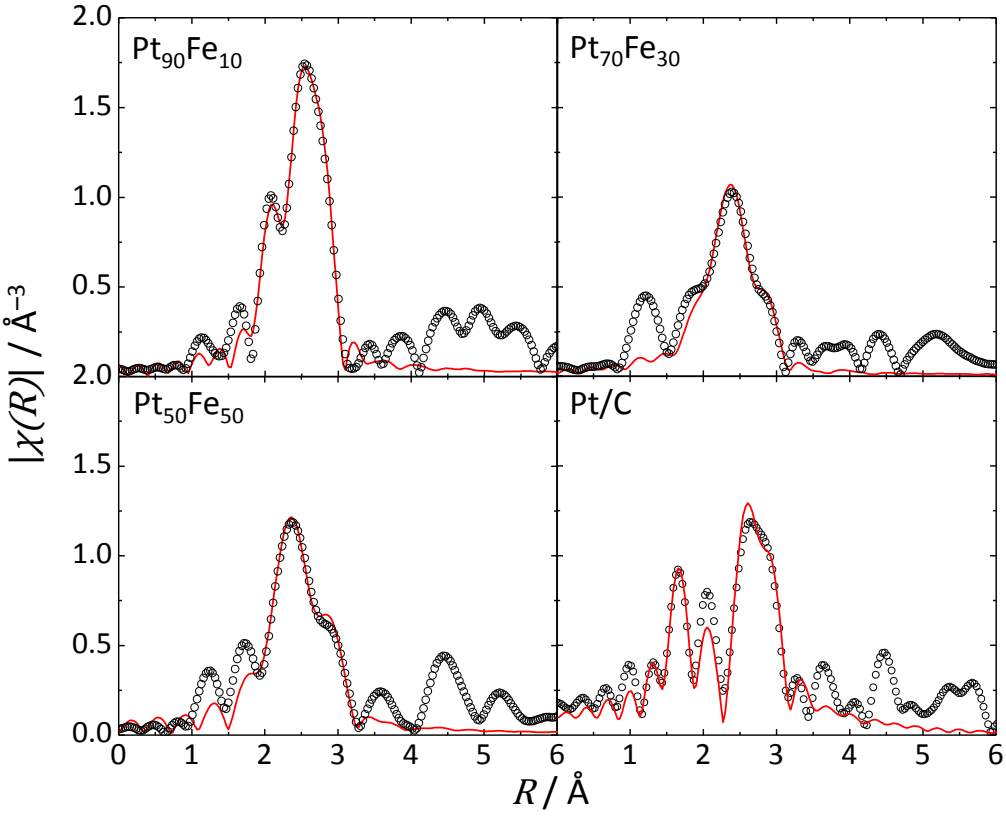


**Figure 4.4.** Experimental and fitted Pt $L_3$-edge FT-EXAFS spectra for Pt–$FeO_x$ and Pt/C catalyst samples. Adapted with permission from Reference 168.

**Table 4.2**. Structural parameter values obtained via fitting of Pt $L_3$-edge FT-EXAFS spectra. Uncertainties are indicated in parentheses (treated as one standard deviation). Adapted with permission from Reference 168.

| Sample | Path | *CN* / a.u. | *R* / Å | $\sigma^2$ / $10^{-3}$ Å$^2$ | $\Delta E_0$ / eV |
|---|---|---|---|---|---|
| $Pt_{90}Fe_{10}$ | Pt–Fe | 1.0(3) | 2.67(2) | 3(1) | 1(2) |
| | Pt–Pt | 8(1) | 2.775(5) | | |
| $Pt_{70}Fe_{30}$ | Pt–Fe | 1.7(7) | 2.70(3) | 6(2) | 2(2) |
| | Pt–Pt | 7(2) | 2.72(1) | | |
| $Pt_{50}Fe_{50}$ | Pt–Fe | 1(1) | 2.72(9) | 3(3) | 3(4) |
| | Pt–Pt | 7(3) | 2.72(3) | | |
| Pt/C | Pt–O | 1.9(3) | 2.04(2) | 2(2) | 10(1) |
| | Pt–Pt | 6(2) | 2.78(1) | | |

Lower metallic *CN*s are typically observed in metal nanoparticles of sufficiently small size, due to their increased specific surface areas, and indicate a large proportion of atoms at surface sites. Thus, the low Pt−Fe *CN* may also be indicative of the presence of Fe atoms at or near the nanoparticle surface, a finding that is also consistent with the results of Fe K-edge XANES analysis. It was further observed that the total Pt–M (M = Pt or Fe) *CN*s for the Pt–$FeO_x$ samples were lower than expected for nanoparticle of these sizes (being all significantly larger than those of Pt/C). Because both the reported bond lengths and HRTEM lattice fringes for Pt confirm that the FCC structure is retained in these samples, this discrepancy was attributed to vacancies and other defects at the Pt core formed during synthesis.

In addition to the observed trends in *CN* values, the experimental data provided useful information in terms of bond lengths. Significant differences in Pt–Pt bond lengths were identified, with the more Fe-rich samples ($Pt_{70}Fe_{30}$ and $Pt_{50}Fe_{50}$) possessing significantly shorter bonds than those containing little or no Fe ($Pt_{90}Fe_{10}$ and Pt/C). It is possible that this observation reflects a greater amount of intermetallic interaction near

the Pt surface of the Fe-rich nanoparticles, which has been observed to result in similarly decreased Pt–Pt bond lengths.[206,207] The increased likelihood of incorporation of Fe into the Pt core can be explained by the relatively larger number of Fe ions present in the reaction mixture for these nanoparticles, which increases the probability of significant Fe diffusion into the metallic Pt lattice under the reductive synthetic conditions. This trend is likely not visible from the Fe XANES spectra is that, as is also shown by Fe K-edge EXAFS spectra, $FeO_x$ is much more abundant than metallic Fe in these samples.

It is readily apparent from the similarities between the corresponding Fe K-edge EXAFS spectra presented in Figure 4.5a that Fe present in the Pt–$FeO_x$ nanoparticles exists primarily in an oxidized state. The high degree of noise observed in these spectra can be attributed to two predominant factors, the presence of significant amounts of Pt in each sample and the lack of long-range order in the $FeO_x$ phase. The large absorption cross section of Pt can result in considerable attenuation of the incident X-ray beam, thereby interfering with the signal obtained from Fe species. Furthermore, samples lacking long-range order (such as these Pt–$FeO_x$ nanoparticles) tend to exhibit reduced amplitudes of oscillation at higher k-values. Additional support for the latter of these causes is provided by analysis of the corresponding FT-EXAFS spectra. Although quantitative fitting of the Fe K-edge FT-EXAFS was precluded by the noisiness of the data, qualitative comparisons of peak positions (shown in Figure 4.5b) revealed apparent similarities between all Pt–$FeO_x$ nanoparticles and the $Fe_3O_4$ reference. However, an apparent shift to higher *R*-values and significant reduction in the Fe–Fe peak intensity (*ca.* 2.8 Å, corresponding to the iron oxide phase) for the Pt–$FeO_x$ nanoparticles indicated a lack of significant long-range order relative to bulk $Fe_3O_4$.

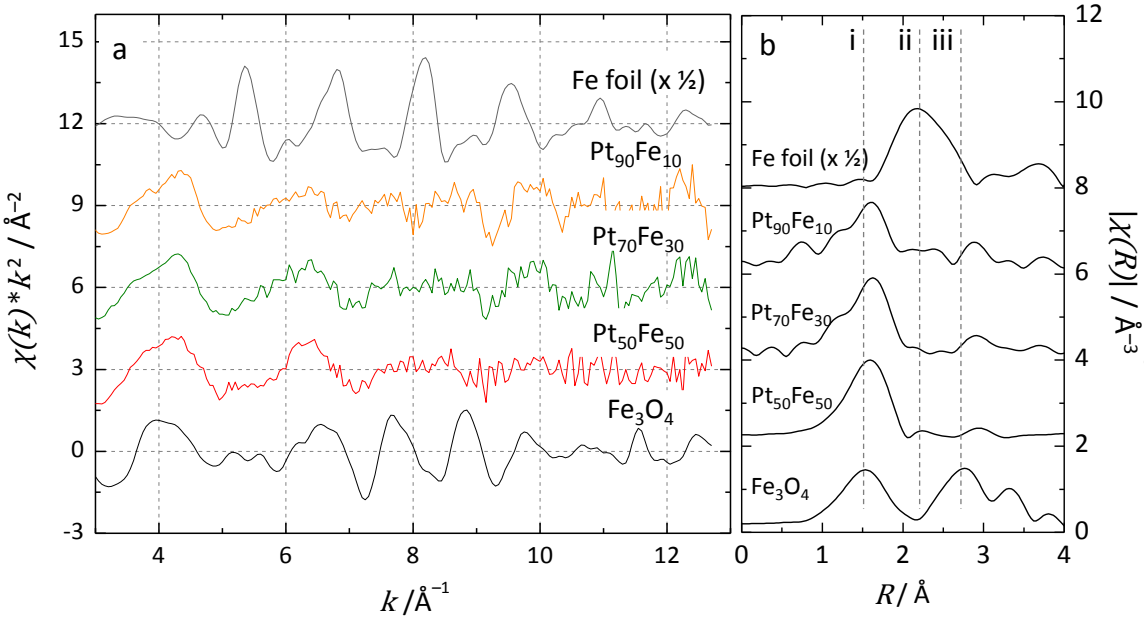


**Figure 4.5.** Fe K-edge EXAFS presented as (a) EXAFS and (b) FT-EXAFS from Pt–$FeO_x$ nanoparticles and reference materials. Note that the intensities of both the EXAFS and FT-EXAFS spectra for the Fe foil reference have been reduced by half to allow for easier graphical comparison. Peaks indicated by dashed lines correspond to (i) Fe–O bonding, (ii) Fe–Fe metallic bonding, and (iii) Fe–Fe bonding in iron oxides. Adapted with permission from Reference 168.

The observed shift and decrease in peak intensity are to be expected from more amorphous materials, which have a broader distribution of bond lengths due to their decreased order; this further helps to corroborate the absence of measurable Fe oxide lattice fringes in the measured HRTEM images. The proportion of metallic Fe–Fe bonding in each sample was estimated from the intensity of the Fe–Fe scattering peak at *ca.* 2.2 Å. From a comparison of these features, it was concluded that, consistent with the Fe XANES results, the relative amount of low-valent Fe in each sample increased in the order $Pt_{50}Fe_{50} < Pt_{70}Fe_{30} < Pt_{90}Fe_{10}$. This indicates that a greater proportion of the Fe precursor is reduced when less is initially added and that total reduction may be possible when only very small amounts of Fe are added to the reaction mixture. For these samples, particularly those with greater Fe content, $FeO_x$ predominated over metallic Fe. Due to

the fact that Pt seed particle nucleation occurred prior to addition of the Fe precursor during synthesis, finding a Pt–Fe core-shell structure was to be expected, and evidence of the Pt–$FeO_x$ structure was provided by many of the employed characterization techniques. In order to better understand the electronic effects of surface $FeO_x$ on the Pt core, *ab initio* calculations were employed to investigate interactions at the Pt–$FeO_x$ interface.

### 4.5.4 Simulation of Electronic Structure

As illustrated in Figure 4.6, *ab initio* electronic calculations were used to determine charge transfer, electron counts, and d-electron density of states (d-DOS) information for atoms located at the (111) surfaces of three model structures: pure metallic Pt, an intermetallic PtFe alloy, and metallic Pt with a partial surface layer of FeO (denoted Pt@FeO). As expected given their respective electronegativities, both the overall charge transfer and d-electron counts of Fe revealed significant electron donation from Fe to Pt in PtFe and Pt@FeO. Figure 4.6a shows that although considerable charge density was lost by surface Fe sites in the Pt@FeO system, nearly negligible charge density gain was experienced by each individual Pt atom. This effect can be simply attributed to the relatively large number of Pt atoms present in the model (*ca.* 18 atoms Pt per atom of Fe), as supported by the fact that more significant charge gain per Pt atom is observed for PtFe, in which more similar numbers of Pt and Fe atoms is present.

Although this 18:1 ratio is higher than expected for any of the actual Pt–$FeO_x$ samples, it allows the model to include a several-layer depth of Pt atoms, which more accurately represents the Pt nanoparticle core. The effects of PtFe interactions and surface FeO on d-electron counts are presented in Figure 4.6c. As a result of the aforementioned charge transfer, Fe d-electron counts in the Pt−Fe model were reduced relative to Fe

metal for both systems, with a greater decrease observed for Pt@FeO due to the presence of many electronegative O atoms. The effects on the Pt d-electron counts were less dramatic, and the only appreciable change was an increase for the PtFe model. Thus, it can be expected that the presence of interfacial Fe species will contribute little to the d-electron density of Pt in the Pt–$FeO_x$ nanoparticles.

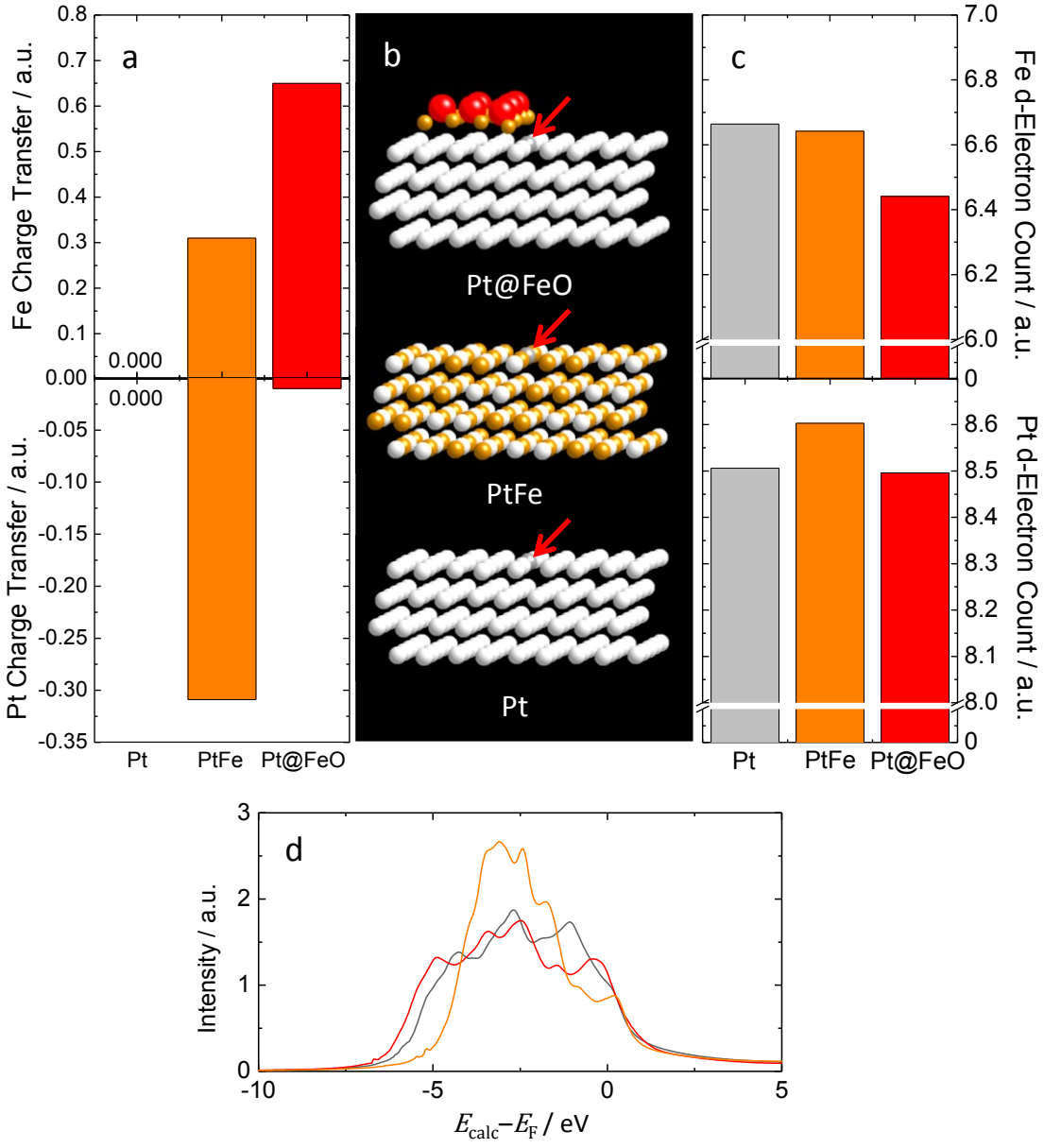


**Figure 4.6.** *Ab initio* FEFF8 simulation results, including (a) calculated interatomic charge transfer, (b) structural models used for simulations, (c) atomic d-electron counts, and (d) d-DOS spectra for edge-site Pt and surface-site Fe atoms in Pt (gray), PtFe (orange), and Pt@FeO (red). Adapted with permission from Reference 168.

It has been observed that Pt valence d-band properties correlate with the electrocatalytic behavior of Pt-based catalysts.[47] *Ab initio* d-DOS simulations, shown in Figure 4.6d, were performed in order to study the effects of surface Fe oxide on the Pt d-band in Pt–$FeO_x$ nanoparticles. These simulations revealed a slight overall broadening of the Pt d-band for Pt@FeO, as opposed to the significant narrowing observed for PtFe. Center positions of the d-bands relative to the Fermi energy were determined for each sample by integrating over the entire d-DOS region, yielding values of −2.24, −2.36, and −2.56 eV for Pt, PtFe, and Pt@FeO, respectively. The lowered d-band positions of both PtFe and Pt@FeO relative to Pt are in agreement with the experimentally determined d-band shifts of some highly active intermetallic PtFe catalysts[177,188] and reveal that the surface oxide structure is also capable of significantly influencing the electronic structure of Pt sites.

### 4.5.5 Testing Electrocatalytic Activity

In order to evaluate the relationship between the structural and electronic properties of Pt–$FeO_x$ nanoparticles and their surface reactivity, cyclic and linear sweep voltammetry measurements were performed. The reference electrode was calibrated before each session of CV measurements. Cyclic voltammograms for the Pt–$FeO_x$ and Pt/C samples (presented in Figure 4.7a) were normalized using their experimentally determined ECSAs for closer comparison. Several features of interest were observed, including H-desorption and Pt surface oxidation regions (positive peaks at 0.0 to 0.4 $V_{RHE}$ and at 0.7 to 1.2 $V_{RHE}$, respectively).

The peak areas in the H-desorption region correspond to the amount of charge passed in order to desorb surface-bound H atoms and were used to determine the ECSA

of each sample in accordance with standard procedures.[208] It was observed that all three Pt–$FeO_x$ samples possessed very similar specific ECSAs (*ca.* 40 $cm^2$ $mg^{-1}$ Pt), while that of the Pt/C reference was approximately twice as large (*ca.* 80 $cm^2$ $mg^{-1}$ Pt). In conjunction with results from EDS and HRTEM analyses, this observation of very similar specific ECSAs for all Pt–$FeO_x$ samples was found to further support the proposed Pt core/$FeO_x$ shell structure.

By assuming that the Pt–$FeO_x$ nanoparticles were spherical, that the diameters measured using HRTEM reflected only the size of the Pt core, and that the oxide layer is made up of $Fe_2O_3$, the compositions of each sample should exhibit uniform surface $FeO_x$ layers of 0.25, 0.60, and 0.93 nm in thickness for $Pt_{90}Fe_{10}$, $Pt_{70}Fe_{30}$, and $Pt_{50}Fe_{50}$, respectively. The presence of characteristic Pt features in the cyclic voltammograms, however, demonstrates that Pt is not totally obstructed by the $FeO_x$ surface layer and that an island-like structure of $FeO_x$ on Pt may be more probable.

While smaller nanoparticle diameters should exhibit larger specific ECSAs, the larger amount of $FeO_x$ present in these samples could result in blocking of surface sites, thereby counteracting the effects of particle size. The shapes of peaks in the H-desorption region also provide information regarding the presence of different Pt crystallographic facets, which could not be reliably assumed from HRTEM measurements obtained prior to electrochemical treatment and testing. Based upon the absence of H-desorption peaks centered between 0.3 and 0.4 $V_{RHE}$ (corresponding to Pt(100) surfaces[47]) and the predominance of peaks centered in the range of 0.0 to 0.3 $V_{RHE}$ (corresponding to Pt(110) and Pt(111) surfaces[47]) for the cyclic voltammograms of both the Pt–$FeO_x$ nanocatalysts and the Pt/C reference, it was proposed that the majority of surface Pt sites existed at the more highly active Pt(111) and Pt(110) surfaces, with minimal contributions from

Pt(100).[209] This distribution of surface facets is most likely due to the (previously discussed) preferred formation of certain crystalline facets at nanoparticle surfaces, as governed by the ligands employed in their synthesis.

The onset of the Pt surface oxidation region is typically associated with the adsorption of hydroxyl groups to form a Pt–$OH_{ads}$ layer, followed by more extensive Pt oxide formation as the potential is swept to increasingly positive values.[43,210] It was observed that the half-maximum onset potential for this initial oxidation in the studied materials shifted to lower potentials for $Pt_{70}Fe_{30}$and $Pt_{50}Fe_{50}$, yielding a half-maximum potential of *ca.* 0.80 $V_{RHE}$ instead of the *ca.* 0.85 $V_{RHE}$ value observed in $Pt_{90}Fe_{10}$ and the commercial Pt/C catalyst. This shift demonstrates that the Pt in these more Fe-rich samples was able to more easily adsorb species such as −OH. This enhanced affinity for oxygenated species was also found to correlate with shorter Pt–Pt bond lengths in $Pt_{70}Fe_{30}$ and $Pt_{50}Fe_{50}$ (2.72 $Å^{-1}$ versus 2.775 $Å^{-1}$), as determined from Pt $L_3$-edge FT-EXAFS fitting results.

Linear sweep voltammetry was used to measure both the current densities and mass-normalized currents exhibited by each sample. Figure 4.7b (inset) shows that all three Pt–$FeO_x$ nanoparticles shared linear sweep voltammetry profiles that were very similar after normalization, but differed from that of Pt/C. The observed half-maximum potentials for these samples occurred at *ca.* 0.88 $V_{RHE}$ instead of *ca.* 0.83 V, representing facilitation of the ORR process and granting the nanoparticles a broader range of operating potentials. Voltammograms normalized by the ECSA of each sample are shown in Figure 4.7c and illustrate the markedly increased activities of the Pt–$FeO_x$ nanoparticles as a function of their Fe content. This effect is further illustrated in Figure 4.7d, wherein current densities were observed to increase by up to a factor of two under diffusion-

controlled conditions and by up to a factor of ten under kinetically controlled conditions. Thus, a positive correlation between both the specific ORR activity of the Pt–$FeO_x$ electrocatalysts and their relative Fe contents was observed.

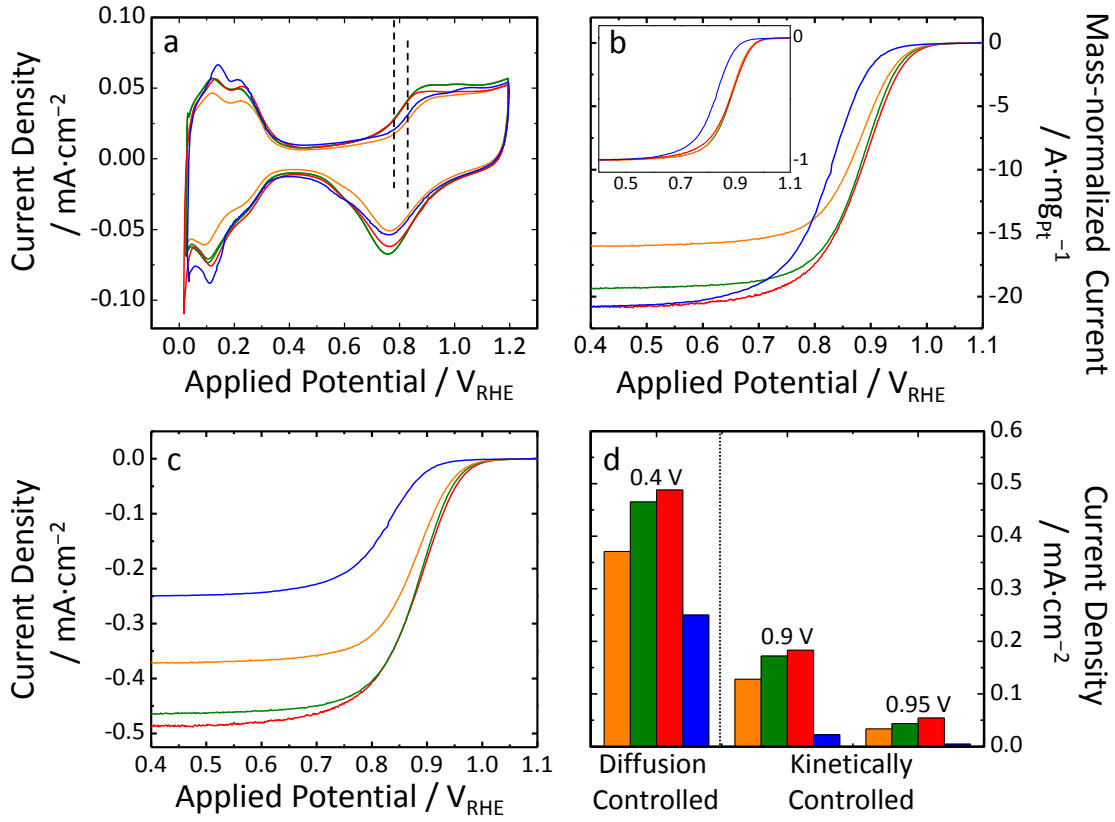


**Figure 4.7.** (a) Cyclic and (b) linear sweep voltammograms normalized by ECSA, (c) linear sweep voltammograms normalized by Pt mass, and (d) current densities for each Pt–$FeO_x$ catalyst in various regions of interest. Coloured curves and bars represent $Pt_{90}Fe_{10}$ (orange —), $Pt_{70}Fe_{30}$ (green —), $Pt_{50}Fe_{50}$ (red —), and Pt/C (blue —) samples, respectively. Adapted with permission from Reference 168.

The positive correlation between Fe content and increasing ORR activity can be interpreted by combining the Pt–$FeO_x$ surface activity results with their structural and electronic information from XANES, EXAFS, and *ab initio* calculations presented previously. Shorter Pt–Pt bond lengths have been observed to correlate with higher ORR activity in Pt catalysts,[188] particularly in the case of bimetallic Pt nanoparticles. Coincidently, the Pt–$FeO_x$ nanoparticles exhibiting the highest electrocatalytic activities ($Pt_{70}Fe_{30}$ and $Pt_{50}Fe_{50}$) were found to also have significantly shorter Pt–Pt bond lengths

than both $Pt_{90}Fe_{10}$ and the Pt/C reference. Thus, the effect of the Pt–Pt bond length seems to contribute significantly to the observed ORR performance of the Pt–$FeO_x$ nanoparticles.

In addition, it was deduced from EXAFS results (as discussed previously) that the nanoparticles with higher Fe content should have a tendency toward increased Fe diffusion into the Pt core region. This could account, at least in part, for the higher ORR activity for the nanoparticles with more Fe content. Although both XANES and EXAFS results showed a trend toward relatively less low-valent Fe as the Fe content increased, the predominance of the $FeO_x$ phase could easily obscure any increase in Pt–Fe interactions. *Ab initio* calculations indicated that both Pt–FeO and Pt–Fe interactions were able to induce a shift of the Pt valence d-band to lower energy levels, which has also been recognized as a favorable factor in the enhanced ORR activity of Pt.[188] This dependence of surface reactivity on Fe content would, thus, provide an explanation for the slightly higher ORR reactivity of $Pt_{50}Fe_{50}$ relative to $Pt_{70}Fe_{30}$.

## 4.6 Conclusions

In summary, a simple and clean CO-reduction method was used to prepare a series of carbon-supported, nearly monodisperse platinum–iron oxide nanoparticles with varied Pt−Fe ratios ($Pt_{90}Fe_{10}$, $Pt_{70}Fe_{30}$, and $Pt_{50}Fe_{50}$). In conjunction with HRTEM imaging, XAS measurements made from the perspectives of both Pt and Fe demonstrated that the three nanoparticle samples consisted of Pt cores with partial surface layers of amorphous iron oxide, but did not rule out the possible presence of discrete FeOx nanoparticles. Detailed information regarding nanoparticle local structure and electronic properties was obtained by analyzing the XANES and EXAFS data, and was further supported by computational

results. Remarkably, the ORR activity of these Pt–$FeO_x$ nanoparticles was found to be superior to that of the commercial Pt/C catalyst and dependent on the Pt−Fe molar ratio. The results of this analysis suggest that this enhanced catalytic activity is the result of Fe incorporation into Pt, in good agreement with prior literature investigations of PtFe nanoparticle systems. Furthermore, an essential role was played by XAS in the characterization of the Pt–$FeO_x$ samples, illustrating its suitability for addressing the challenges posed by such complex materials.

Based upon these results, however, it could not be definitively determined whether the observed enhancement in ORR activity was due to electronic effects arising from the presence of surface Fe/$FeO_x$ species or to the lattice strain indicated by shortened Pt–Pt bond lengths. These catalytic tests also represented a first foray into the field of electrochemistry, and could be extended to afford further information regarding these samples. Additionally, the possibility of significant changes in the surface structure of the Pt–$FeO_x$ nanoparticles under the conditions used for electrochemical measurements, including strong acidity and rapidly changing applied potentials, was still a major concern. In order to better understand the role of the Fe component in these samples, as well as their electrochemical stability, further studies were required.

# Chapter 5 – Surface Reconstruction and Reactivity of Pt–$FeO_x$ Nanoparticles

Adapted with permission from Reference 206:
Duchesne, P.N.; Chen, G.; Zhao, X.; Zheng, N.; Zhang, P. "Surface Reconstruction and Reactivity of Platinum–Iron Oxide Nanoparticles" *J. Phys. Chem. C,* **2014**, *118* (49), 28861-28867.


## 5.1 Contributions

PND and GC (College of Chemistry and Chemical Engineering, Xiamen University) synthesized the Pt–$FeO_x$ nanoparticles and deposited them onto the carbon powder support. XZ (College of Chemistry and Chemical Engineering, Xiamen University) acquired TEM images and PND performed image analyses. PND isolated samples from the electrode surface, acquired and analyzed CV and ORR activity data, performed XAS measurements and data analysis, and wrote the manuscript. PZ supervised PND and helped with manuscript revision. NZ (College of Chemistry and Chemical Engineering, Xiamen University) supervised GC and XZ.

## 5.2 Foreword

The study described in Chapter 4 represented a first foray into the characterization of multi-metallic Pt-based nanoparticles and showed good success for the use of XAS techniques. Although the as-synthesized samples exhibited a Pt–$FeO_x$ structure instead of forming metallic PtFe nanoparticles, their electrocatalytic activities were still improved relative to a commercial Pt/C catalyst. The relationship between the surface Fe species and the catalytic activity enhancement was still unclear, however, due largely to the possibility of significant modification of the nanoparticle surfaces on exposure to electrocatalytic reaction conditions. The study presented in this chapter thus serves as a

follow-up to the initial characterization of the Pt–$FeO_x$ samples. Emphasis is placed on determining the extent of nanoparticle surface modification under electrocatalytic conditions, further characterizing the electrocatalytic activity of Pt–$FeO_x$, and investigating the electronic effects of surface Fe species via experimental and computational methods.

## 5.3 Introduction

While previous research did reveal that enhanced ORR activity is exhibited by Pt–$FeO_x$ nanoparticles, it was unable to clarify whether this enhancement was due to electronic effects from the presence of Fe/$FeO_x$ species or surface strain. Electrochemical measurements also showed that the Pt–$FeO_x$ voltammograms continued to change over the course of several tens of cycles. One possible explanation for this change is the inherently lower stability of non-noble metal components of these nanoparticles under standard fuel cell operating conditions (corrosive electrolytes, strong electrical potentials, *etc.*), which are prone to leaching.[191,208] As a result, the structure of the active catalyst could differ significantly from its as-synthesized form. The effect of leaching on surface structure has previously been explored using various combinations of Pt and 3d transition metals, revealing that such processes lead to the formation of a Pt-enriched "skin" due to the lesser stability on the non-noble metal component.[47,184,212] Interestingly, some of the same studies also revealed 3d metal enrichment in the first sublayer of metal atoms, which was implicated in the enhanced activity of such surfaces.[47] Furthermore, changes in the surface structure of even pure Pt nanoparticles can be effected via electrochemical treatments.[121] As a result of these factors, there was no guarantee that the characterization data accurately described the catalytic material in its active state.

In order to investigate the possible impact of surface structural changes on the electrocatalytic activity of Pt–$FeO_x$ nanoparticle catalysts, samples of each elemental composition (*i.e.*, $Pt_{90}Fe_{10}$, $Pt_{70}Fe_{30}$, and $Pt_{50}Fe_{50}$) were analyzed both before and after electrochemical characterization. In addition to observing any gross morphological changes to the particles themselves using TEM, changes in their local structure and electronic properties are elucidated through the use of EXAFS and XANES analyses. A more thorough investigation of the electrocatalytic activities of these samples was also performed, providing deeper insight into correlations between the structure and activity of Pt catalysts following electrocatalytic testing in acidic media.

## 5.4 Experimental Methods

### 5.4.1 Sample Preparation

Pt–$FeO_x$ nanoparticles synthesized previously using a facile, "clean" method were used in this study.[172] Briefly, these nanoparticles were formed at elevated temperatures in OAm solution under a reducing atmosphere of carbon monoxide. Control of the Pt:Fe precursor ratio in the reaction mixture was used to generate nanoparticles with differing elemental compositions. Surface-protecting OAm ligands were removed via ligand exchange with excess *n*-butylamine in the presence of suspended Vulcan XC-72 carbon powder, inducing immobilization of the nanoparticles onto the carbon support (30 wt% Pt loading). Catalyst loading was measured using inductively coupled plasma optical emission spectroscopy. A commercial Pt catalyst (HiSPEC 3000, 20 wt% loading, denoted "Pt/C") was also used as a reference during characterization of the Pt–$FeO_x$ samples.

Although *in situ* measurements were precluded by the lack of an on-site electrochemical systems (and would have been significantly complicated by the need to properly orient the incident X-ray beam, operating RDE electrochemical cell, and fluorescence detector for data collection), it was still possible to study the structure of the Pt–$FeO_x$ samples using *ex situ* methods. Following electrochemical characterization, samples of the post-treatment Pt–$FeO_x$ and Pt/C materials were obtained for further XAS analysis. First, the RDE was removed from the electrolyte solution and carefully dried by wicking away any residual liquid with the edge of a Kimwipe tissue. After allowing the sample several minutes to dry, a strip of cellophane tape was applied to the surface of the glassy carbon RDE; removing the tape also removed a thin, but appreciable, layer of sample. This was repeated several times to ensure collection of sufficient material before the exposed catalyst sample was sealed-in with a second strip of tape.

### 5.4.2 Cyclic Voltammetry

A Pine Instrument Company RDE system was used to perform electrochemical measurements in the laboratory of Prof. Jeff Dahn at Dalhousie University. Full experimental details have been presented previously.[172] In brief, a three-electrode cell was assembled, consisting of a glassy carbon RDE working electrode, Pt wire counter electrode, and Koslow mercury/mercurous sulfate reference electrode in 0.1 M perchloric acid ($HClO_4$) electrolyte. Glassware was decontaminated by boiling in deionized water prior to use. Measurements were then conducted according to standard ORR characterization procedures.[208]

To investigate the effects of electrochemical treatment on Pt–$FeO_x$ nanoparticles, samples in $Ar_{(g)}$-saturated electrolyte were exposed to applied potentials between 0.02 and

1.2 $V_{RHE}$. The treatment continued for 50 cycles at a sweep rate of 50 $mV \cdot s^{-1}$. The activity of each sample with regards to the ORR was measured by saturating the electrolyte solution with $O_{2(g)}$ and then sweeping the applied potential over the same potential range used for the initial electrochemical treatment. A rotation rate of 1,600 RPM was used for all experiments. Area-specific current densities were obtained by correcting these experimental data to account for key factors, including non-Faradaic contributions, mass transport at the electrode surface, and ECSA for each sample.[213]

### 5.4.3 X-ray Absorption Spectroscopy

XAS data acquisition was performed using the Sector 20-BM beamline of the Advanced Photon Source at Argonne National Laboratory in Argonne, IL. A double-crystal Si(111) mirror monochromator was used for wavelength selection and, in conjunction with a Rh-coated Si focusing mirror, detuned to 80% in order to reject higher harmonics. Standard gas-ionization chamber detectors were used for collecting reference foil data, whereas the limited quantity of both the Pt–$FeO_x$ and Pt/C samples necessitated the use of a more sensitive a 12-element Ge fluorescence detector. A cryostatic sample holder was used to maintain a stable temperature of 50 ± 1 K (for pre-treatment samples) or 90 ± 1 (for post-treatment samples) in order to further enhance the intensity of the EXAFS signal via suppression of thermal vibrations, thereby obtaining better signal-to-noise ratios. Processing and fitting of XAS data were performed using the IFEFFIT software suite.[77]

### 5.4.4 Transmission Electron Microscopy

Due to the fact that they had been preserved between strips of cellophane tape for XAS characterization, preparation of the post-treatment nanoparticle samples for TEM

analysis required some processing. After carefully separating the strips of tape encompassing the post-treatment sample material, both strips were inserted into a small (1.5 mL) sample vial filled with *n*-hexane and sonicated until their adhesive dissolved, releasing the sample from the cellophane backing. The undissolved cellophane backing was then carefully removed, and the remaining suspension centrifuged at 15,000 RPM for 5 min to separate the sample material from the supernatant, which was then decanted. Each sample was then washed with 1 mL of laboratory grade ethanol (*i.e.*, sonicated, then centrifuged again under the same conditions). Finally, each sample was dispersed in 200 μL of ethanol via sonication and drop-cast onto Formvar-coated copper TEM grids. Sample imaging was performed at the Dalhousie University Scientific Imaging Suite using a Tecnai F-30 transmission electron microscope operated at 300 kV in bright-field imaging mode. Size distributions of the nanoparticles were measured using MacBiophotonics ImageJ software and several representative images from each sample.[199]

## 5.5 Results and Discussion

### 5.5.1 Cyclic Voltammetry

Cyclic voltammograms of both the Pt–$FeO_x$ samples and Pt/C reference catalyst are presented in Figure 5.1. After 50 cycles, marked changes were observed in the voltammograms over several regions of interest. Most of these regions are characteristic of Pt, but peaks attributable to the oxidation and reduction of the $Fe^{2+}/Fe^{3+}$ redox couple (*ca.* 0.74 $V_{RHE}$ on the forward sweep and *ca.* 0.70 $V_{RHE}$ on the reverse sweep) were apparent in the Pt–$FeO_x$ voltammograms.[214] In general, it was observed that peaks

indicative of H-adsorption/desorption (0.05 to 0.35 $V_{RHE}$) and Pt-surface reduction peaks increased in intensity, those representative of $H_{2(g)}$ evolution (*ca.* 0 $V_{RHE}$) decreased in intensity, and those reflective of Pt-surface reduction increased in intensity. In conjunction with the differences indicated by XAS data analysis (*vide infra*), these changes are consistent with restructuring of the Pt surface as a result of potential cycling, and indicate the emergence of distinct Pt(111) and Pt(110) crystallographic facets from a more irregular initial structure.[209] Peaks associated with the $Fe^{2+}/Fe^{3+}$ redox couple were observed to disappear after only a few scans, suggesting that these species were only initially present at the Pt surface and dissolved readily into the acidic electrolyte solution.

As expected, the most intense $Fe^{2+}/Fe^{3+}$ feature was observed for $Pt_{50}Fe_{50}$, which has the greatest Fe content; however, the $Pt_{70}Fe_{30}$ sample did not exhibit a peak intensity intermediate between the former sample and $Pt_{90}Fe_{10}$, as might have been expected given its relative composition. It is likely that this discrepancy is due to the samples being immersed in the acidic electrolyte for different lengths of time prior to the onset of electrochemical cycling. In contrast with that located at the nanoparticle surface, Fe located beneath the Pt surface layer should be both physically shielded from the acidic electrolyte and electronically stabilized by its numerous Pt neighbours. It is to these stabilized sub-surface Fe atoms that the enhanced activity of the Pt-$FeO_x$ nanoparticles is attributed.

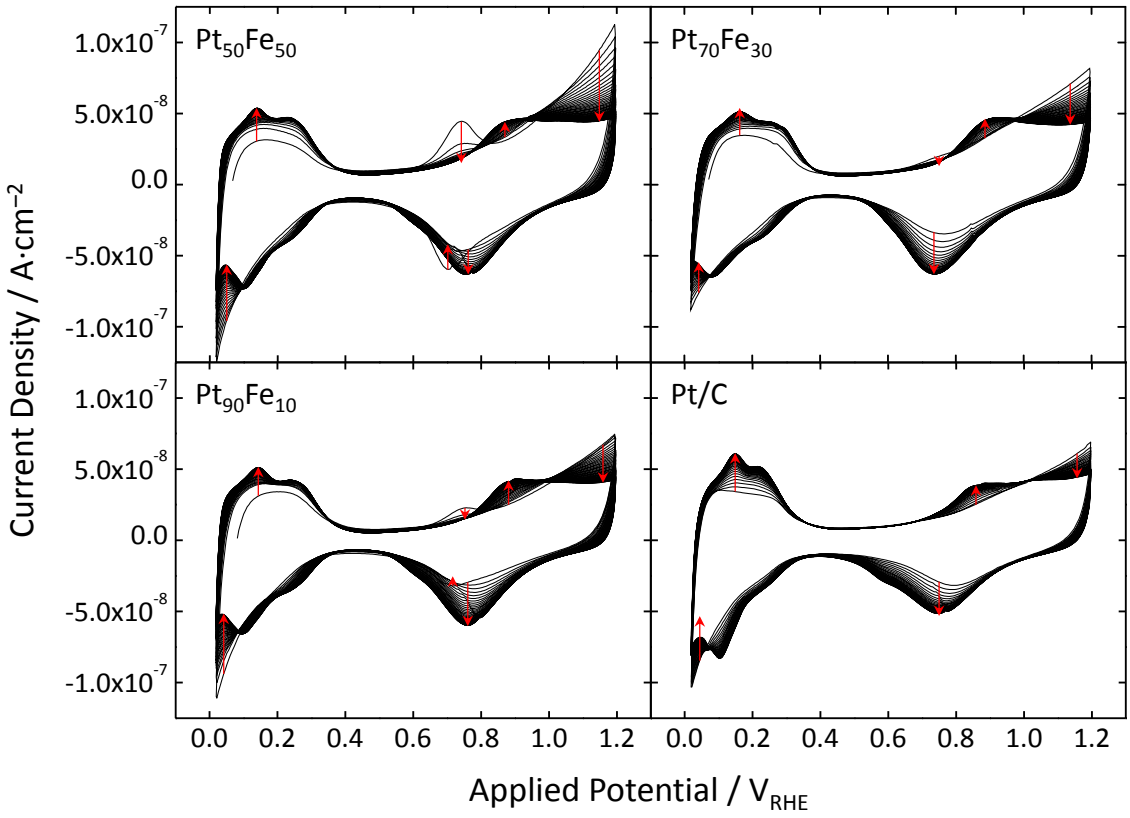


**Figure 5.1.** Evolution of cyclic voltammograms from Pt–$FeO_x$ and Pt/C reference samples over the course of 50 cycles. Red arrows indicate the direction of change for each region of interest. Adapted with permission from Reference 206.

### 5.5.2 Transmission Electron Microscopy

TEM images (see Figure 5.2) were acquired by Xiaojing Zhao for each nanoparticle sample in order to ensure no drastic changes in morphology had occurred as a result of the electrochemical treatment. In fact, very little change was observed, with particle sizes of 3 ± 1 nm, 4 ± 1 nm, 5 ± 1 nm, and 4 ± 1 nm being observed for $Pt_{50}Fe_{50}$, $Pt_{70}Fe_{30}$, $Pt_{90}Fe_{10}$, and Pt/C, respectively. These values matched closely with those determined for the samples prior to electrochemical treatment (3.5 ± 0.5 nm, 4.0 ± 0.5 nm, 4.4 ± 0.6 nm, and 2.8 ± 0.7 nm, respectively), suggesting that no significant particle aggregation occurred during electrochemical cycling. Close analysis of the TEM images reveals that some fusion of adjacent particles to form oblong, rod-like structures did occur

for a small number of particles; however, such behavior has also been reported by other researchers and does not appear to degrade catalyst performance as significantly as does the formation of large, spherical aggregates.[11] Overall, only minor structural changes were observed relative to the results of pre-treatment TEM analysis.

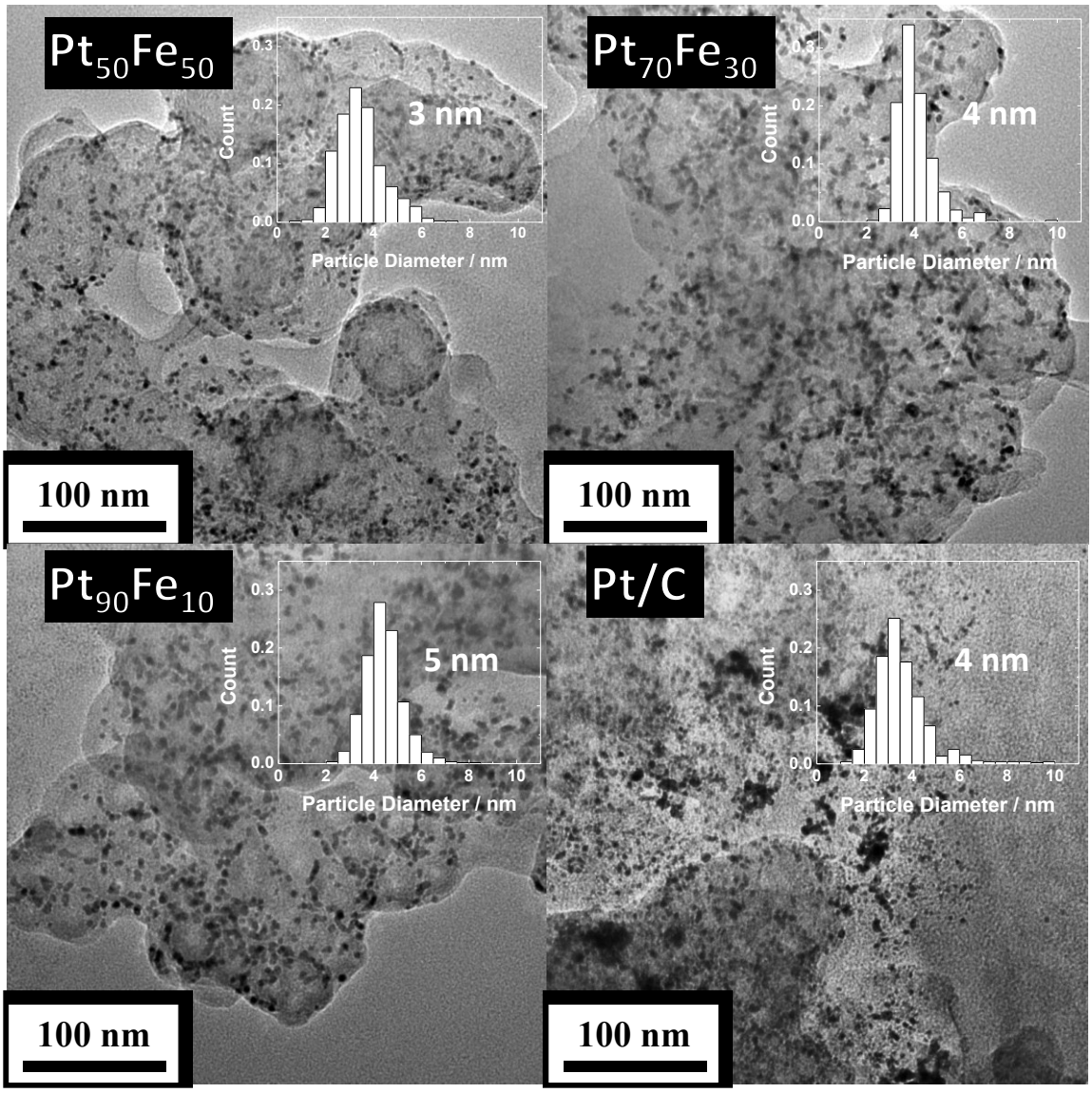


**Figure 5.2.** TEM micrographs of Pt–$FeO_x$ and reference Pt/C catalyst samples after electrochemical treatment. Inset histograms depict measured nanoparticle diameters as measured from a series of images (444 < N < 599). Adapted with permission from Reference 206.

### 5.5.3 X-ray Absorption Spectroscopy

XAS measurements were performed at the Pt $L_3$ absorption edge in order to study Pt–$FeO_x$ and Pt/C catalyst samples both before and after electrochemical cycling. XANES spectra from these measurements are presented in Figure 5.3. Although the Pt–$FeO_x$ samples appear to have behaved differently with regards to electrochemical treatment, the observed changes can, nonetheless, provide useful insight into their structure. Overall, electrochemical treatment appears to have had the effect of homogenizing the XANES spectra of the Pt–$FeO_x$ nanoparticles. Both $Pt_{50}Fe_{50}$ and $Pt_{90}Fe_{10}$ samples exhibited little change in white line shape or intensity as a result of treatment, indicating that changes to the average Pt environment in these samples were minimal. In contrast, the white line intensity of $Pt_{70}Fe_{30}$ increased slightly post-treatment, while that of Pt/C decreased.

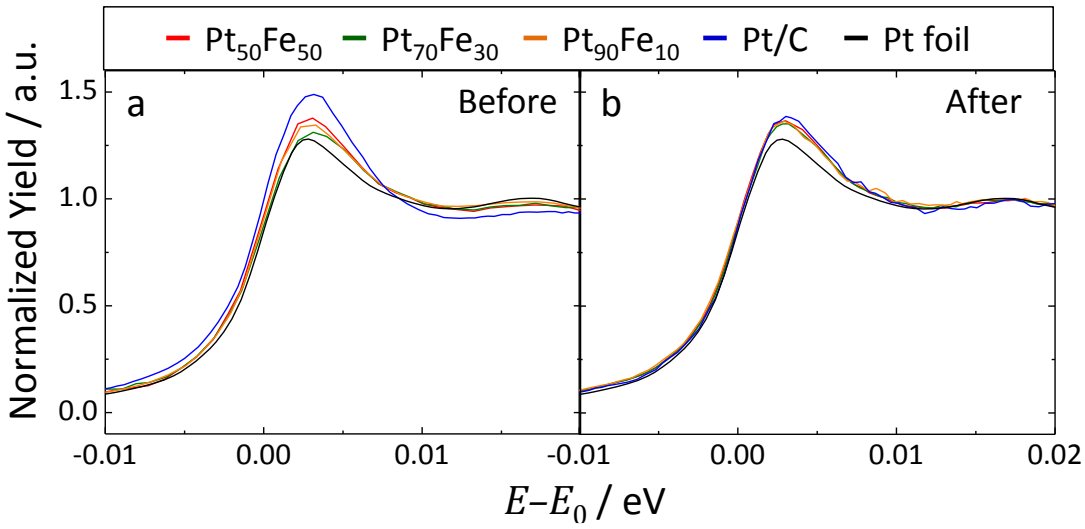


**Figure 5.3.** Comparisons of Pt $L_3$-edge XANES spectra acquired (a) before (at 50 K) and (b) after (at 90 K) electrochemical treatment in 0.1 M $HClO_4$ electrolyte. Adapted with permission from Reference 206.

From a basic understanding of XANES principles, the observed changes can be interpreted as arising from changes in the Pt d-electron density, with decreased electron density resulting in increased white line intensity.[215] This decreased electron density of Pt in $Pt_{70}Fe_{30}$ after electrochemical treatment may be related to the loss of charge transfer

from Fe to Pt atoms in the nanoparticles. The fact that the Pt electron density is reduced as a result of treatment could indicate that a significant amount of metallic Fe near the surface was removed from the nanoparticles alongside the surface Fe-oxides. This is also consistent with the conclusion that the $Pt_{70}Fe_{30}$ sample contains a relatively greater amount of metallic Fe than the other Pt–$FeO_x$ samples.

The increase in d-electron density experienced by Pt/C should not be due to leaching of its components (primarily Pt and O) as was the case for the Pt–$FeO_x$ samples, but could be explained by a reduction of oxidized surface Pt species accumulated during exposure to air. In order to better understand the root causes for these changes, it is helpful to closely study the local structure of each sample. FT-EXAFS spectra for Pt–$FeO_x$ samples and Pt/C are presented in Figure 5.4. Despite being obtained at a higher temperature (90 ± 1 K, versus 50 ± 1 K for the untreated data), the post-treatment spectra exhibited more intense peaks corresponding to Pt–M scattering paths. As the unusually low intensity observed for the Pt–M paths prior to cycling has been attributed to destructive interference between Pt–Pt and Pt–Fe scattering paths, this increased intensity could be understood as a decrease in one of these two contributions to the overall peak intensity.

Overall, the qualitative similarity of the FT-EXAFS spectra, especially at higher *R*-values, indicates that the samples have become more structurally similar. Differences introduced during sample synthesis appear to have been removed by the electrochemical cycling process. Additionally, the intensity reduction of the Pt–O peak of Pt/C (*ca.* 1.7 Å) indicates that less Pt-oxide is present post-treatment, further supporting the reduction of surface Pt based on XANES analysis. In order to fully characterize the structural changes in these samples, fitting of experimental FT-EXAFS spectra was performed.

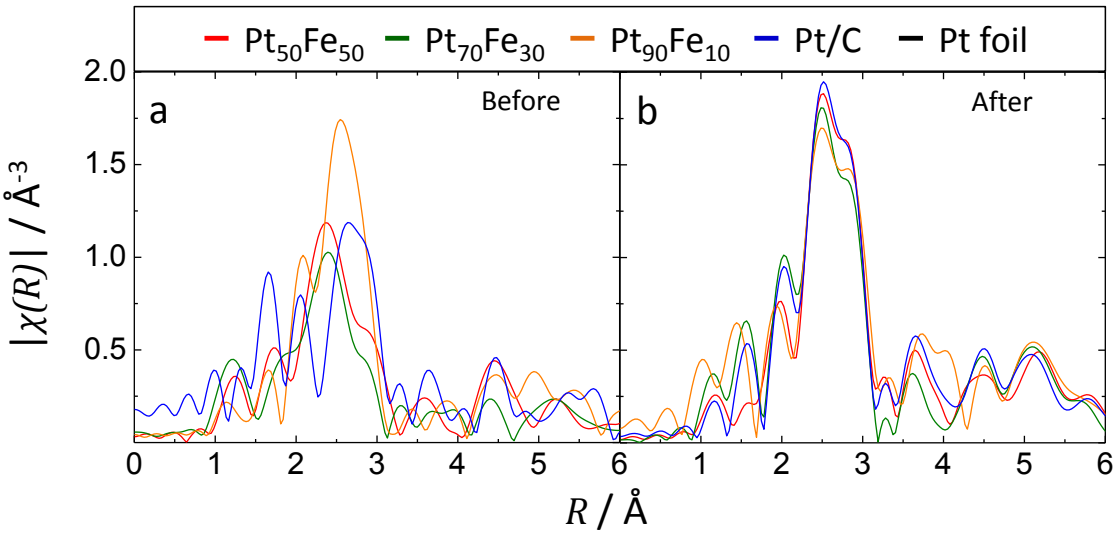


**Figure 5.4.** Comparisons of Pt $L_3$-edge FT-EXAFS spectra for Pt–$FeO_x$ and Pt/C samples acquired (a) before and (b) after electrochemical treatment in 0.1 M $HClO_4$ electrolyte. Adapted with permission from Reference 206.

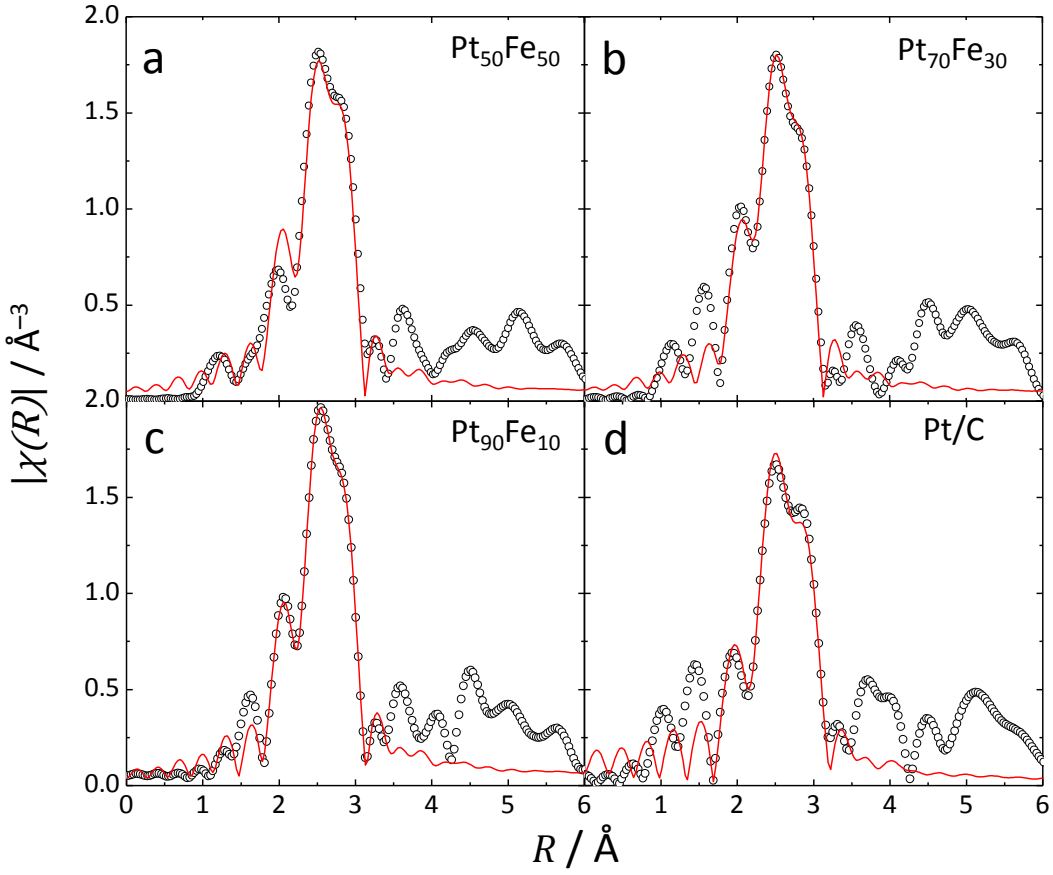


**Figure 5.5.** Pt $L_3$-edge FT-EXAFS experimental (hollow circles) and fitted spectra (red lines) for electrochemically treated (a) $Pt_{50}Fe_{50}$, (b) $Pt_{70}Fe_{30}$, (c) $Pt_{90}Fe_{10}$, and (d) Pt/C samples. Adapted with permission from Reference 206.

Fitted FT-EXAFS spectra are presented in Figure 5.5. Corresponding structural parameters obtained from the fitting of pre-treatment[172] and post-treatment Pt–$FeO_x$ and Pt/C samples are presented in Table 5.1. Immediately apparent from these data is the significant decrease in the degree of Pt–Fe bonding after electrochemical cycling; however, as indicated by their respective Pt–Fe *CN*s, both $Pt_{70}Fe_{30}$ and $Pt_{90}Fe_{10}$ retained a measurable degree of Pt–Fe interaction. Given the structural information available from cyclic voltammetry and XANES analyses, this is likely due to the relatively large amount of metallic Fe located just beneath the Pt surfaces of the nanoparticles. Further support for this conclusion is afforded by the observed Pt−Fe bond lengths.

**Table 5.1.** Structural parameters obtained from fitting of Pt $L_3$-edge FT-EXAFS spectra prior to, and following, electrochemical cycling. Uncertainties in the last decimal place of each value are indicated in parentheses (treated as one standard deviation). A double asterisk (**) indicates that contributions from the Pt–Fe scattering paths in these samples were too weak to be measured. Adapted with permission from Reference 206.

| | | before treatment | | | | after treatment | | | |
|---|---|---|---|---|---|---|---|---|---|
| Sample | Path | *CN* / a.u. | *R* / Å | $\sigma^2$ / $10^{-3}$ Å$^2$ | $\Delta E_0$ / eV | *CN* / a.u. | *R* / Å | $\sigma^2$ / $10^{-3}$ Å$^2$ | $\Delta E_0$ / eV |
| $Pt_{90}Fe_{10}$ | Pt–Fe | 1.0(3) | 2.67(2) | 3(1) | 1(2) | 0.6(2) | 2.67(1) | 3(1) | 5(1) |
| | Pt–Pt | 8(1) | 2.775(5) | | | 10(1) | 2.75(1) | | |
| $Pt_{70}Fe_{30}$ | Pt–Fe | 1.7(7) | 2.70(3) | 6(2) | 2(2) | 0.7(6) | 2.67(5) | 4(1) | 4(2) |
| | Pt-Pt | 7(2) | 2.72(1) | | | 11(3) | 2.75(1) | | |
| $Pt_{50}Fe_{50}$ | Pt–Fe | 1(1) | 2.72(9) | 3(3) | 3(4) | ** | ** | 4(1) | 4(2) |
| | Pt-Pt | 7(3) | 2.72(3) | | | 11(2) | 2.75(1) | | |
| Pt/C | Pt–O | 1.9(3) | 2.04(2) | 2(2) | 10(1) | ** | ** | 3(1) | 6(1) |
| | Pt–Pt | 6(2) | 2.78(1) | | | 10(1) | 2.76(1) | | |

For the pre-treatment samples, it was observed that the mean Pt−Fe bond length was correlated with greater Fe content. On the basis of the Fe K-edge XANES results from the as-synthesized Pt−$FeO_x$,[172] samples with greater Fe content also possessed relatively more Fe-oxide than metallic Fe. Thus, it can be inferred that a predominance of

metallic Pt−Fe interactions yields shorter average bond lengths (*ca.* 2.67 Å) than does that of oxide Pt−Fe interactions (*ca.* 2.72 Å). Therefore, the relatively short Pt−Fe bond length for post-treatment $Pt_{70}Fe_{30}$ indicates that the remaining Fe is likely present in a metallic environment.

With regard to the observed Pt–Pt *CN*s, an increase was observed for all samples as a result of electrochemical cycling. This is easily explained by surface reconstruction, as is indicated by the evolution of the characteristic H-adsorption/desorption peaks in the voltammograms for each sample. From the low Pt–Fe and Pt–Pt *CN*s obtained prior to treatment, it appears that both the Pt–$FeO_x$ samples and Pt/C catalyst possessed irregular or highly defected surface morphologies in their as-synthesized forms, likely facilitated by the presence of a stabilizing surface Fe oxide layer. The harsh conditions introduced by electrochemical cycling have clearly proven sufficient to effect considerable transformation of this initial structure, resulting in higher *CN*s more indicative of an ordered Pt surface.

### 5.5.4 ORR Activity Testing

The ORR activities of the Pt–$FeO_x$ and Pt/C samples were evaluated via linear sweep voltammetry, with the resultant normalized current densities and Tafel plots presented in Figure 5.6. By further correcting for mass-transfer limited diffusion using the Levich relation,[208] reliable measures of specific current density ($j_{specific}$) under kinetically controlled conditions (*i.e.*, 0.95 $V_{RHE}$) were obtained. Half-wave potentials ($E_{1/2}$, measured at one-half the maximum diffusion-limited current density) are generally indicative of the thermodynamic efficiency (or voltage efficiency) of an electrochemical reaction.[216] In the case of ORR activity, a more positive potential is indicative of a lower

overpotential being required to drive the reaction, and, thus, greater electrocatalytic efficiency. Tafel plots were also prepared and fitted using linear regression in order to obtain their characteristic Tafel slopes. Experimentally determined values of $E_{1/2}$, $j_{specific}$, and Tafel slope for each sample are presented in Table 5.2. An anomalous feature was observed in the data from $Pt_{70}Fe_{30}$ at *ca.* 0.8 $V_{RHE}$, making the veracity of its superior performance uncertain. From these data, it appears that $Pt_{70}Fe_{30}$ exhibits the largest $E_{1/2}$ of the four samples tested (0.965 $V_{RHE}$), followed by $Pt_{90}Fe_{10}$ (0.939 $V_{RHE}$), $Pt_{50}Fe_{50}$ (0.917 $V_{RHE}$), and Pt/C (0.913 $V_{RHE}$).

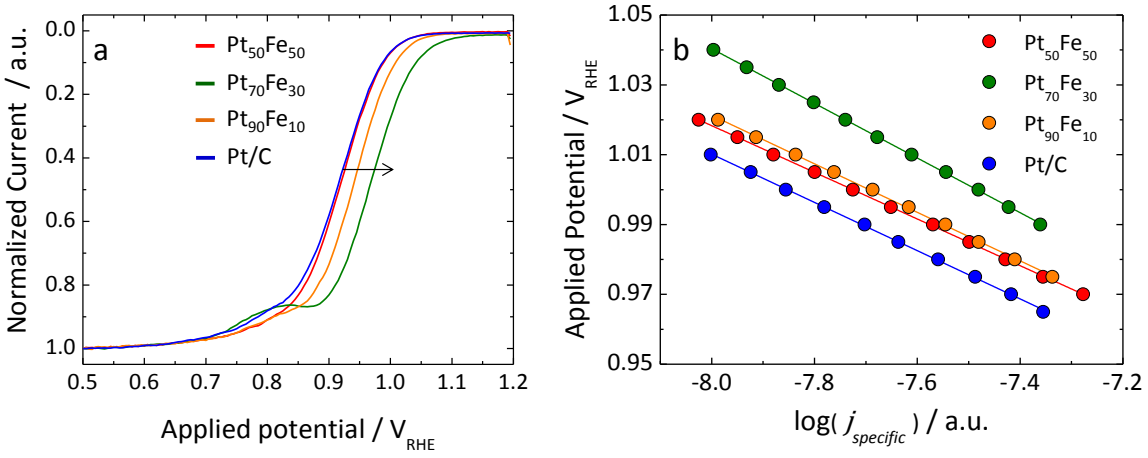


**Figure 5.6.** (a) Current density plots normalized by maximum diffusion-limited current (at 0.5 $V_{RHE}$) and (b) Tafel plots of the Pt–$FeO_x$ samples and Pt/C reference. Adapted with permission from Reference 206.

**Table 5.2.** Figures of merit for the ORR activities of Pt–$FeO_x$ and Pt/C samples. Uncertainties representative of noise in the experimental data are shown in parentheses; these uncertainties represent three standard deviations. Adapted with permission from Reference 206.

| Sample | Half-wave Potential ($V_{RHE}$) | Specific Current Density ($10^{-2}$ mA·cm$^{-2}$) | Tafel Slope ($mV_{RHE}$·dec$^{-1}$) |
|---|---|---|---|
| $Pt_{90}Fe_{10}$ | 0.939(1) | 9.9(2) | –69(1) |
| $Pt_{70}Fe_{30}$ | 0.965(1) | 13.2(3) | –78(1) |
| $Pt_{50}Fe_{50}$ | 0.917(1) | 9.8(3) | –67(1) |
| Pt/C | 0.913(1) | 7.1(2) | –69(1) |

In keeping with the obtained half-wave potentials, $Pt_{70}Fe_{30}$ also offered the highest kinetic current density ($1.32 \times 10^{-1}$ mA·cm$^{-2}$). $Pt_{90}Fe_{10}$ had the next best $j_{specific}$ ($9.9 \times 10^{-2}$ mA cm$^{-2}$) but was not significantly better than $Pt_{50}Fe_{50}$ ( $9.8 \times 10^{-2}$ mA·cm$^{-2}$), and Pt/C demonstrated the poorest performance (just $7.1 \times 10^{-2}$ mA·cm$^{-2}$). One possible explanation for the similar $j_{specific}$ values of $Pt_{90}Fe_{10}$ and $Pt_{50}Fe_{50}$, despite the more positive $E_{1/2}$ of the former, is that both two-electron ($O_2 + 2H^+ + 2e^- \rightarrow H_2O_2$) and four-electron ($O_2 + 4H^+ + 4e^- \rightarrow 2H_2O$) pathways exist for the reduction of $O_{2(g)}$ at Pt surfaces.[217] While the latter typically predominates under these conditions, the former is also viable. It could be possible that the relatively greater $j_{specific}$ of $Pt_{50}Fe_{50}$ is due to the competing two-electron formation of $H_2O_2$, thereby explaining its similar performance to $Pt_{90}Fe_{10}$ despite the differences in their local structures (as indicated by EXAFS analysis). Additional experiments performed using a rotating ring disk electrode would allow the contributions from $H_2O_2$ formation to be clearly quantified; however, the similar Tafel slopes for these samples suggest that they follow the same reaction mechanism, and so this is not the best explanation for the results.

Experimentally, the reduction of $O_{2(g)}$ on Pt corresponds to Tafel slopes of approximately −60 mV·dec$^{-1}$ at more positive potentials (*i.e.*, greater than 0.8 $V_{RHE}$) and −120 mV·dec$^{-1}$ for measurements obtained at less positive potentials (*i.e.*, less than 0.8 $V_{RHE}$).[218] This is explained by a difference in the rate-determining step of the ORR on Pt/Pt–O and pure metallic Pt surfaces, respectively. A comparison of the samples studied revealed slopes well in line with those published previously for Pt and PtFe nanoparticle samples[219] with one exception. $Pt_{70}Fe_{30}$ demonstrated a Tafel slope 13 % greater in magnitude than those of the other samples (−78 mV·dec$^{-1}$ versus *ca.* −68 mV·dec$^{-1}$); this

suggests that there may be some contributions from $H_2O_2$ formation in the $Pt_{70}Fe_{30}$ data, and could also explain the unusual feature in its data at *ca*. 0.8 $V_{RHE}$. The small deviations of the other Pt–$FeO_x$ samples from the ideal value for a mixed Pt/Pt–O surface is most likely due to their small particle size, which can result in increasingly steep Tafel slopes for nanoparticles in the size range of 6 to 1 nm.[220]

## 5.6 Conclusions

In summation, XAS data analysis was successfully used in conjunction with electrochemical measurements to characterize the physical changes in Pt–$FeO_x$ nanoparticle surfaces, which occurred due electrochemical cycling in acidic media. It was found that, following electrochemical treatment, surface Fe and $FeO_x$ species were removed, leaving behind a P-rich skin, as described previously in the literature. As a result, it was deduced that activity enhancement observed for these nanoparticle catalysts was due to the effects of sub-surface Fe species; however, whether this was due to electronic or surface strain effects was still unclear. Regardless, it was observed that those samples retaining measurable quantities of Fe ($Pt_{70}Fe_{30}$ and $Pt_{90}Fe_{10}$) exhibited the greatest reduction in ORR overpotential, although the values observed for Pt70Fe30 were somewhat called into question by the possibility of competing $H_2O_2$ formation at the electrode surface. In addition to the helping explain the role of Fe in enhancing electrocatalytic activity, characterization of the used nanoparticle catalysts revealed the subsequent reconstruction of their surfaces following electrochemical treatment. This reconstruction resulted in significant changes in the Pt–$FeO_x$ materials, highlighting the critical importance of *in situ* and/or post-catalyst characterization, and again emphasizing the utility of XAS techniques in contributing to such analyses.

# Chapter 6 – Growth Mechanism, Local Structure, and Electronic Properties of Pt Clusters Formed on Ag Nanoparticle Surfaces

Adapted with permission from Reference 216:
Duchesne, P.N.; Zhang, P. "Element-Specific Analysis of the Growth Mechanism, Local Structure, and Electronic Properties of Pt Clusters Formed on Ag Nanoparticle Surfaces" *J. Phys. Chem. C,* **2014**, *118* (37), 21714-21721.


## 6.1 Contributions

PND synthesized samples, prepared them for ICP-OES measurements, and analyzed the resulting data. ICP-OES measurements and peak fitting were performed by Daniel Chevalier (Minerals Engineering Centre, Dalhousie University). PND acquired and analyzed UV-vis absorption, TEM, and XAS data; performed *ab initio* simulations of XANES spectra; and wrote the manuscript. PZ supervised PND and helped with manuscript revision.

## 6.2 Foreword

The previous chapters have repeatedly demonstrated the utility of XAS techniques in the characterization of Pt-based nanoparticles, including bimetallics. The studies presented in Chapters 4 and 5, in particular, showed that performing measurements at both the Pt and Fe absorption edges provides invaluable structural information. However, the structure of those Pt–$FeO_x$ nanoparticles was less than ideal for catalytic applications, as the majority of the Pt material is localized within the nanoparticle cores. The study described in this chapter explores alternative syntheses to produce surface-localized Pt sites. Emphasis is placed on the formation of core-shell AgPt nanoparticles, thorough XAS characterization of their structure from both the Ag and Pt absorption edges, and corroboration of the inferred particle structures using *ab initio* methods.

## 6.3 Introduction

While the previous studies of Pt-$FeO_x$ nanoparticles were successful in terms of sample characterization, the synthesis was not well-suited to the production of metallic PtFe nanoparticles. Both mono- and bimetallic nanoparticle catalysts currently see widespread study and application in a variety of chemical processes, including fuel cell operation and the production of combustible fuels from biomass.[208,222,223] However, as discussed in previous chapters, the incorporation of some baser elements (*e.g.*, Fe) into Pt materials can be hindered by their rapid oxidation.[172] Fortunately, a satisfactory solution can be found in the combination of Pt with less costly noble metals such as Ag, leading to AgPt nanoparticles with more complex structures.[54]

In addition to being less prone to oxidation than those containing base metals (*e.g.*, Fe, Co, *etc.*), AgPt nanoparticles with core-shell structures can also be better suited to catalytic applications than pure Pt. Their primary benefit is that the surface localization of Pt can be greatly enhanced in a core-shell structure. However, the difficulty with this approach comes in controlling the growth of the shell layer; if the layer is too thick, many Pt atoms will still lie beneath the exposed surface and be inaccessible and inactive. As a result, monolayer or sub-monolayer coverage of the particle core by Pt is highly desirable; in the latter case, interfacial regions between the two metals can exist at the nanoparticle surface, upon which the catalyzed reaction may proceed differently or even more efficiently than on Pt alone.[224] Bimetallic Pt nanoparticles consisting of small Pt clusters on the surface of larger metal cores (*i.e.*, sub-monolayers) should allow for reduced cost, high catalytic surface area, and a strong interaction between Pt and the substrate. Unfortunately, obtaining a uniform coating of limited thickness can be very challenging.[225]A ready solution to this challenge is found in the use of galvanic

replacement reactions; shell thickness is limited by the ability of metal ions to access and replace less-noble surface metal atoms in these reactions, making them well-suited for the formation of monolayer and sub-monolayer nanoparticle shells.[225,226]

As is often the case for nanomaterials, the characterization of surface structure in bimetallic Pt nanoparticles using conventional techniques remains a challenge. As the previous studies on Pt–$FeO_x$ samples have demonstrated, XAS techniques can be well suited for such materials, particularly in that both the Ag and Pt environments can be probed separately (via their respective absorption edges). Attempts to employ these nanoparticles as ORR catalysts were unsuccessful, however, and so emphasis is placed on structural characterization using both experimental and *ab initio* XAS techniques. ICP-OES, UV-vis, and TEM measurements are further used to understand the structure and formation mechanism of these AgPt nanoparticles.

## 6.4 Experimental Methods

### 6.4.1 Materials

Silver nitrate ($AgNO_3$, 99.9+ %), polyvinylpyrrolidone (PVP, MW 8,000 Da), and dihydrogen hexachloroplatinate(IV) hexahydrate ($H_2PtCl_6 \cdot 6H_2O$, 99.9 %) were purchased from Alfa Aesar. Sodium borohydride ($NaBH_4$, 99%) and *n*-butylamine ($BuNH_2$, 99.5 %) were purchased from Sigma-Aldrich. Potassium hydroxide (KOH, 85+ %) and hydrochloric acid ($HCl_{(aq)}$, 36.5 to 38.0 % w/w) were purchased from ACP Chemicals. Nitric acid ($HNO_{3(aq)}$, 67 to 70 % w/w) was purchased from Caledon Laboratory Chemicals. Vulcan XC-72 carbon powder was purchased from Cabot Corporation. Deionized water (DIW, 18.2 MΩ·cm) was obtained using a Barnstead NANOpure DIamond UV ultrapure water system. All reagents and solvents were used as received.

### 6.4.2 Preparation of Ag Nanoparticle Seeds

A single large batch of Ag nanoparticle seeds was first synthesized using a procedure derived from that published by Zhang *et al.*[227] In detail, fresh stock solutions of $PVP_{(aq)}$ (8 g in 88 mL of DIW), $KOH_{(aq)}$ (28 mg in 25 mL of DIW), and $AgNO_{3(aq)}$ (17 mg in 5 mL of DIW) were first prepared. The $PVP_{(aq)}$ was transferred to a 250 mL round-bottom flask, to which 2 mL of $KOH_{(aq)}$ and 5 mL of the $AgNO_{3(aq)}$ were then added. This reaction mixture was stirred and de-gassed with nitrogen for 30 min. A fresh solution of $NaBH_4$ (19 mg in 5 mL of ice-cold DIW) was prepared and added to the reaction mixture, which was then sealed under a $N_{2(g)}$ atmosphere and allowed to react for 1 h. Finally, the mixture was aged for 48 h without stirring so that any excess $NaBH_4$ was allowed to decompose (thus ensuring that the Pt precursor could be reduced only via galvanic reaction with the Ag nanoparticle seeds).

### 6.4.3 Formation of AgPt Nanoparticles

A fresh stock solution of $H_2PtCl_6 \cdot 6H_2O$ (13 mg in 25 mL of DIW) was used in the preparation of AgPt nanoparticle samples. First, 20 mL of the previously synthesized Ag seed nanoparticles were transferred to a 50 mL round-bottom flask, followed by a predetermined volume of $H_2PtCl_6 \cdot 6H_2O_{(aq)}$ (1, 3, 5, or 8 mL). This mixture was purged of oxygen using $N_{2(g)}$ and then refluxed at 100 °C for 10 min before being allowed to cool for 24 h while still under $N_{2(g)}$ atmosphere. After cooling, the mixture was centrifuged at a relative centrifugal force (RCF) of 15,000 to remove any silver chloride or other insoluble by-products formed during the reaction.

### 6.4.4 Purification of AgPt Nanoparticles

In order to purify the final AgPt nanoparticles, each sample was first treated with four volume equivalents of acetone (laboratory grade) to induce precipitation of its constituent particles; at this point, the suspensions became visibly cloudy. Low-temperature centrifugation (3 °C, RCF = 15,000) was performed to isolate the precipitated nanoparticles, which were then re-dispersed in a minimal amount of DIW before being precipitated with acetone and centrifuged once more. The final, twice-purified product was again re-dispersed in a minimal quantity of DIW and lyophilized. The resultant yellow or brown powders were light and easily handled for further analyses; however, due to the large PVP content of the final product, further preparation was required to prepare samples for TEM measurements (see Section 6.4.6).

### 6.4.5 Preparation of Samples for ICP-OES Analysis

In preparation for ICP-OES analysis, 10 to 20 mg of each AgPt nanoparticle sample were added to a 5 mL volumetric flask and treated with 1 mL of $HNO_{3(aq)}$ to first dissolve the Ag component of the particles. The flask was then stoppered and the mixture gently stirred for 24 h. Following this treatment, the suspension took on a partially opaque, brownish colouration that was visibly darker for samples with greater Pt content (resulting from the remaining Ag-depleted nanoparticles). Next, 3 mL of $HCl_{(aq)}$ was added to the mixture to form an aqua regia solution capable of dissolving the Pt component of the particles. The flask was then loosely stoppered to prevent pressurization and the mixture allowed to stir for a further 24 h. Following this stage of treatment, the solutions had visibly cleared and taken on a yellow-orange colouration; each solution was finally diluted to a volume of 5 mL before being analyzed.

### 6.4.6 Standard Characterization Methods

Elemental analysis of the samples was conducted on a Varian Vista Pro (radial view) ICP-OES instrument. Prior to measurement, the samples were diluted using 10 % $HCl_{(aq)}$ to reduce their acid concentration. The instrument was operated with a power of 1.3 kW, a plasma flow of 15.0 $L \cdot min^{-1}$, an auxiliary flow of 1.50 $L \cdot min^{-1}$, and a read time of 10 s with three replicates for each sample.

UV-vis spectroscopy measurements were performed using a Cary 100 Bio UV–visible spectrophotometer. For each AgPt sample, a 100 μL aliquot was taken via micropipette and diluted to a total volume of 3 mL before being analyzed. A DIW blank reference was also measured and used to background-subtract each spectrum. Spectra were normalized at 320 and 600 nm to more clearly illustrate the evolution of the Ag SPR absorption peak.

Each sample was also imaged using TEM; however, the relatively large amount of PVP ligand material present in the final products proved problematic and resulted in very low contrast for the nanoparticles. In order to facilitate TEM analysis, a small portion of each AgPt sample was deposited onto carbon powder and washed thoroughly according to standard procedures.[172] In brief, several milligrams of lyophilized nanoparticle product were dispersed in a 1 mL of *n*-butylamine suspension of Vulcan XC-72 and stirred for 48 h. The samples were then successively purified (three times in total) via high-speed centrifugation in absolute ethanol (laboratory grade), with the supernatant being removed each time using a Pasteur pipet. After the final such purification, a small amount of the product dispersed in ethanol was drop-cast onto Formvar-coated copper TEM grids. After the samples dried, they were analyzed using bright field imaging on an FEI Tecnai-12 transmission electron microscope (80 kV operating voltage). Mean particle diameters were measured from TEM images using the digital image processing tool ImageJ.[199]

### 6.4.7 X-ray Spectroscopy and *Ab Initio* Calculations

XAS data acquisition was performed using the Sector 20-BM beamline of the Advanced Photon Source at Argonne National Laboratory in Argonne, IL. The lyophilized AgPt powders were analyzed in the solid state without further modification or dilution. In order to suppress thermal vibrations and enhance EXAFS signal intensity, a cryostat was used to maintain a constant sample temperature of 50 ± 1 K throughout the course of the measurements. A double-crystal Si(111) mirror monochromator was used for wavelength selection. In conjunction with a toroidal focusing mirror, the incident beam intensity was detuned to 80% to reject higher harmonics of the selected wavelength. Spectra were acquired using either a 12-element solid state Ge X-ray fluorescence detector (AgPt nanoparticles) or gas ionization chamber (metal foil references) as appropriate, given the resulting signal intensity. XAS data processing was performed using the IFEFFIT software suite.[77]

Absorption edge energies for Pt and Ag XANES spectra were calibrated relative to an in-line metal foil reference (Pt or Ag) and normalized using first- and third-order polynomials to fit the pre- and post-edge regions of the spectra, respectively. XANES simulations of Pt $L_3$-edge spectra were generated using FEFF8 software.[78] For the fitting of the experimental FT-EXAFS data, two metal-metal paths were used, with their $\sigma^2$ and $\Delta E_0$ parameters correlated in order to provide more degrees of freedom. The Pt and Ag spectra were first fitted separately in order to obtain reasonable starting values for subsequent fits; the spectra were then fitted simultaneously under identical conditions, save that the Ag–Pt and Pt–Ag bond lengths were correlated to reflect the fact that they represent a single bonding interaction. Uncertainties for the reported parameter values

were calculated from the off-diagonal elements of the correlation matrix for the final fit. These values were further weighted by the square root of the $\chi^2$ value, taking into account shot noise in the range 15 to 25 Å, as recommended by Newville *et al.*[83] Note that the Fourier-transformed regions were obtained over the available range of 2.5 to 12.5 $Å^{-1}$ and fitted only within the range of 2.2 to 3.1 Å (*i.e.*, the primary metal-metal scattering paths).

## 6.5 Results and Discussion

### 6.5.1 Initial Characterization

Concentrations of Ag and Pt in the AgPt nanoparticles were determined via ICP-OES elemental analysis performed by Daniel Chevalier of Dalhousie University. These concentrations were then used to calculate the relative atomic compositions of each sample. Mass concentrations of Ag and Pt, as well as elemental compositions corresponding to each volume of Pt solution added to Ag nanoparticle seeds, are presented in Table 6.1.

**Table 6.1.** Elemental compositions of AgPt nanoparticles as calculated from ICP-OES measurements. Adapted with permission from Reference 216.

| Pt Added / mL | Ag content / $mg \cdot L^{-1}$ | Pt content / $mg \cdot L^{-1}$ | Elemental Composition / atom% |
|---|---|---|---|
| 1 | 9.9 | 1.3 | $Ag_{93}Pt_7$ |
| 3 | 6.5 | 2.8 | $Ag_{81}Pt_{19}$ |
| 5 | 6.0 | 4.3 | $Ag_{72}Pt_{28}$ |
| 8 | 15.6 | 15.5 | $Ag_{65}Pt_{35}$ |

For convenience, AgPt samples are hereafter identified by their experimentally determined elemental compositions (*i.e.*, $Ag_{93}Pt_7$, $Ag_{81}Pt_{19}$, $Ag_{72}Pt_{28}$, and $Ag_{65}Pt_{35}$). Preferential deposition of Pt atoms onto the surfaces of the Ag seed nanoparticles was encouraged by employing a self-limiting galvanic reduction reaction during synthesis (as illustrated in Figure 6.1a). Data pertaining to average particle size and standard deviation are shown in Figure 6.1b. Mean particle diameters of 4 ± 1 nm for pure Ag nanoparticles (Ag NPs), 4 ± 1 nm for $Ag_{93}Pt_7$, 5 ± 1 nm for $Ag_{81}Pt_{19}$, 4 ± 1 nm for $Ag_{72}Pt_{28}$, and 5 ± 1 nm for $Ag_{65}Pt_{35}$ were determined.

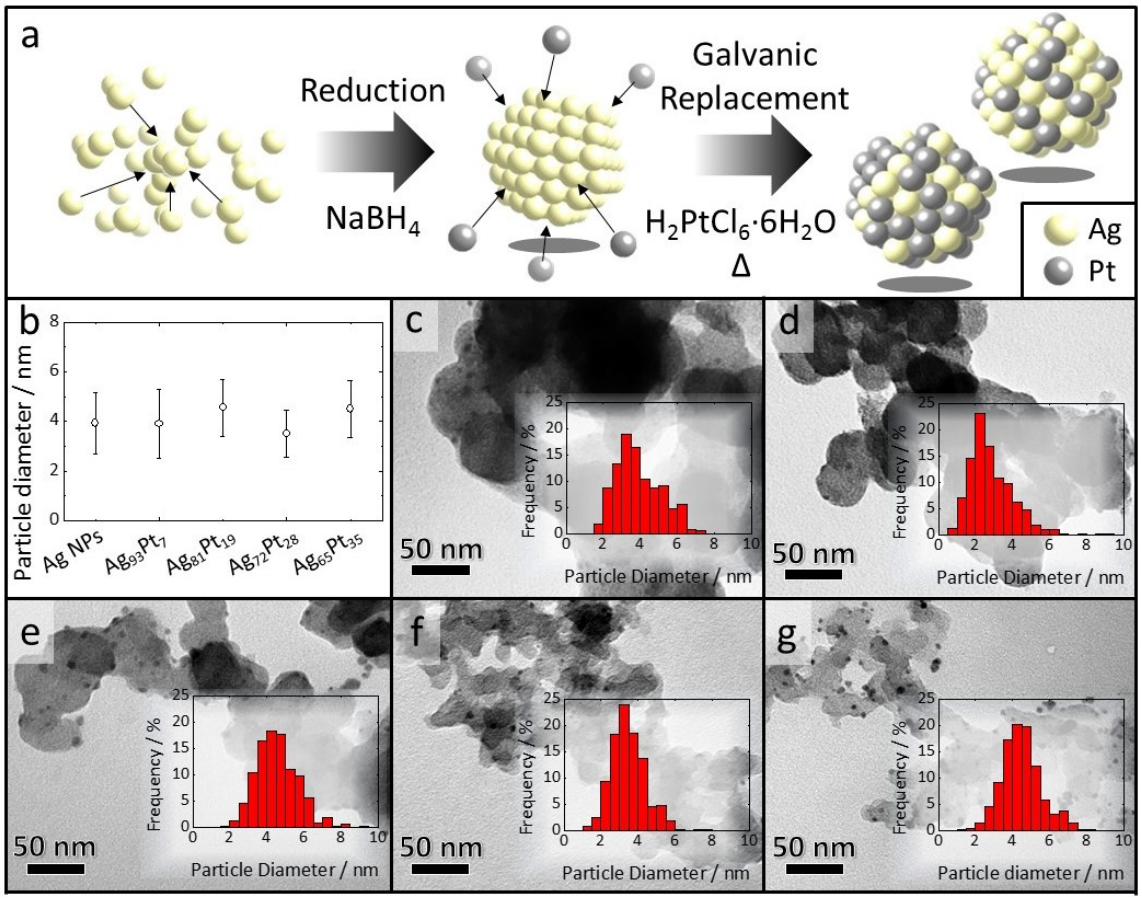


**Figure 6.1.** (a) Schematic illustration of the synthetic procedure, (b) mean particle diameters, and (c-g) TEM images depicting AgPt nanoparticles deposited onto a Vulcan XC-72 carbon powder support. Inset histograms show respective nanoparticle size distributions as determined graphically from TEM images. Adapted with permission from Reference 216.

Representative TEM images from each AgPt sample are presented in Figure 6.1c-g. The AgPt nanoparticles are observed as small (*ca.* 2 to 5 nm diameter) dark particles in the bright field images; the larger structures (*ca.* 20 nm or greater diameter) are particles of the carbon support material used to facilitate TEM data collection and improve sample stability for long-term storage. The unimodality of the particle diameter histograms supports the successful deposition of Pt onto the Ag NP surfaces, as the nucleation of discrete Pt nanoparticles should result in a bimodal distribution. From these images, the successful deposition of the nanoparticles onto the carbon support is also clearly confirmed. To further characterize the properties of these AgPt nanoparticles, UV–vis absorption spectra were acquired for each sample.

Background-corrected UV–vis absorption spectra for AgPt nanoparticle samples prior to deposition on Vulcan XC-72 are presented in Figure 6.2. An intense SPR band characteristic of nanosized Ag is prominent in the spectrum of the Ag NPs. When greater amounts of Pt were added to the Ag NPs, extinction of this SPR band was observed to occur. Experimental evidence from similar noble metal nanoparticles reveals that the peak absorption of an SPR band is dependent on the both the dielectric constant of the constituent material and particle size.[228] Given that the observed differences in mean particle diameter were not sufficient to significantly affect the SPR band[229] and that TEM imaging precludes the possibility of nanoparticle aggregation, it is concluded that the observed loss of absorption must be due to the incorporation of Pt atoms into the surfaces of Ag NPs. To further investigate this hypothesis, XAS analysis was employed to measure the resulting electronic and structural changes in the AgPt nanoparticle samples.

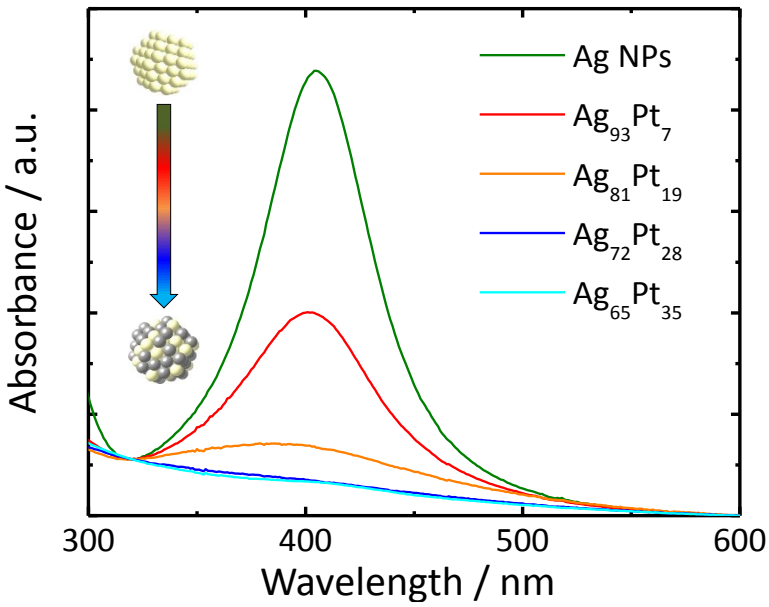


**Figure 6.2.** Background-corrected UV–vis absorption spectra of AgPt nanoparticle samples after adding increasing amounts of Pt. Reproduced with permission from Reference 216.

### 6.5.2 EXAFS Analysis

In order to characterize the structure of these bimetallic nanoparticles from both the Pt and Ag perspectives, focus was placed on element-specific EXAFS analyses. The $k^2$-weighted EXAFS spectra corresponding to the AgPt samples are presented in Figure 6.3a. It can readily be seen that the EXAFS oscillation patterns of both the Ag K-edge and Pt $L_3$-edge spectra from the AgPt nanoparticles closely resemble those of their respective metal foil references. The relatively low intensities of the Pt and Ag foil reference spectra are due to their being measured at ambient temperature (*ca.* 300 K), whereas the AgPt samples were measured at low temperatures (50 ± 1 K). Among the AgPt samples, those with greater Pt content were observed to have less-intense Ag K-edge EXAFS oscillations; this finding can be explained by destructive interference between the Ag–Ag and Ag–Pt scattering paths. Analogous amplitude reduction was also observed in the corresponding FT-EXAFS spectra between 2 and 3 Å. Conversely, analysis of Pt $L_3$-edge spectra revealed more consistent amplitudes between samples in both the EXAFS and FT-

EXAFS spectra, suggesting greater similarity in their local structural environments. Fitting of the FT-EXAFS spectra was also performed using standard methods in order to more thoroughly investigate these data.[123,172]

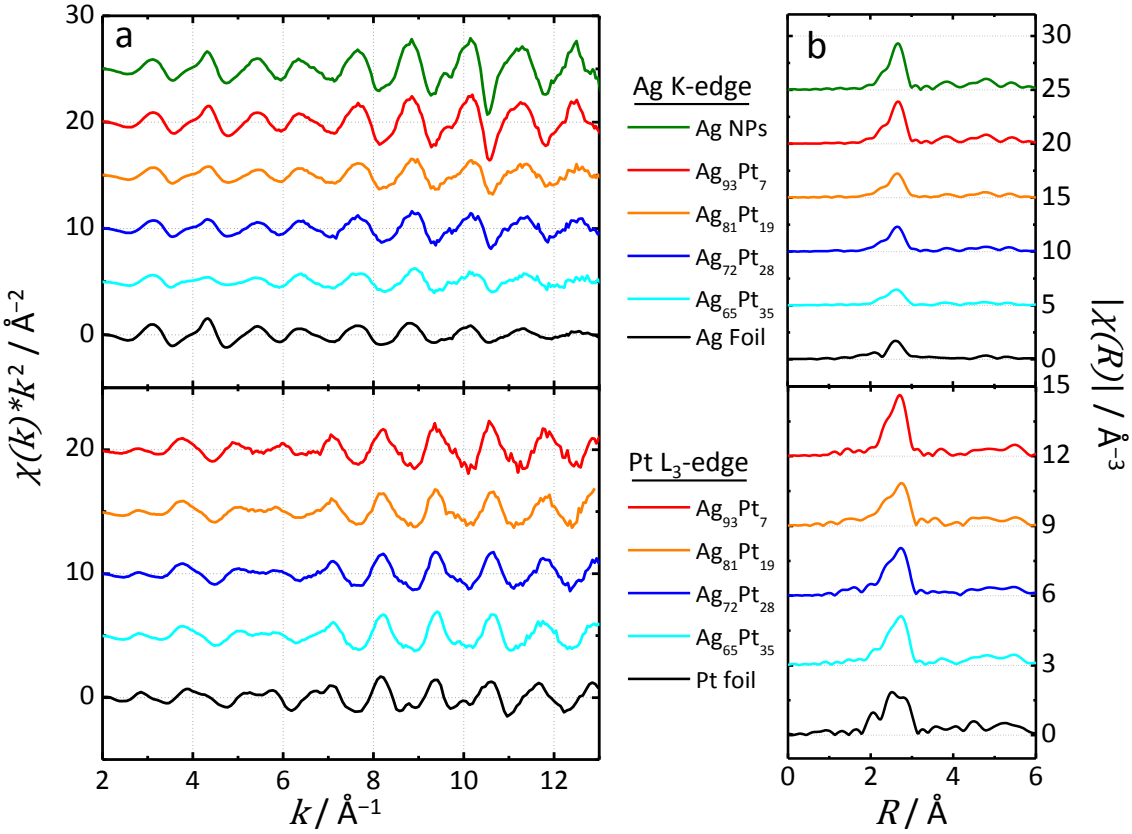


**Figure 6.3.** (a) EXAFS and (b) FT-EXAFS spectra acquired at (top) the Ag K-edge and (bottom) Pt $L_3$-edge for AgPt samples and respective metal foil references. Adapted with permission from Reference 216.

Fitted FT-EXAFS spectra are presented in Figure 6.4, with the corresponding structural parameters presented in Table 6.2. The obtained parameter values indicated a decrease in the total Ag–Ag *CN* as more Pt was incorporated into the Ag NPs; this was likely due to etching of Ag caused by the galvanic reduction of Pt. Extensive etching is expected due to the fact that four atoms of Ag must be oxidized in order to reduce a single atom of Pt (as dictated by the corresponding partial redox reaction: $Pt^{4+}_{(aq)} + 4Ag^{0}_{(s)} \rightarrow Pt^{0}_{(s)} + 4Ag^{+}_{(aq)}$). In reality, the reaction occurring is likely even more complicated due to the reductive action of PVP, which could lead to conversion of $Pt^{4+}$ species to $Pt^{2+}$ and/or

re-reduction of $Ag^{+}$ to $Ag^{0}$ at nanoparticle surfaces (thereby explaining why mean particle diameters for the AgPt nanoparticle samples did not decrease as Pt content was increased).[230,231] Significant surface roughening is also suggested by the low Ag–Ag *CN*s, particularly in the samples with the highest Pt contents. The only clear trend in terms of bond lengths was observed for the Ag–Ag scattering path, where a gradual decrease was observed as Pt content was increased. This effect is likely due to lattice contraction caused by the electronic effects of having greater quantities of Pt present in these samples. In contrast, the Pt–Pt *CN* was observed to initially increase on changing the composition from $Ag_{93}Pt_{7}$ to $Ag_{81}Pt_{19}$, but remained constant thereafter, despite continued increases in relative Pt content. While this result may at first seem unusual, it can be interpreted as indicating an increase in surface coverage by the Pt clusters rather than a continual growth in their size.

The degree of interaction between the Ag and Pt components of the nanoparticles is indicated by their respective Ag–Pt and Pt–Ag *CN*s. Based on the measured elemental compositions and mean particle diameters, a large proportion of the Ag atoms is expected exist in the particle cores where they have little to no interaction with Pt, resulting in consistently low Ag–Pt *CN*s. By contrast, the greater degree of Pt–Ag coordination observed from the Pt perspective is readily explained by a high proportion of interfacial sites due to the preferential surface localization of Pt. Taken together, and in conjunction with the SPR band extinction trend from UV-vis results, these observations provide strong evidence in support of the formation of small Pt clusters on the surface of the (albeit significantly etched) Ag nanoparticle cores.

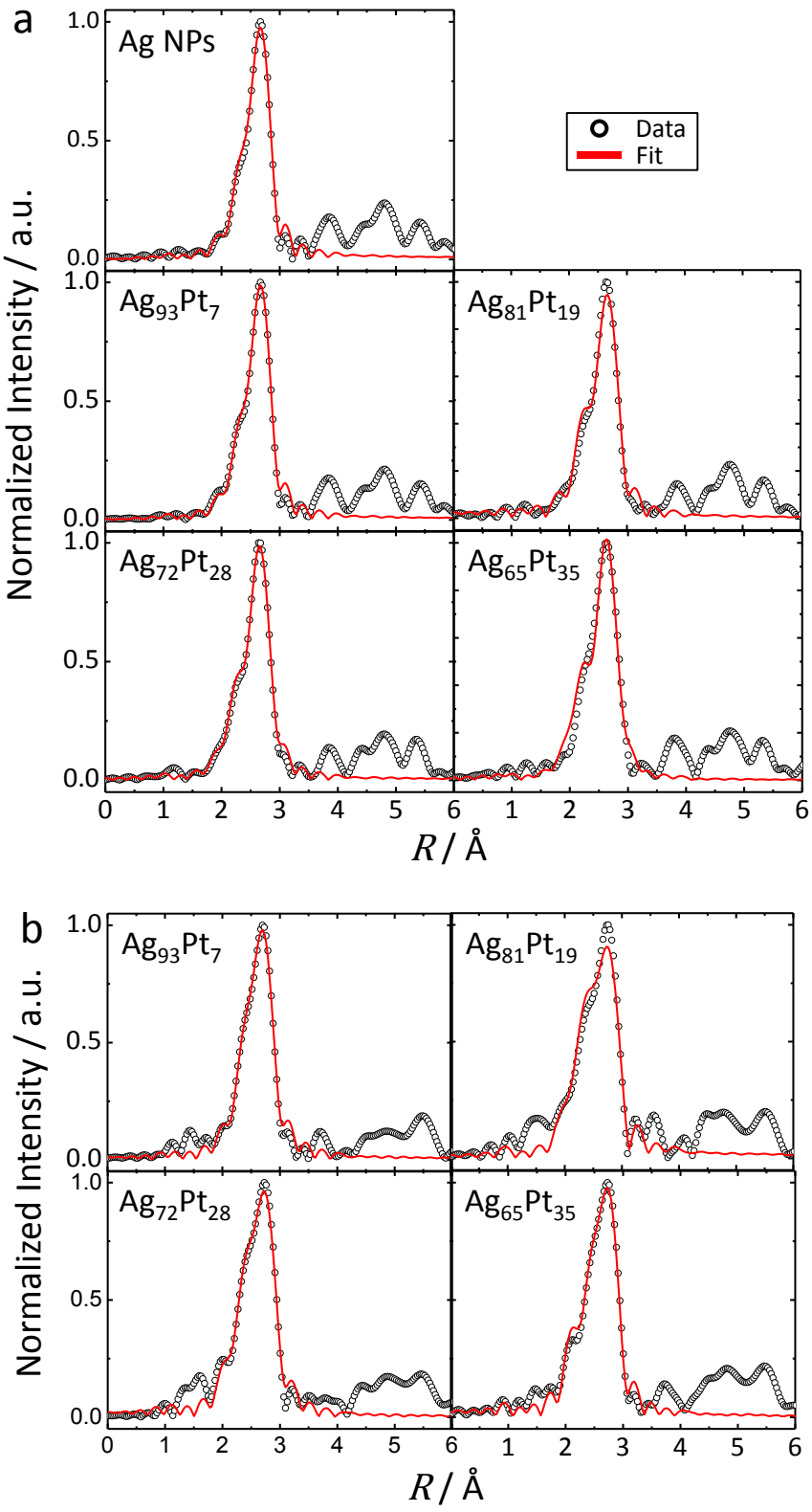


**Figure 6.4.** Experimental (empty circles) and fitted (solid red lines) FT-EXAFS spectra from AgPt nanoparticles at the (a) Ag K-edge and (b) Pt $L_3$-edge. Adapted with permission from Reference 216.

**Table 6.2.** Structural parameter values obtained from fitting Ag K-edge and Pt $L_3$-Edge FT-EXAFS spectra. Uncertainties in the last decimal place of each value are indicated in parentheses (treated as one standard deviation). An asterisk (*) indicates that these parameter values were correlated during fitting. A double asterisk (**) indicates that contributions from this scattering path were too weak to be included in the fit. Adapted with permission from Reference 216.

| Samples | Edge | Path | *CN* / a.u. | *R* / Å | $\sigma^2$ / $10^{-3}$ Å$^2$ | $\Delta E_0$ / eV |
|---|---|---|---|---|---|---|
| Ag NPs | Ag K | Ag–Ag | 9.9(8) | 2.875(3) | 2.8(4) | 2.5(7) |
| $Ag_{93}Pt_7$ | Ag K | Ag–Ag | 10.0(5) | 2.872(2) | 3.2(2) | 2.9(4) |
| | | Ag–Pt | ** | ** | ** | ** |
| | Pt $L_3$ | Pt–Pt | 2(1) | 2.77(5) | 3.1(1) | 5(2) |
| | | Pt–Ag | 6(2) | 2.84(1) | | |
| $Ag_{81}Pt_{19}$ | Ag K | Ag–Ag | 7(1) | 2.847(9) | 4.2(9) | 1(1) |
| | | Ag–Pt | 1(1) | 2.81(2)* | | |
| | Pt $L_3$ | Pt–Pt | 5(1) | 2.77(1) | 2(2) | 2(2) |
| | | Pt–Ag | 3.0(7) | 2.81(2)* | | |
| $Ag_{72}Pt_{28}$ | Ag K | Ag–Ag | 7(2) | 2.85(1) | 4(1) | 1(1) |
| | | Ag–Pt | 1(1) | 2.83(1)* | | |
| | Pt $L_3$ | Pt–Pt | 5(1) | 2.78(2) | 3(2) | 4(2 |
| | | Pt–Ag | 4(1) | 2.83(1)* | | |
| $Ag_{65}Pt_{35}$ | Ag K | Ag–Ag | 5(1) | 2.83(1) | 5(2) | –1(1) |
| | | Ag–Pt | 2(1) | 2.81(1)* | | |
| | Pt $L_3$ | Pt–Pt | 6(1) | 2.77(1) | 2(1) | 3(2) |
| | | Pt–Ag | 3.0(6) | 2.83(1)* | | |

The preference of Pt to form small clusters can be attributed to its tendency to form shorter, and therefore stronger, bonds with Pt atoms than with Ag. Island growth mechanisms are common for metal nanoparticles formed on a variety of substrate materials,[232–234] and so it can be reasonably assumed that a similar process could be at work in these AgPt nanoparticles. In order to clearly illustrated how these developing particles might look, simple Ag(111) surface model is shown in Figure 6.5a. Based on the structural information provided by these FT-EXAFS fitting results, it is proposed that small Pt clusters initially nucleate at the Ag surface, become larger as the concentration of Pt is increased, and finally continue to increase their surface density once a maximum cluster size has been reached.

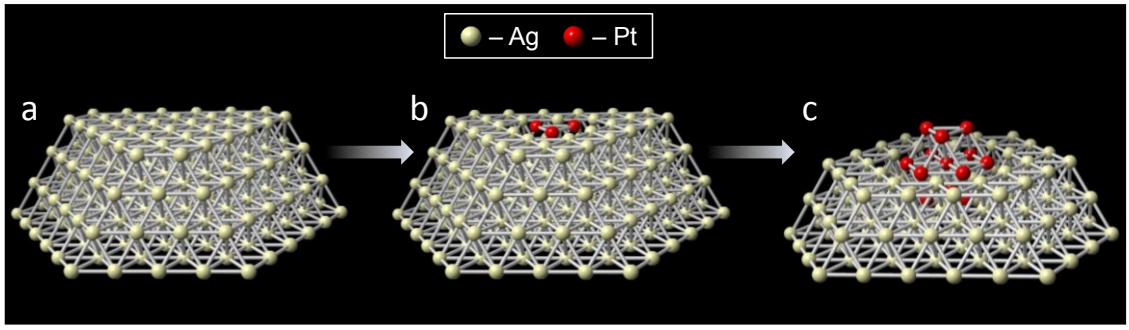


**Figure 6.5.** Proposed growth scheme for Pt clusters at the surface of Ag nanoparticle seeds. Pt ions are reduced onto (a) the initial Ag surface to form (b) very small clusters, which grow into (c) larger clusters when sufficient quantities of Pt ions are available in solution. Reproduced with permission from Reference 216.

The Pt–Pt *CN* data in Table 6.2 can also offer quantitative information on the structural evolution of the Pt clusters. The Pt–Pt *CN* of 2 for $Ag_{93}Pt_7$ suggests a triangular, three-atom $Pt_3$ cluster structure (nominal Pt–Pt *CN* = 2), as illustrated in Figure 6.5b. The other three samples ($Ag_{81}Pt_{19}$, $Ag_{72}Pt_{28}$, and $Ag_{65}Pt_{35}$) all show similar values of 5 to 6 for the Pt–Pt *CN* that roughly correspond to a $Pt_{13}$ cluster model (nominal Pt–Pt *CN* = 5.5), as shown in Figure 6.5c. Interestingly, the aforementioned samples showed no clear evidence of intermediate structures (*e.g.*, tetrahedral or planar $Pt_4$ with a Pt–Pt *CN* = 3); this finding may suggest that certain cluster structures, such as $Pt_3$ and $Pt_{13}$, may be more favorable during the Pt growth process.

It is also worth discussing how the ratio of Pt and Ag precursor materials involved in Pt reduction (*i.e.*, 1:4 for $Pt^{4+}/Ag^0$ or 1:2 for $Pt^{2+}/Ag^0$) might affect the resulting AgPt nanoparticle structure. If a $Pt^{4+}$-based reaction were dominant during the reaction, the resulting Ag–Pt particles with high Pt concentration (*e.g.*, $Ag_{72}Pt_{28}$) would be considerably smaller than the pure Ag NPs. However, mean particle diameters determined from TEM results have indicated that there is no noticeable size decrease for samples with higher Pt concentrations, suggesting that the $Pt^{2+}$ mechanism may be more favorable. This conclusion is also in good agreement with the reducing effect of PVP on

metal ion species, as discussed previously. Having thus provided good insight into the structure of these AgPt samples, further electronic characterization was sought.

### 6.5.3 XANES Analysis and Simulation

In order to probe the electronic properties of the nanoparticles, XANES spectra were acquired from the AgPt samples. These Ag K-edge spectra (Figure 6.6a) closely resembled that of the Ag foil reference, indicating their metallic structure and ruling out significant oxidation or contamination of the samples with unreduced metal salts. The general shape of the AgPt nanoparticle Pt $L_3$-edge XANES spectra (Figure 6.6b) was also observed to be very similar to that of the reference Pt foil, indicating the metallic character of Pt. Unlike the Ag K-edge, however, the white line in Pt $L_3$-edge spectra arises from the excitation of core-level p electrons to vacancies in valence d-orbitals, and so its intensity can be used to monitor the oxidation state of Pt. Interestingly, a slight decrease and broadening of the Pt white line peak were observed in the Pt $L_3$-edge spectra of AgPt samples relative to the Pt foil reference, suggesting the occurrence of charge transfer from Ag to Pt; this effect was most significant by far for $Ag_{93}Pt_7$.

The aforementioned reduced white line intensity and increased peak breadth of the $Ag_{93}Pt_7$ spectrum stand out as unusual. In order to better understand the origin of these features, FEFF8 was used to perform *ab initio* simulations of XANES spectra, which were then compared with the experimental data. Before these simulations could be performed, however, it was necessary to generate reasonable structural models to reflect the structure of Pt sites in the $Ag_{93}Pt_7$ nanoparticles. Based on *CN* and bond length parameter values obtained from FT-EXAFS data fitting, a three-atom Pt cluster on the Ag surface was selected as a representative model for the $Ag_{93}Pt_7$ sample.

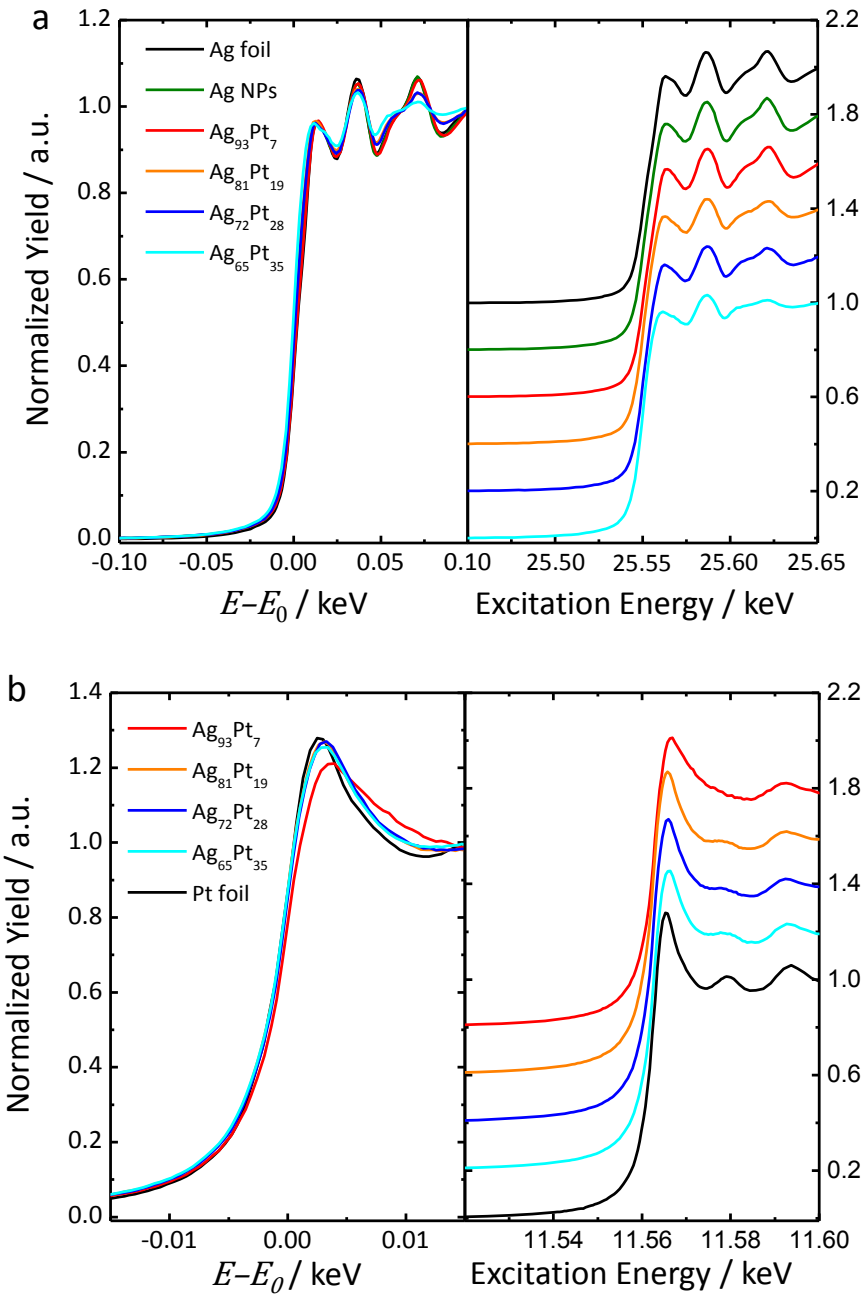


**Figure 6.6.** Overlapped (left) and stacked (right) plots of (a) Ag K-edge and (b) Pt $L_3$-edge XANES spectra from AgPt samples. Adapted with permission from Reference 216.

Experimental $Ag_{93}Pt_7$ and simulated Pt cluster spectra are presented together in Figure 6.7a. In order to verify the reliability of the simulation, a bulk Pt spectrum was also simulated and compared with experimental data from a Pt foil reference in Figure 6.7b. Comparison shows that the simulated spectrum of small Pt clusters on Ag closely

resembles that of the $Ag_{93}Pt_7$ nanoparticles. While this agreement was encouraging, it was unclear whether the observed differences relative to the Pt reference were due to the Pt–Ag bonding interaction or to the small size of the Pt clusters, alone; thus, it was necessary to determine which of the two provided a more significant contribution. The simulated spectrum of a "free" Pt cluster with no supporting Ag surface (also shown in Figure 6.7a) was markedly dissimilar to the experimentally obtained data. It was thus concluded that the interesting electronic behavior of $Ag_{93}Pt_7$ arose primarily as a result of Ag–Pt surface bonding interactions, with lesser influence due to the small size of the Pt cluster. These results also provided evidence that the selected Pt cluster model was a reasonable representation of Pt sites in the $Ag_{93}Pt_7$ nanoparticle sample.

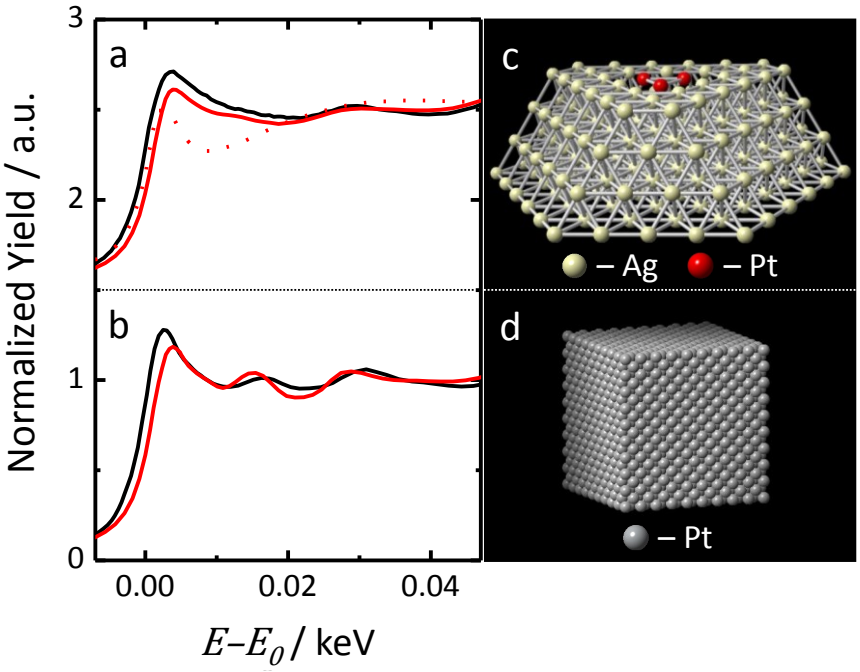


**Figure 6.7.** Experimental (black line) and simulated (red line) Pt $L_3$-edge XANES spectra for (a) a Pt cluster on an Ag surface (dotted red line: "free" Pt cluster) and (b) bulk Pt; the corresponding structural models of the (c) $Pt_3$ cluster and (d) bulk Pt are also shown for reference. Adapted with permission from Reference 216.

## 6.6 Conclusions

To summarize, a series of AgPt nanoparticles was prepared, consisting of small Pt clusters grown at the surfaces of Ag seed particles. Evidence for the incorporation of both Ag and Pt into individual particles was provided by multiple characterization techniques, including TEM, UV-vis absorption, FT-EXAFS data fitting, and analysis of experimental and simulated XANES spectra. More importantly, structural models generated using information gleaned from FT-EXAFs data fitting allowed the unusual electronic structure observed in the $Ag_{93}Pt_7$ XANES spectrum to be reproduced using *ab initio* simulated spectra, illustrating the important synergy between these techniques in the determination of local structure and electronic properties of nanomaterials. This detailed information regarding the local structure, electronic properties, and formation mechanism of AgPt nanoparticles helps to provide a better understanding the relationships between surface structure and catalytic activity in bimetallic Pt nanoparticles.

# Chapter 7 – Effects of Surface Structure on the FAO Activity of Bimetallic PtAu Nanoparticles

## 7.1 Contributions

PND synthesized PtAu nanoparticles and deposited them onto the carbon powder support. Xiaojing Zhao (College of Chemistry and Chemical Engineering, Xiamen University) and Dr. Ali Aldalbahi (King Abdullah Institute for Nanotechnology, King Saud University) acquired TEM images of the PtAu nanoparticles. PND prepared samples for ICP-OES measurements and analyzed the resulting data. Daniel Chevalier (Minerals Engineering Centre, Dalhousie University) performed ICP-OES measurements and peak fitting. Ziyou Li (School of Physics and Astronomy, University of Birmingham) performed high-angle annular dark field (HAADF) and EDS mapping experiments. Christopher Deming (University of California, Santa Cruz) performed CV and FAO activity measurements. Victor Fung (Department of Chemistry, University of California – Riverside) performed DFT calculations regarding CO binding affinities. PND performed XAS measurements and data analysis. PZ supervised PND throughout the project.

## 7.2 Foreword

The study presented in Chapter 6 demonstrated the feasibility of preparing bimetallic Pt nanoparticles with surface-localized Pt sites. Structural analysis revealed that the surfaces of some of these nanoparticles consisted of small Pt clusters with extensive Ag regions accessible to the acidic electrolyte. This exposed Ag surface area is believed to have been responsible for the instability of the AgPt nanoparticles under typical electrocatalytic conditions (*i.e.*, acidic electrolyte and oxidizing applied

potentials[56,57]). To address this stability issue, a modified OAm method (resembling those used in Chapters 4 and 5) was developed in order to obtain a more electrochemically stable core structure. Although the use of Au (rather than less expensive metals) does little to reduce the cost of such nanoparticles, the resulting bimetallic Pt nanoparticles can be used as a foundational study for future experiments studying different combination of metal and/or different catalytic reactions. While analysis of PtAu nanoparticles using XAS is greatly complicated by the overlap of Pt and Au $L_3$-absorption edges, a practical technique for minimizing this effect was employed in this study. Overall, emphasis was placed on the synthesis of PtAu nanoparticles with stable metallic Pt surfaces, evaluating their electrocatalytic activity, and using structural characterization techniques (such as XAS) and DFT calculations to closely investigate the relationship between observed structure and catalytic activity.

## 7.3 Introduction

Despite the electrochemical instability of the AgPt nanoparticles described in Chapter 6, few-atom surface clusters of catalytically active metals are a promising subject of research.[17,54,118] These few-atom catalytic sites are often supported on carbon-based or metal oxide materials, but have also been prepared on the surfaces of metal nanoparticles.[188,235] While it might seem intuitive that the sub-monolayer coverage of the core material by the catalytically active element should result in diminished catalytic activity, excellent performance is often observed for these materials.[19] Furthermore, high atom economy can be achieved using these few-atom surface sites, due to the fact that (in contrast with larger and/or monometallic nanoparticle catalysts) virtually all of the

catalytically active atoms are located at accessible sites.[236]

The observed enhancement in catalytic activity also seems to be dependent on the nature of bonding interactions between the active atomic site and support material.[236] For some catalysts, the support serves as a co-catalyst by providing binding sites for molecules involved in the catalytic reaction.[237] In other cases, the primary role of the support seems to be stabilizing and maintaining separation between the few-atomic sites.[238] However, given the relatively recent arrival of few-atom catalysts on the research scene, it is often still unclear exactly what role the support plays for a given material.[236]

Herein, it is undertaken to synthesize and characterize a series of PtAu nanoparticles, in an effort to generate catalytically active few-atom Pt sites for use in the FAO reaction. The use of bottom-up colloidal synthetic methods allows for great control over the structure of the resulting nanoparticles and affords good uniformity in terms of particle size and morphology. The XAS techniques developed in preceding chapters are ideally suited for characterization of these nanoparticles, and are used to great effect. Electrochemical measurements, including CV and FAO reaction activity are also used to both study the surface structure of the nanoparticles and gauge their electrocatalytic performance. By analyzing PtAu nanoparticles with a variety of surface structures, the effects of core-shell, sub-monolayer, and few-atom sites on catalytic activity is explored.

## 7.4 Experimental Methods

### 7.4.1 Materials

Dihydrogen hexachloroplatinate ($H_2PtCl_6 \cdot 6H_2O$, 99.9 %), hydrogen tetrachloroaurate ($HAuCl_4 \cdot 3H_2O$, 99.9 %), ethylene glycol (EG, 99+ %), and HiSPEC

3000 carbon-supported Pt catalyst (Pt/C, ≤ 500 ppm impurities) were purchased from Alfa Aesar. Oleylamine (OAm, C18-content 80-90 %) and formic acid (HCOOH, 99 %) were purchased from Acros Organics. Vulcan XC-72 carbon powder was purchased from Cabot. Nafion® 117 Solution (Nafion, 5 %) and *n*-butylamine ($BuNH_2$, 99.5 %) were purchased from Sigma Aldrich. Perchloric acid ($HClO_4$, 70 %) was purchased from Fisher Scientific. Ethanol used in cyclic voltammetry experiments (EtOH, 96 %) was purchased from J.T. Baker. All reagents and solvents were used as received, without further purification.

### 7.4.2 Synthesis of PtAu Nanoparticles

Bimetallic PtAu nanoparticles were prepared using a modified version of the synthesis described in Section 4.4.2, and based originally upon the procedure employed by Chen *et al.*[189] This synthetic process differed from the original method in that the CO reducing agent/co-ligand was replaced with ethylene glycol (EG). In addition to removing the need for pressurized gases during synthesis, this modification was important because poisoning of Pt surfaces by CO is a major cause of activity loss in the catalytic FAO reaction.[37,118] As a result, it could be reasonably assumed that the as-prepared Pt-based nanoparticles obtained using this method were at least initially free from CO-poisoning.

PtAu nanoparticles were prepared from stock solutions of Pt and Au chloride precursor salts, with nominal compositions of 10, 25, 50, and 75 atom% Pt being selected by controlling the ratio of precursors used. In a typical synthesis, 72.5 mg $H_2PtCl_6 \cdot 6H_2O$ and 55.1 mg $HAuCl_4 \cdot 3H_2O$ were each dissolved in 70 mL of OAm through a combination of ultrasonication and manual mixing to obtain metal precursor stock solutions. Appropriate volumes of these Pt and Au stock solutions (prepared in OAm)

were then added to a 100 mL round-bottom flask to give the desired Pt-to-Au ratio with a total volume of 20 mL. An additional 20 mL of EG was then added while mixing vigorously using a magnetic stirrer. The resulting mixture was subsequently bubbled with $N_{2(g)}$ for several minutes in order to remove dissolved $O_{2(g)}$ from solution. Each mixture was then placed in a 180 ºC oil bath, sealed, and allowed to react for 1 h. Once the reaction was complete, flask was removed from heat and allowed to cool to room temperature while still sealed under a $N_{2(g)}$ atmosphere. Due to the large excess of reducing agents employed in this reaction (OAm and EG, also functioning as solvents), all $Pt^{4+}$ and $Au^{3+}$ species can reasonably be assumed to have been reduced to a zero-valent state.

In order to purify the product nanoparticles, each sample was divided amongst several 30 mL polypropylene centrifuge tubes. The nanoparticles were precipitated via addition of two to three volume equivalents of EtOH, and then isolated by centrifuging the resulting suspension (at 6,000 RPM for 5 min) and decanting the supernatant. The precipitated nanoparticles were then redispersed in hexanes via brief ultrasonication and shaking before being again precipitated and centrifuged. After this second centrifugation cycle, the purified nanoparticles were redispersed in hexanes and centrifuged once more to remove any insoluble material.

### 7.4.3 Deposition of PtAu Nanoparticles onto XC-72 Carbon Powder

Following purification, the nanoparticle samples were deposited onto an XC-72 carbon powder support material via ligand exchange-induced destabilization. A nanoparticle loading of 20 wt% (by total mass of Pt and Au) was selected in order to allow for better comparison with the commercial Pt/C catalyst (HiSPEC 3000, 20 wt% Pt)

used as a reference material for electrocatalytic testing. For each sample, four mass equivalents of XC-72 powder (assuming a theoretical yield of 100 % for each nanoparticle sample) were added to 15 mL of $BuNH_2$ and thoroughly dispersed via ultrasonication. Each purified nanoparticle sample was then precipitated using EtOH and isolated via centrifugation and decantation. The isolated nanoparticle material was redispersed and extracted from the centrifuge tube using ultrasonication and successive aliquots of the previously prepared XC-72/$BuNH_2$ suspension. This final mixture was then allowed to stir magnetically for 24 h in order to allow the ligand exchange and nanoparticle deposition to occur gradually. Finally, the post-deposition PtAu nanoparticle materials were isolated once more via EtOH addition and centrifugation (at 12,000 RPM for 20 min) and allowed to dry in air.

### 7.4.4 Transmission Electron Microscopy

Bright field TEM imaging of the samples was performed both prior to and following deposition onto the XC-72 carbon support. In preparation for analysis, each sample was dispersed in *ca.* 200 μL of ethanol via sonication and drop-cast onto Formvar-coated copper TEM grids. Unsupported PtAu nanoparticle samples were imaged by Dr. Ali Aldalbahi at King Saud University using a JEOL JEM-2100F transmission electron microscope operated at a 200 kV accelerating voltage. PtAu nanoparticle samples supported on XC-72 carbon powder were imaged at Xiamen University by Xiaojing Zhao using a Tecnai F-30 transmission electron microscope operated at a 300 kV accelerating voltage. Size distributions and mean particle diameters of the nanoparticles were measured and calculated at Dalhousie University using MacBiophotonics ImageJ software[199] using several representative images from each sample. HAADF and EDS

mapping measurements were performed by Dr. Ziyou Li and Prof. Jun Yuan at the University of Birmingham using a JEOL 2100F scanning transmission electron microscope. A JEOL annular dark field detector was used for HAADF imaging and a Bruker XFlash 4030 silicon drift detector was used for EDS mapping of the PtAu nanoparticle samples.

### 7.4.5 X-ray Absorption Spectroscopy

XAS measurements were performed using the Sector 20-BM beamline of the Advanced Photon Source at Argonne National Laboratory in Argonne, IL. The end-station was equipped with a double-crystal Si(111) monochromator for wavelength selection, which was detuned to 80 % in order to help reject higher harmonics of the desired energy; a toroidal focusing mirror was also employed to further enhance harmonic rejection. Gas-ionization detectors were used to measure the absorption spectra of Pt and Au foil reference materials; however, data acquisition from the bimetallic nanoparticles was complicated by overlap between the spectra obtained at the Pt and Au $L_3$-edges (occurring at 11,562.76 eV and 11,919.70 eV, respectively[239]). This challenge was addressed by employing a 12-element Ge fluorescence detector to collect data from the bimetallic PtAu nanoparticles. Although there also exists overlap between the Pt and Au $L_\alpha$ emission peaks centered at 9,442.3 eV and 9,713.3 eV, repectively[240]), nearly all of the interfering signal could be filtered out by excluding the overlapping energy region between the two. While excluding this region also resulted in a reduction of fluorescence intensity, the loss was largely offset by the greater sensitivity of the fluorescence detector relative to standard absorption detectors. As a result, useable spectra were obtained for all samples through the use of this method.

In order to compensate for the greater amount of noise present in the fluorescence data, PtAu nanoparticle samples were held at 90 ± 1 K during measurement in order to enhance EXAFS signal intensity by supressing thermal vibrations in the material. Data processing and fitting were performed using WinXAS[76] and Analyzer v0.1 (see Section 2.1.6) software. A single metal-metal scattering path was used in fitting the FT-EXAFS data because insufficient degrees of freedom were available to include separate Pt and Au scattering paths; the Pt–M and Au–M fitting values reported herein thus represent averages of the Pt–Pt/Pt–Au and Au–Au/Au–Pt contributions.

### 7.4.6 Cyclic Voltammetry

Cyclic voltammetry was performed by Christopher Deming at the University of California in Santa Cruz, California. A CHI 710 electrochemical work station with a three-electrode setup was employed, including a polished glassy carbon RDE working electrode, a Ag/AgCl reference electrode, and a Pt sheet counter electrode. A solution of 0.1 M perchloric acid was used as the supporting electrolyte, with the addition of 0.1 M formic acid during FAO activity measurements. Catalyst "ink" suspensions were prepared by dispersing the carbon-supported PtAu material in EtOH via ultrasonication to obtain a final catalyst concentration of 1 $\mu g \cdot \mu L^{-1}$. A volume of Nafion solution equal to 1 % the volume of added EtOH was then added and sonicated for a further 15 min to complete the preparation.

Catalyst inks were deposited onto polished RDE surfaces using a microliter syringe. For ORR testing, 20 μL of catalyst ink were drop-cast onto the electrode surface and allowed to dry completely. A 3 μL volume of diluted Nafion solution (20 % v/v in EtOH) was then deposited onto the dried catalyst layer in order to help improve its physical stability and electrical conductivity. The electrode surface was allowed to dry

completely prior to electrochemical testing. After purging the electrolyte solution with ultrahigh purity $N_{2(g)}$, CV measurements were performed. Pt ECSAs were calculated from the integrated region beneath the H-desorption peaks in each voltammogram.

### 7.4.7 DFT Calculations

DFT calculations were performed by Victor Fung at University of California, Riverside, using Vienna *ab initio* package (VASP) software. The revised Perdew-Burke-Erzerhof (RPBE) form of the generalized-gradient approximation (GGA) was chosen for electron exchange and correlation in order to correct for the over-binding of small molecules at transition metal surfaces observed using the standard Perdew-Burke-Erzerhof approach. The electron-core interaction was described using the projector-augmented wave method (PAW). A kinetic energy cutoff of 450 eV was used for the planewaves, and the Brillouin zone was sampled using a 3×3×1 Monkhorst-Pack scheme. The surface model slab was created using a 4x4 supercell of the Pt/Au unit cell, with four atomic layers and a 15 Å unit cell. Adsorption energies were calculated using the following equation:

$$E_{ads} = E_{surface+adsorbate} - (E_{surface} + E_{adsorbate}), \quad (6.1)$$

wherein the energy of the adsorbate, $E_{adsorbate}$, was computed by placing the CO adsorbate molecule in a 10 Å wide cubic cell vacuum to prevent intermolecular interactions resulting from the periodic boundary conditions.

## 7.5 Results and Discussion

### 7.5.1 Initial Characterization of PtAu Nanoparticles

Initial characterization of the carbon-supported PtAu nanoparticles was performed

using ICP-OES and TEM in order to measure their elemental compositions and confirm successful sample preparation (see Table 7.1). The results of elemental analysis showed good agreement between the ideal and measured compositions, and samples are hereafter identified by their measured Pt content: $Pt_{78}Au_{22}$, $Pt_{53}Au_{47}$, $Pt_{17}Au_{83}$, and $Pt_{7}Au_{93}$. Total metal loadings for these samples were very similar (11 ± 2 wt%), but consistently less than the target 20 wt%. TEM measurements performed following deposition onto XC-72 carbon powder (Figure 7.1) revealed a high degree of nanoparticle uniformity, with observed mean particle diameters of *ca.* 7 nm for all samples and a high degree of dispersion on the carbon powder support.

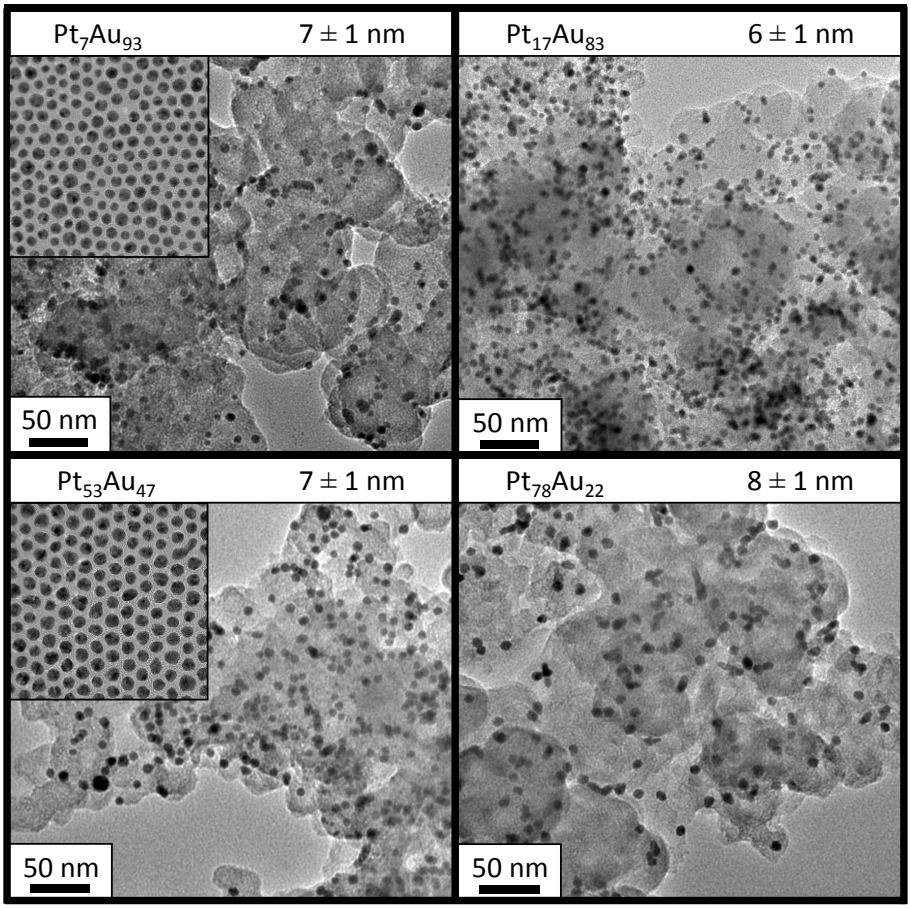


**Figure 7.1.** TEM micrographs and mean particle diameters from carbon-supported PtAu nanoparticles. Inset images show unsupported PtAu nanoparticles. One standard deviation from the mean diameter is indicated by the number following the plus-minus symbol.

**Table 7.1.** Elemental compositions and mass loadings calculated from ICP-OES measurements of PtAu nanocatalysts, and mean particle diameters determined graphically from TEM images.

| Ideal Composition / atom % | Measured Composition / atom % | Metal Loading / mass % | Pt Loading / mass % | Mean Particle Diameter / nm |
|---|---|---|---|---|
| $Pt_{75}Au_{25}$ | $Pt_{78}Au_{22}$ | 13 | 10.1 | 8 ± 1 |
| $Pt_{50}Au_{50}$ | $Pt_{53}Au_{47}$ | 12 | 6.4 | 7 ± 1 |
| $Pt_{25}Au_{75}$ | $Pt_{17}Au_{83}$ | 10 | 1.7 | 6 ± 1 |
| $Pt_{10}Au_{90}$ | $Pt_{7}Au_{93}$ | 11 | 0.8 | 7 ± 1 |

HAADF imaging and EDS mapping were employed in order to provide insight into the local structure of these PtAu nanoparticles. By rastering the electron beam across an individual nanoparticle and measuring the observed Pt and Au X-ray fluorescence intensities, it was possible to map their spatial distribution. The individual dots represent the fluorescence intensity for Pt or Au in that pixel of the image: greater intensity is reflected by a brighter colouration, and is not directly representative of Pt cluster size. This analysis revealed a distinct Au core/Pt shell structure for all samples, with further evidence of Pt sub-monolayer and few-atom cluster surface coverage in those samples with low Pt content (*i.e.*, $Pt_7Au_{93}$). Support for this finding is afforded by the single-particle EDS mapping (Figure 7.2a-b), in which the Pt signal of $Pt_7Au_{93}$ is much more highly dispersed than that of the $Pt_{78}Au_{22}$ sample. While these results are encouraging, more quantitative evidence of these sub-monolayer and few-atom cluster surface structures is made available by FT-EXAFS analyses.

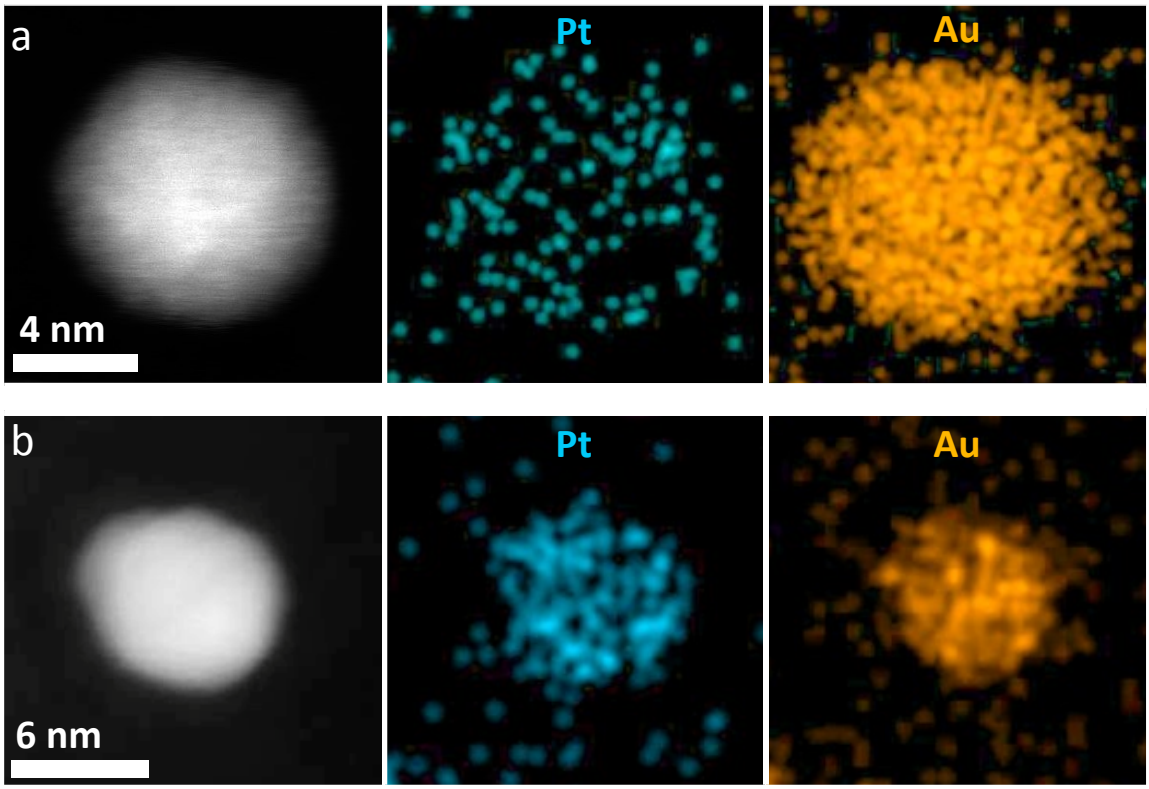


**Figure 7.2.** HAADF images and EDS elemental maps of Pt and Au for (a) few-atom clusters in $Pt_7Au_{93}$ nanoparticles and (b) complete core-shell structure in $Pt_{78}Au_{22}$ nanoparticles.

### 7.5.2 EXAFS Fitting Results

FT-EXAFS spectra for $Pt_7Au_{93}$ are presented alongside reference spectra from pure Pt and Au nanoparticles in Figure 7.3. From these plots, a marked difference in peak intensities was observed between the Pt and Au $L_3$-edge spectra of $Pt_7Au_{93}$, with the low intensity of the Pt peak being indicative of a low *CN*. Parameter values (shown in Table 7.2) obtained by fitting the Pt $L_3$-edge FT-EXAFS spectra shown in Figure 7.4 confirmed that Pt was significantly under-coordinated (Pt–M *CN* = 7.4, versus Au–M *CN* = 12), indicating a strong preference for the surface-localization of Pt over Au. It is remarkable that these complex surface morphologies were achieved via simultaneous reduction of the two metals, whereas similar control over surface structure generally requires a stepwise synthesis.[54]

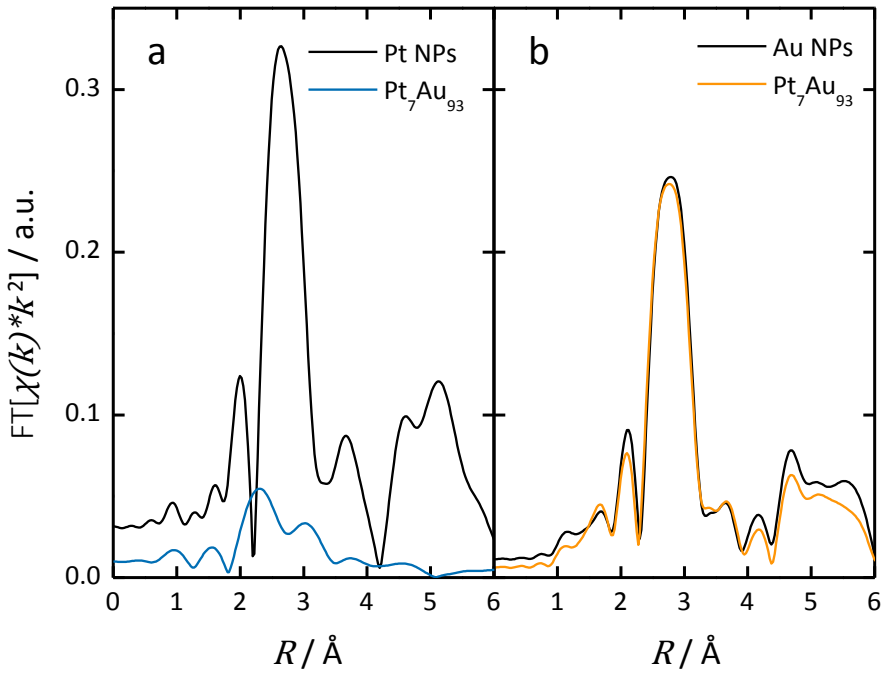


**Figure 7.3.** (a) Pt and (b) Au $L_3$-edge FT-EXAFS spectra of few-atom $Pt_7Au_{93}$ compared against pure Au or Pt nanoparticle reference samples.

From the Au perspective, the majority of Au–M bond lengths was observed to gradually switch from Au–Au to Au–Pt with increasing Pt content. This shift reflects greater degrees of Pt incorporation into the nanoparticles, but does not provide direct support for the formation of a core-shell nanoparticle structure. Based on the Pt–M bond lengths determined from FT-EXAFS fitting, homometallic bonding between Pt atoms was found to be greatly predominant in both $Pt_{53}Au_{47}$ and $Pt_{78}Au_{22}$ nanoparticles. The close agreement of the measured Pt–M bond lengths in $Pt_7Au_{93}$ and $Pt_{17}Au_{83}$ with that expected for Pt–Au (*i.e.,* 2.822 Å), however, reveals that Au atoms comprise the majority of atoms neighbouring Pt. This finding is consistent with the presence of few-atom Pt clusters at the surfaces of predominantly Au nanoparticles.

**Table 7.2.** Comparison of coordination number, bond length, and degree of heterometallic bonding for PtAu nanoparticles, as obtained via FT-EXAFS fitting. Uncertainties in the last decimal place of each value are indicated in parentheses (treated as one standard deviation).

| Sample | Au–M | | | Pt–M | | |
|---|---|---|---|---|---|---|
| | *CN* / a.u. | *R* / Å | Au–Pt / % | *CN* / a.u. | *R* / Å | Pt–Au / % |
| $Pt_{100}Au_0$ | ----- | ----- | ----- | 11.1(5) | 2.772(1) | ----- |
| $Pt_{78}Au_{22}$ | 12(1) | 2.839(4) | 66 | 9(1) | 2.776(4) | 8 |
| $Pt_{53}Au_{47}$ | 12.1(9) | 2.851(3) | 42 | 9(2) | 2.776(8) | 8 |
| $Pt_{17}Au_{83}$ | 11.6(9) | 2.861(3) | 22 | 9(1) | 2.818(5) | 92 |
| $Pt_7Au_{93}$ | 12(1) | 2.862(4) | 20 | 7.4(9) | 2.813(5) | 82 |
| $Pt_0Au_{100}$ | 12.0(4) | 2.872(1) | ----- | ----- | ----- | ----- |

*CN* values obtained from FT-EXAFS fitting provide additional support in favour of the surface localization of Pt. The observed Au–M *CN*s of all PtAu samples are rather high for nanoparticles of their size (as determined from TEM images), whereas the Pt–M *CN*s are more reasonable, if not lower than expected. Furthermore, the combination of extensive Pt–Pt bonding and higher Pt–M *CN*s in $Pt_{53}Au_{47}$ and $Pt_{78}Au_{22}$ suggests that thicker Pt shells are formed in these samples than in those containing less Pt. Based on the information obtained from the various characterization techniques employed, heretofore, it is possible to construct hypothetical particle structures for some of the PtAu nanoparticles.

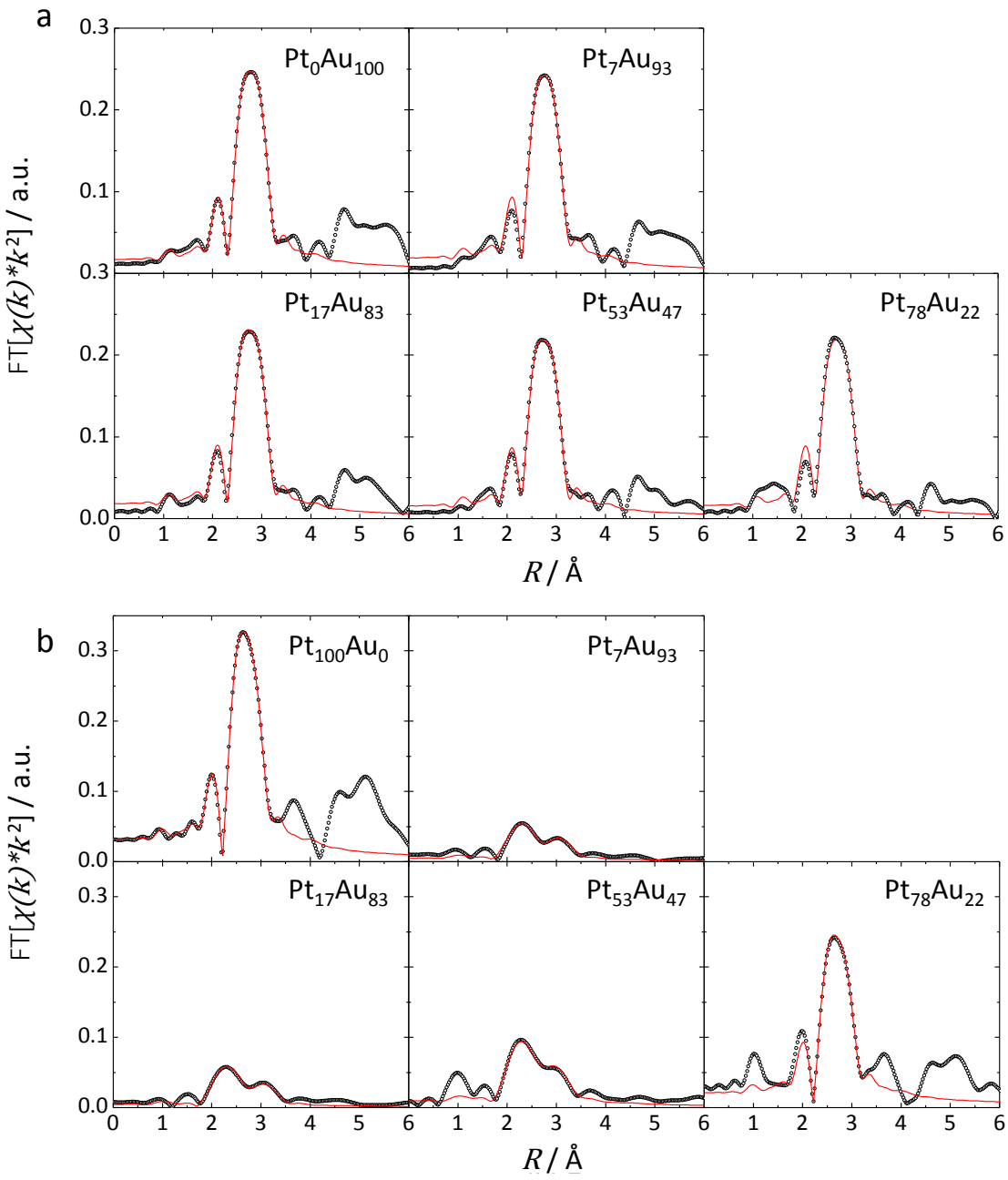


**Figure 7.4.** Experimental (hollow circles) and fitted (red lines) FT-EXAFS spectra acquired at the (a) Au and (b) Pt $L_3$-edges of PtAu nanoparticle samples.

Examples of few-atom Pt cluster and core-shell surface structures are illustrated in Figure 7.5a-b. Strong support for these distinct surface structures is provided by the respective Pt–H, Pt–O, and Au–O formation and removal peaks revealed by CV measurements in Figure 7.5c. As might be intuited, spectra from samples with lower Pt

content (*i.e.*, $Pt_7Au_{93}$ and $Pt_{17}Au_{83}$) exhibited less-intense Pt–H and Pt–O peaks and significant Au–O peaks, whereas samples with higher Pt content (*i.e.*, $Pt_{52}Au_{47}$ and $Pt_{78}Au_{22}$) featured more intense Pt–H/Pt–O peaks and little to no Au–O intensity. Interestingly, though, the position of the Pt–O removal peak in the reverse potential sweep was observed to shift gradually from *ca.* 0.8 $V_{RHE}$ for pure Pt to *ca.* 0.7 $V_{RHE}$ as a function of decreased Pt content; this shift represents an increased binding affinity of Pt for O atoms, and could reflect significant changes in the catalytic behaviour of these samples.

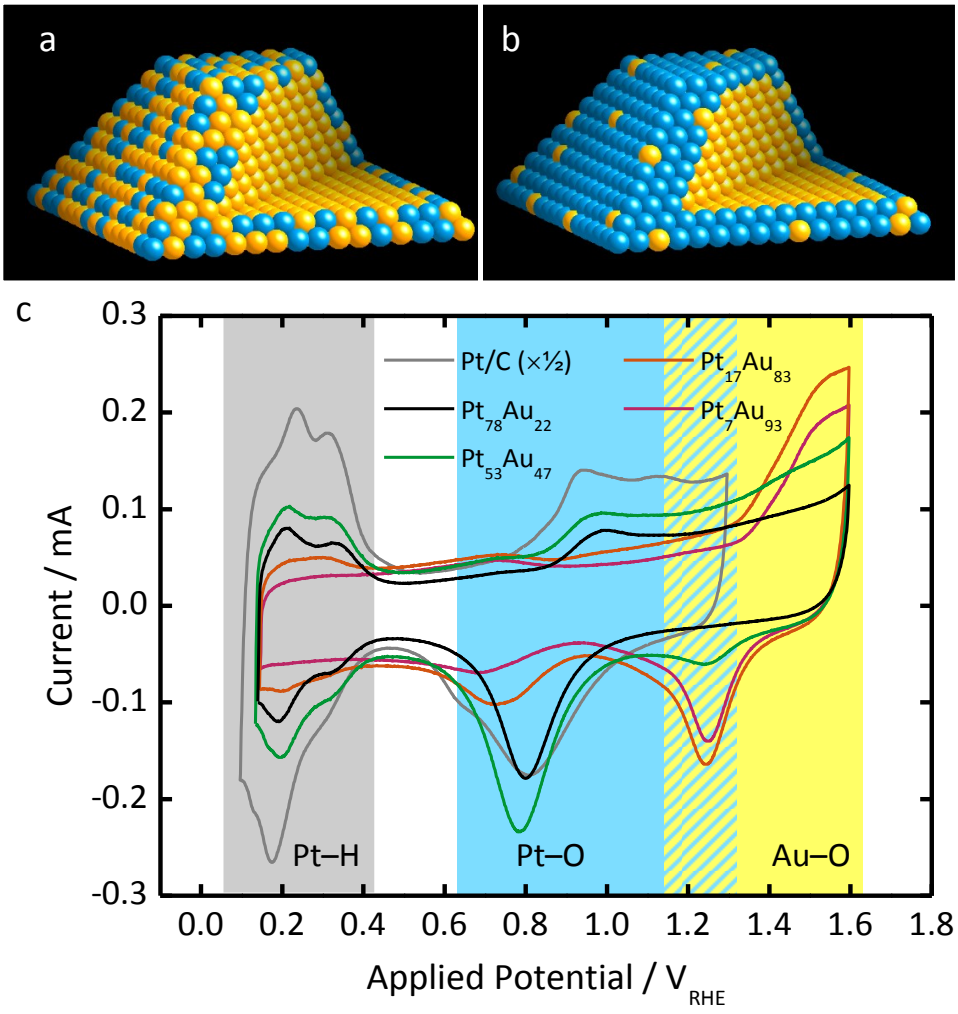


**Figure 7.5.** Models depicting examples of (a) few-atom Pt and (b) core-shell PtAu surface structures at the partial surface of a polyhedral nanoparticle, and (c) cyclic voltammograms with highlighted regions of interest for PtAu samples in 0.1 M $HClO_4$ and 0.1 M HCOOH (sweep rate: 100 $mV \cdot s^{-1}$).

The FAO electrocatalytic activities of the PtAu samples were normalized according to their respective Pt masses and compared with a commercial Pt/C reference material. The effect of CO poisoning on Pt surfaces is immediately evident from the FAO peak currents (*ca.* 0.6 $V_{RHE}$) in the forward potential sweeps of Pt/C, $Pt_{78}Au_{22}$, and $Pt_{53}Au_{47}$ shown in Figure 7.6a. The much greater peak intensities observed for samples bearing few-atom and sub-monolayer Pt sites (*i.e.*, $Pt_7Au_{93}$ and $Pt_{17}Au_{83}$), however, indicate that CO poisoning was being largely averted. This increased FAO peak intensity was also correlated with the disappearance of the CO oxidation peak at *ca.* 0.9 $V_{RHE}$, and is more clearly illustrated by the highlighted peak at *ca.* 0.85 $V_{RHE}$ in the first derivative of the forward sweep (Figure 7.6b). CO oxidation also occurs on Au surfaces at 0.8 to 0.9 $V_{RHE}$,[241] therefore the absence of a peak in this region of the forward FAO sweeps of $Pt_{17}Au_{83}$ and $Pt_7Au_{93}$ indicates that no CO oxidation is occurring at either Pt or Au. Furthermore, while Au surfaces are resistant to CO poisoning and can serve to catalyze the FAO reaction, they are much less active than Pt surfaces.[242] Peak FAO activity is achieved at *ca.* 0.6 $V_{SCE}$ (0.9 $V_{RHE}$) on Au surfaces,[242] and the fact that no such peak is observed in the voltammograms shown in Figure 7.6 indicates that Pt sites are responsible for the majority of the observed FAO activity.

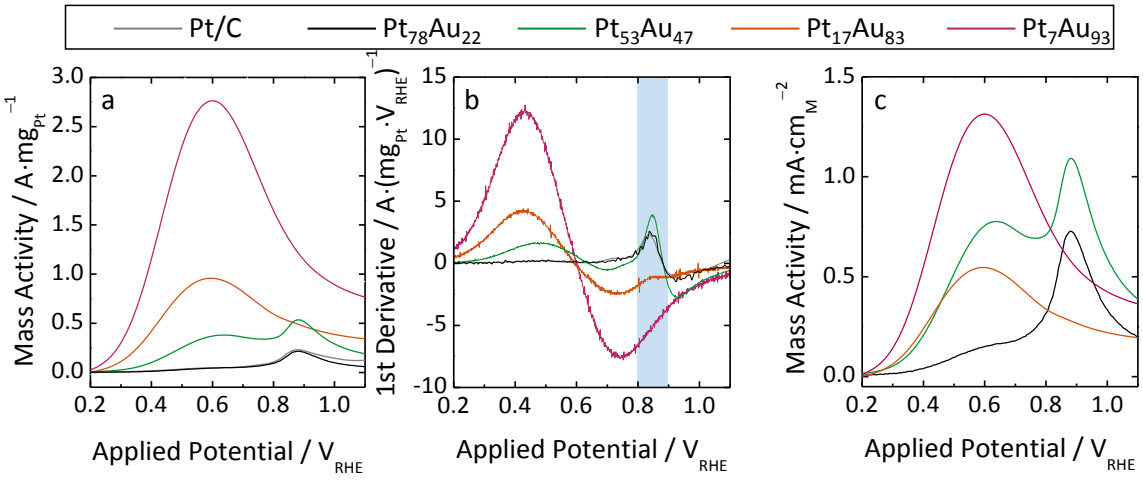


**Figure 7.6.** (a) Mass-normalized forward sweep and (b) first-derivative voltammograms, as well as (c) total ECSA-normalized forward sweep voltammograms corresponding to the PtAu nanoparticle and Pt/C reference samples in 0.1 M $HClO_4$ and 0.1 M HCOOH (sweep rate: 10 $mV \cdot s^{-1}$).

As these results demonstrate, eliminating CO poisoning at the Pt surface sites had a profound effect on the peak FAO current and led to increases in electrocatalytic performance by nearly two orders of magnitude, depending on the nature of the Pt surface sites involved. A clear trend was observed for the peak FAO currents presented in Figure 7.7a, with the few-atom Pt sites of $Pt_7Au_{93}$ demonstrating activity much greater than that of pure Pt surfaces (*i.e.*, 66 times the current per unit mass of Pt/C and 92 times that of $Pt_{78}Au_{22}$). It is also important to note that the observed activity enhancement is not an artefact of normalizing only by the mass of Pt; Figure 7.6c illustrates that significant activity enhancement is also observed when the activity is normalized by the total ECSA (*i.e.*, the sum of Pt and Au ECSAs).

Despite this great enhancement, chronoamperometry measurements indicated that there was still a significant loss of activity over time when the samples were held at constant potential (Figure 7.7b). As discussed previously, CO poisoning in these samples has been virtually eliminated, and so cannot be the source of this gradual loss of activity; a more likely explanation is the gradual accumulation of electrosorbed electrolyte ions and reactants/intermediates at the electrode surface.[46] This hypothesis is supported by the observation that much of this loss is recoverable, as indicated by the retention of 70% maximum peak current by $Pt_7Au_{93}$ after 1,500 rounds of CV potential cycling (Figure 7.7c). The irreversible losses brought about by this repeated cycling treatment can be ascribed to rearrangement of surface atoms, which can smooth or restructure defected surfaces, thereby resulting in reduced catalytic activity.[243]

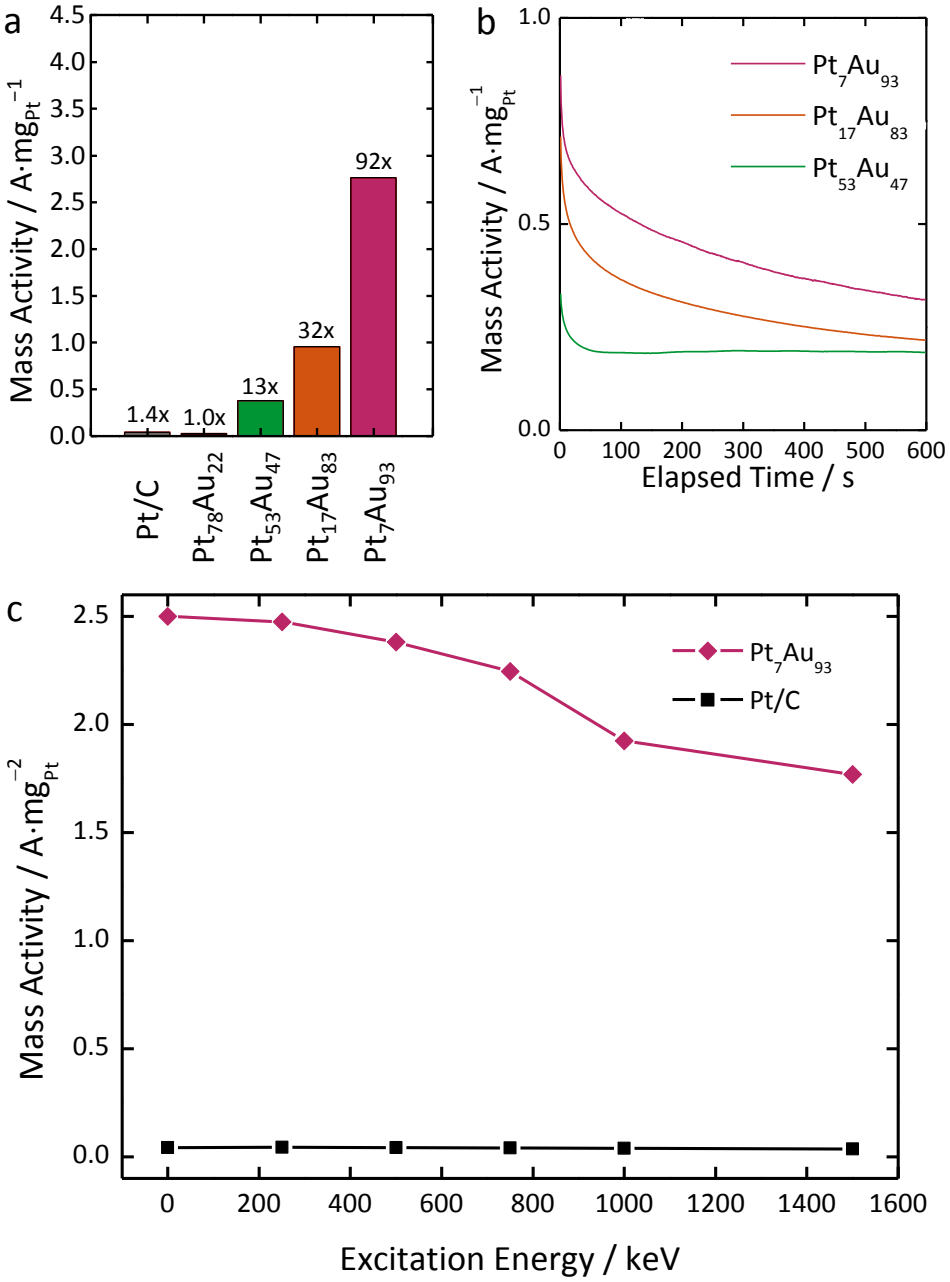


**Figure 7.7.** (a) Peak mass activity, (b) 0.55 $V_{RHE}$ chronoamperometry plots, and (c) mass activity after repeated cycling between 0.1 and 1.1 $V_{RHE}$ for PtAu and commercial Pt/C samples in 0.1 M $HClO_4$ and 0.1 M HCOOH (sweep rate: 10 $mV \cdot s^{-1}$).

The observed orders-of-magnitude increase in catalytic activity certainly warrants further exploration. Because CO has such an impact on the measured activity of Pt-based FAO catalysts, it is an excellent probe molecule to use in this investigation. DFT calculations were performed to study the binding properties of CO at few-atom Pt sites

relative to pure Pt surfaces (Figure 7.8a-b). Multiple binding sites for CO exist at both few-atom and pure Pt surfaces (in order of adsorption energy: apical < bridging < HCP hollow < FCC hollow).The results of these calculations indicate that CO binding is weakened at all binding sites on few-atom Pt cluster surfaces (see Table 7.3); this finding suggests that FAO activity should be enhanced due a reduction of the typically too-strong CO adsorption on Pt (as per the Sabatier Principle).[244] However, while this weakened CO binding is consistent with the observed activity enhancement, it is generally recognized that the surface morphology itself makes the greatest contribution to FAO activity.[118]

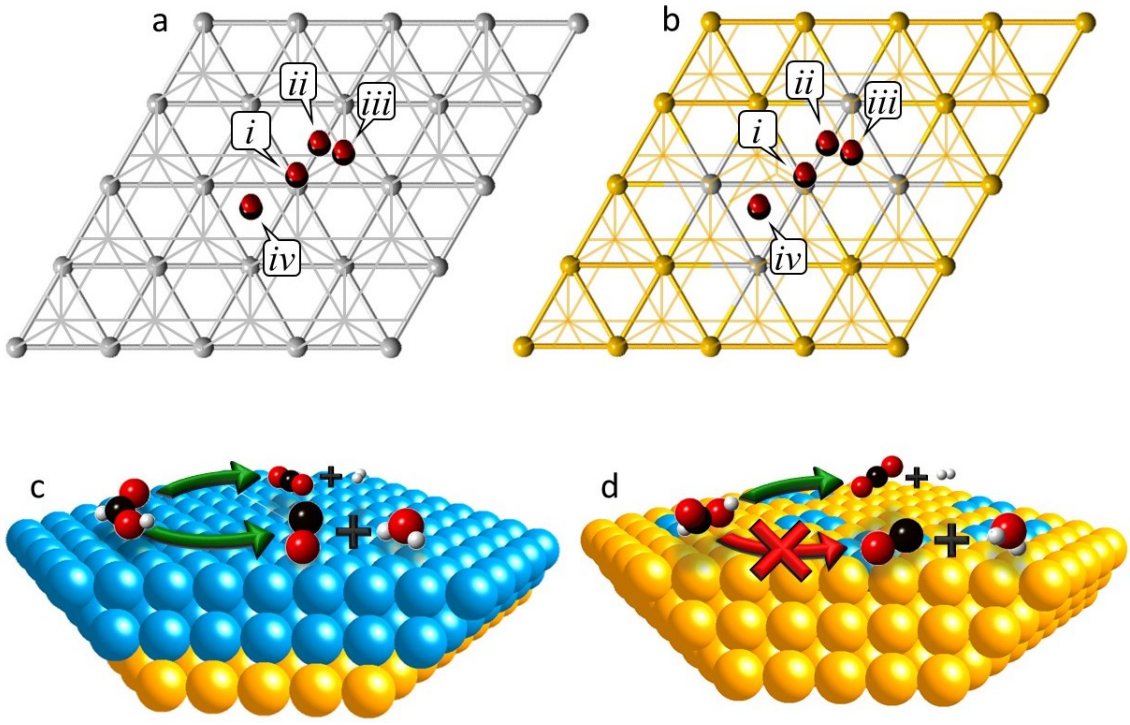


**Figure 7.8.** (*i*) Apical, (*ii*) bridging, (*iii*) HCP hollow, and (*iv*) FCC hollow CO adsorption sites on model (111) lattices of (a) complete core-shell and (b) few-atom cluster Pt surface sites; also shown are predominant FAO reaction pathways on (c) complete core-shell and (d) few-atom Pt surfaces illustrating the selectivity achieved via the ensemble effect.

**Table 7.3.** DFT-calculated adsorption energies for CO at specific sites on monometallic and few-atom Pt surfaces.

| Surface Type | Adsorption Energy at Site / eV | | | |
|---|---|---|---|---|
| | *i* | *ii* | *iii* | *iv* |
| Pure Pt | –1.268 | –1.374 | –1.396 | –1.421 |
| Few-atom Pt | –1.063 | –1.161 | –1.277 | –1.255 |

While multiple possible pathways exist for the oxidation of formic acid at Pt surfaces, the dehydrogenation ($HCOOH_{ads} \rightarrow H_{2(ads)} + CO_{2(ads)}$) and dehydration ($HCOOH \rightarrow H_2O_{(ads)} + CO_{(ads)}$) pathways tend to predominate overall; these pathways are illustrated in Figure 7.8c.[52] Of these pathways, the former pathway is generally responsible for the observed FAO activity of Pt, whereas the latter leads to the formation of adsorbed CO species at Pt sites and blocks them from participating in future reaction steps. Due to its large impact on catalytic activity, surface morphology also plays a large role in determining which of these two reaction pathways will predominate. Both DFT calculations[245] and experimental evidence[246] support this observation, indicating that one to two adjacent Pt atoms are required for formic acid dehydrogenation, whereas the indirect dehydration pathway requires a greater number of adjacent atoms. This "ensemble effect" strongly discourages the detrimental dehydration reaction, leaving the dehydrogenation reaction as the primary reaction pathway, as shown in Figure 7.8d, and readily explains the remarkable activity of the few-atom PtAu nanocatalysts.

## 7.6 Conclusions

A simple and convenient solvothermal method was developed for the synthesis of *ca.* 7 nm PtAu nanoparticles, and their subsequent deposition onto an XC-72 carbon powder support material. Using this method, structured nanoparticles with complete core-shell, sub-monolayer, and few-atom Pt surface structures were generated by carefully controlling the atomic ratios of metal precursors employed in the synthetic reaction. Unlike many other published syntheses, this method required only a single step to achieve significant variation in surface structure. A comprehensive suite of structural characterization techniques was employed to elucidate the bulk and surface structures of these PtAu nanocatalysts, including ICP-OES, TEM, STEM, EDS, and EXAFS. The structural information so obtained was found to be in good agreement with the results of electrochemical characterization performed using both CV and chronoamperometry techniques, and was well able to explain the observed orders-of-magnitude increase in specific FAO activity for the best PtAu nanocatalyst (2.75 $A \cdot mg_{Pt}^{-1}$ for few-atom $Pt_7Au_{93}$) relative to the poorest (0.03 $A \cdot mg_{Pt}^{-1}$ for the pure Pt shell surface of $Pt_{78}Au_{22}$). DFT calculations further supported these results by revealing weakened adsorption of CO to few-atom Pt surfaces, although it was concluded that the ensemble effect was likely the predominant factor affecting CO formation and corresponding activity of each PtAu sample.

Furthermore, this work confirms the ensemble effect theory for reaction pathway selectivity on Pt catalyst materials, and demonstrates the utility of employing multiple, complementary characterization techniques, including powerful structural determination methods such as EXAFS and CV. In particular, EXAFS was able to provide strong

evidence of few-atom, sub-monolayer, and Pt shell surfaces atop a primarily Au-based nanoparticle core. Likewise, a wide range of ancillary characterization techniques were used to provide a clear picture of the physical structure and electronic properties of these PtAu nanoparticles. While incorporating Au does not help compensate for the inherently high material costs of Pt catalysts, the magnitude of the observed FAO activity enhancement does begin to make these nanocatalysts a viable option for real-word applications. Furthermore, while less-expensive elements such as Ag and Cu are liable to be unstable in acidic electrolyte solutions, related research[247–249] shows that employing Pt-based alloys of these metals in conjunction with a non-acidic electrolyte could result in future generations of bimetallic Pt nanocatalysts that exhibit both excellent FAO activity and greatly reduced material costs; with such continued developments, the development and more widespread application of fuel cell technologies could be enabled.

# Chapter 8 – Conclusions and Future Work

## 8.1 Conclusions

Given the extensive use of Pt-based nanoparticles in a range of chemical and electrochemical reactions, it is crucially important to understand the relationships between their surface structure and catalytic activity as fully as possible. In working to address this issue, the studies presented herein have focused on three key goals: exploring the suitability of XAS techniques for characterizing the surface structure of bimetallic Pt nanoparticles, corroborating the inferred surface structures through the use of supplementary techniques, and correlating this structural information with the observed catalytic behavior. A minor emphasis was also placed on the use of simple synthetic methods requiring little subsequent work-up or purification.

In Chapter 3, the study of fluorescent Pt nanoclusters served as an opportunity to gain familiarity with the use of XAS techniques in characterizing Pt-based nanoparticles. The synthesis method was kept as simple as possible, requiring only a metal precursor salt and DMF, which served as a 3-in-1 solvent, reducing agent, and stabilizing ligand. Following sample preparation, and subsequent EXAFS characterization, it was concluded that the nanoclusters responsible for the observed optical fluorescence were not metallic, but instead consisted of polynuclear molecular complexes formed by $Pt^{2+}$ ions with DMF and its oxidation products. Based on this structural evidence, charge transfer involving the Pt atoms and their coordinated ligands was implicated as a possible mechanism for the observed fluorescence. Overall, these results demonstrated that XANES and EXAFS analyses can yield a wealth of structural information for even very small Pt nanoparticles, providing insight that could not be obtained in previous studies using less-specialized techniques.

In Chapter 4, focus was shifted to the synthesis of bimetallic Pt nanoparticles using another "clean" synthetic method. This synthesis was made possible by the use of a few components capable of performing multiple roles simultaneously; CO was used as both a reducing agent and capping ligand, while OAm served as a solvent, ligand, and reducing agent, all in one. Samples with elemental compositions of $Pt_{90}Fe_{10}$, $Pt_{70}Fe_{30}$, and $Pt_{50}Fe_{50}$ were prepared, and structural characterization using XANES and EXAFS techniques revealed a metallic Pt core with a surface layer of $FeO_x$ species ($Pt–FeO_x$), however the possibility of discrete $FeO_x$ nanoparticles being formed was not conclusively ruled out. Regardless, testing the ORR activity of these samples revealed enhanced electrocatalytic activity relative to pure Pt nanoparticles, apparently due to the incorporation of Fe into their surface structure. While a more proximal cause for this activity enhancement could not be clearly determined, *ab initio* simulations were used to investigate the electronic contributions of Fe and $FeO_x$ species interacting with Pt. Thus, through the combined use of XAS data, ORR activity measurements, and *ab initio* calculations, it was possible to infer relationships between the structures of $Pt–FeO_x$ nanoparticles and their catalytic performance. Overall, these results demonstrated the advantage of using complementary XAS data (obtained at X-ray absorption edges of both components) in characterizing the structure of metallic Pt-based nanoparticles.

In Chapter 5, close attention was paid to the effects of electrochemical operating conditions on the surface structure of the $Pt–FeO_x$ nanoparticles prepared in Chapter 4. CV and XAS techniques were found to be instrumental in monitoring the changes in surface structure. The former technique revealed rapid removal of Fe species (including virtually all of the surface-bound $FeO_x$) and gradual rearrangement of the remaining Pt surface, while the latter confirmed that only very little Fe remained in the samples

following this electrochemical treatment. It was further found that those samples which retained detectable levels of Fe exhibited the best catalytic performance in the ORR, suggesting that the enhanced catalytic activity of these nanoparticles was due to sub-surface Fe species beneath the restructured Pt surface. Overall, this study highlighted the crucial importance of performing *in situ* or post-catalysis characterization of materials when investigating relationships between their structure and catalytic activity.

In Chapter 6, AgPt nanoparticles were prepared by forming few-atom Pt nanoclusters at the surfaces of Ag nanoparticle seeds. Based on the amount of Pt added, cluster sizes varied from *ca.* 3 atoms ($Ag_{93}Pt_7$) to *ca.* 13 atoms ($Ag_{81}Pt_{19}$), with Pt coverage of the Ag surface being correlated with greater Pt content (as seen in $Ag_{72}Pt_{28}$ and $Ag_{65}Pt_{35}$). Insight into the structure and growth mechanisms of the Pt surface clusters was made possible by the fitting of EXAFS spectra acquired at both the Ag K and Pt $L_3$ absorption edges. Simulated Pt $L_3$-edge XANES spectra were also generated via *ab initio* methods and used in comparison with experimental spectra to support the inferred nanoparticle structure. Overall, these results demonstrated the high level of structural detail that can be determined using measurements from multiple X-ray absorption edges, and further emphasized the benefits of combining both experimental data and *ab initio* simulations in the characterization of nanoparticle structure.

In Chapter 7, PtAu nanoparticles with distinct core-shell structures were prepared via a one-step reaction by employing a modified version of the "clean" synthetic method (*i.e.*, using CO and OAm) described in Chapter 4. XAS data acquisition was substantially complicated by partial overlap of the Pt and Au $L_3$-edge absorption spectra; however, through the implementation of X-ray fluorescence detection methods and careful channel selection, good-quality spectra were obtained from these PtAu samples in both the

XANES and EXAFS spectral regions. Based on the corroborative results of EXAFS, CV, and FAO electrocatalytic activity analyses, all PtAu nanoparticles were found to share the same general Au-core/Pt-shell structure; however, those with the lowest Pt contents ($Pt_7Au_{93}$ and $Pt_{17}Au_{83}$) showed evidence of Pt surface clusters similar to those observed in Chapter 6.

The high peak oxidation currents and absence of CO oxidation peaks in the FAO activity plots also lent support for the existence of few-atom Pt sites. These findings suggested that, via the ensemble effect, these few-atom sites allowed for extremely high selectivity against the decomposition of formic acid to CO at the Pt surfaces, thereby resulting in much more efficient bimetallic Pt catalyst by preventing CO poisoning. Overall, these results demonstrated the value of employing multiple complementary characterization techniques, including XAS, in conjunction with electrocatalytic activity measurements to perform mechanistic studies on heterogeneous Pt catalysts.

## 8.2 Future Work

### 8.2.1 Complementary Characterization Techniques

Due to the significant structural and compositional differences between the fluorescent Pt nanoclusters synthesized in Chapter 3 and the bimetallic Pt nanoparticles synthesized in subsequent chapters, future studies of these materials would also differ in focus. Despite considerable successes in evaluating the structure of the Pt nanoclusters, some questions still remained to be answered. Although it was determined that these nanoclusters consisted of molecular complexes instead of metallic particles, their exact structural compositions could not be determined using XAS techniques alone. However,

their molecular structure could be advantageous for characterization techniques such as $^{195}$Pt NMR. $^{195}$Pt NMR is usually infeasible for metallic nanoparticles due to extensive coupling between the many Pt atoms, leading to excessive peak broadening;[250] however, it could be much better suited to dealing with the molecular fluorescent Pt nanoclusters that lack this metallic structure.[60] Likewise, measuring XPS peak positions (as has been done by other researchers[26]) would help to determine the oxidation state of Pt with greater confidence than was possible through XAS analysis, thereby strengthening evidence for the molecular structure of these fluorescent Pt nanoclusters.

### 8.2.2 New Metal Compositions

With regard to bimetallic Pt nanoparticles, perhaps the most obvious subject for further experimentation is synthesis. While the synthetic method used to prepare Pt–$FeO_x$ nanoparticles in Chapter 4 resulted in poor incorporation of Fe, this is likely due to inherent difficulty in reducing Fe ions. While fine-tuning of the synthetic method could likely potentially improve the efficiency of Fe addition, new compositions with heightened catalytic activities could also be obtained by substituting Fe with other metals less prone to oxidation. Unfortunately, it is likely that these materials are ultimately doomed to failure as catalysts, as the bulk of the nanoparticles is made up of Pt instead of the cheaper 3d metal. However, the incorporation of alternative metals could also be applied to the synthetic methods employed in Chapters 6 and 7.

Finally, while bimetallic Pt nanoparticles have been quite extensively studied, three-component compositions containing Pt represent a relatively unexplored avenue of research. Unfortunately, performing XAS characterization of such materials is implicitly more likely to face complications (*e.g.*, overlapping absorption edges, or convolution of

EXAFS spectra due to a greater number of distinct metal-metal bond lengths). However, this greater number of components can also be boon, as it affords a greater number of measureable X-ray absorption edges and, thus, perspectives into the nanoparticles' structure. XAS characterization of these trimetallic Pt catalysts could thus be a fruitful next step in the further development of this research.

### 8.2.3 Alternative Catalytic Reactions

While major changes in surface structure were observed for Pt–$FeO_x$ nanoparticles under electrocatalytic conditions, they were not as problematic as were those observed for the AgPt nanoparticles in Chapter 6. Due to the greater corrosion susceptibility of 3d and 4d metals when used in electrocatalysis, particle dissolution was found to be a formidable obstacle to the use of these nanoparticles as electrocatalysts. The catalytic reactions studied in the preceding chapters, however, represent only a small fraction of the potential catalytic applications of Pt. Many other catalytic reactions occur under more forgiving conditions, including non-electrocatalytic reactions in the liquid phase (*e.g.*, lignin hydrolysis[251]) or the gas phase (*e.g.*, CO oxidation[252]), offering potential avenues of research for corrosion-sensitive bimetallic nanoparticles. Furthermore, even reactions such as the ORR that present challenges for less-stable metals can also be performed under less corrosive conditions (*e.g.*, by using a neutral or basic electrolyte), albeit with typically reduced reaction rates.[120] Thus, there exist many potential applications of these bimetallic Pt nanoparticles that remain to be explored.

### 8.2.4 Further Application of XAS Characterization Techniques

In general, the aforementioned studies well-demonstrated the ability of XAS techniques to contribute invaluable insight into the structure and catalytic activity of

bimetallic Pt nanoparticles. These same structural characterization techniques could, however, be extended to the characterization of nanocatalysts *in situ*. As was shown in Chapters 4 and 5, the conditions under which a catalytic reaction is performed can drastically impact surface structure. As a result, being able to monitor nanoparticle surface structure during these reactions provides a much more accurate understanding of the mechanisms involved. The utility of such *in situ* characterization has begun to attract research attention,[63] and will likely only continue to do so with time.

# Appendix A: Letters of Permission

## A1. Permissions for Chapter 3

Local structure of fluorescent platinum nanoclusters

P. N. Duchesne and P. Zhang, *Nanoscale*, 2012, **4**, 4199

**DOI:** 10.1039/C2NR30500C

If you are the author of this article you do not need to formally request permission to reproduce figures, diagrams etc. contained in this article in third party publications or in a thesis or dissertation provided that the correct acknowledgement is given with the reproduced material.

Reproduced material should be attributed as follows:

- For reproduction of material from NJC:
  [Original citation] - Reproduced by permission of The Royal Society of Chemistry (RSC) on behalf of the Centre National de la Recherche Scientifique (CNRS) and the RSC
- For reproduction of material from PCCP:
  [Original citation] - Reproduced by permission of the PCCP Owner Societies
- For reproduction of material from PPS:
  [Original citation] - Reproduced by permission of The Royal Society of Chemistry (RSC) on behalf of the European Society for Photobiology, the European Photochemistry Association, and RSC
- For reproduction of material from all other RSC journals:
  [Original citation] - Reproduced by permission of The Royal Society of Chemistry

If you are the author of this article you still need to obtain permission to reproduce the whole article in a third party publication with the exception of reproduction of the whole article in a thesis or dissertation.

Information about reproducing material from RSC articles with different licences is available on our Permission Requests page.

## A2. Permissions for Chapter 4


Home | Create Account | Help


| | |
|---|---|
| **Title:** | Local Structure, Electronic Behavior, and Electrocatalytic Reactivity of CO-Reduced Platinum–Iron Oxide Nanoparticles |
| **Author:** | Paul N. Duchesne, Guangxu Chen, Nanfeng Zheng, et al |
| **Publication:** | The Journal of Physical Chemistry C |
| **Publisher:** | American Chemical Society |
| **Date:** | Dec 1, 2013 |

Copyright © 2013, American Chemical Society

LOGIN

**If you're a copyright.com user,** you can login to RightsLink using your copyright.com credentials. Already **a RightsLink user** or want to learn more?

**PERMISSION/LICENSE IS GRANTED FOR YOUR ORDER AT NO CHARGE**

This type of permission/license, instead of the standard Terms & Conditions, is sent to you because no fee is being charged for your order. Please note the following:

- Permission is granted for your request in both print and electronic formats, and translations.
- If figures and/or tables were requested, they may be adapted or used in part.
- Please print this page for your records and send a copy of it to your publisher/graduate school.
- Appropriate credit for the requested material should be given as follows: "Reprinted (adapted) with permission from (COMPLETE REFERENCE CITATION). Copyright (YEAR) American Chemical Society." Insert appropriate information in place of the capitalized words.
- One-time permission is granted only for the use specified in your request. No additional uses are granted (such as derivative works or other editions). For any other uses, please submit a new request.

BACK | CLOSE WINDOW

## A3. Permissions for Chapter 5


Home | Create Account | Help


**Title:** Surface Reconstruction and Reactivity of Platinum–Iron Oxide Nanoparticles

**Author:** Paul N. Duchesne, Guangxu Chen, Xiaojing Zhao, et al

**Publication:** The Journal of Physical Chemistry C

**Publisher:** American Chemical Society

**Date:** Dec 1, 2014



LOGIN

If you're a copyright.com user, you can login to RightsLink using your copyright.com credentials. Already a RightsLink user or want to learn more?

**PERMISSION/LICENSE IS GRANTED FOR YOUR ORDER AT NO CHARGE**

This type of permission/license, instead of the standard Terms & Conditions, is sent to you because no fee is being charged for your order. Please note the following:

- Permission is granted for your request in both print and electronic formats, and translations.
- If figures and/or tables were requested, they may be adapted or used in part.
- Please print this page for your records and send a copy of it to your publisher/graduate school.
- Appropriate credit for the requested material should be given as follows: "Reprinted (adapted) with permission from (COMPLETE REFERENCE CITATION). Copyright (YEAR) American Chemical Society." Insert appropriate information in place of the capitalized words.
- One-time permission is granted only for the use specified in your request. No additional uses are granted (such as derivative works or other editions). For any other uses, please submit a new request.

BACK | CLOSE WINDOW

## A4. Permissions for Chapter 6


Home | Create Account | Help

ACS Publications
Most Trusted. Most Cited. Most Read.

**Title:** Element-Specific Analysis of the Growth Mechanism, Local Structure, and Electronic Properties of Pt Clusters Formed on Ag Nanoparticle Surfaces

**Author:** Paul N. Duchesne, Peng Zhang

**Publication:** The Journal of Physical Chemistry C

**Publisher:** American Chemical Society

**Date:** Sep 1, 2014



LOGIN

If you're a copyright.com user, you can login to RightsLink using your copyright.com credentials. Already a RightsLink user or want to learn more?

**PERMISSION/LICENSE IS GRANTED FOR YOUR ORDER AT NO CHARGE**

This type of permission/license, instead of the standard Terms & Conditions, is sent to you because no fee is being charged for your order. Please note the following:

- Permission is granted for your request in both print and electronic formats, and translations.
- If figures and/or tables were requested, they may be adapted or used in part.
- Please print this page for your records and send a copy of it to your publisher/graduate school.
- Appropriate credit for the requested material should be given as follows: "Reprinted (adapted) with permission from (COMPLETE REFERENCE CITATION). Copyright (YEAR) American Chemical Society." Insert appropriate information in place of the capitalized words.
- One-time permission is granted only for the use specified in your request. No additional uses are granted (such as derivative works or other editions). For any other uses, please submit a new request.

BACK | CLOSE WINDOW

# References


(1) Portney, N. G.; Ozkan, M. *Anal. Bioanal. Chem.* **2006**, *384*, 620.

(2) Astruc, D. *Transition-metal Nanoparticles in Catalysis: From Historical Background to the State-of-the Art*; 2008.

(3) Nel, A.; Xia, T.; Mädler, L.; Li, N. *Science* **2006**, *311*, 622.

(4) Yuan, B.; Cademartiri, L. *J. Mater. Sci. Technol.* **2015**, *31*, 607.

(5) Tan, C.; Zhang, H. *Nat Commun* **2015**, *6*, 1.

(6) Jain, P. K.; Huang, X.; El-Sayed, I. H.; El-Sayed, M. A. *Plasmonics* **2007**, *2*, 107.

(7) Kim, J. W.; Deaton, R. *Part. Part. Syst. Charact.* **2013**, *30*, 117.

(8) Barber, D. J.; Freestone, I. C. *Archaeometry* **1990**, *1*, 33.

(9) Faraday, M. *Phil. Trans. R. Soc. Lond.* **1857**, *147*, 145.

(10) Web of Science ("nanopart*") https://www.webofknowledge.com (accessed Oct 7, 2015).

(11) Wang, H.-H.; Zhou, Z.-Y.; Yuan, Q.; Tian, N.; Sun, S.-G. *Chem. Comm.* **2011**, *47*, 3407.

(12) Gambinossi, F.; Mylon, S. E.; Ferri, J. K. *Adv. Colloid Interface Sci.* **2015**, *222*, 332.

(13) Yavari, A. R. *Mater. Trans.* **1995**, *36*, 228.

(14) Suryanarayana, C. *Prog. Mater. Sci.* **2001**, *46*, 1.

(15) Rehbock, C.; Jakobi, J.; Gamrad, L.; van der Meer, S.; Tiedemann, D.; Taylor, U.; Kues, W.; Rath, D.; Barcikowski, S. *Beilstein J. Nanotechnol.* **2014**, *5*, 1523.

(16) Wee, J.-H.; Lee, K.-Y.; Kim, S. H. *J. Power Sources* **2007**, *165*, 667.

(17) Tsai, C. F.; Yeh, K. Y.; Wu, P. W.; Hsieh, Y. F.; Lin, P. *J. Alloys Compd.* **2009**, *478*, 868.

(18) Teo, B. K.; Sun, X. H. *J. Clust. Sci.* **2006**, *17*, 529.

(19) Na, K.; Zhang, Q.; Somorjai, G. A. *J. Clust. Sci.* **2014**, *25*, 83.

(20) Gupta, A. K.; Gupta, M. *Biomaterials* **2005**, *26*, 3995.

(21) Nguyen, T.-D. *Nanoscale* **2013**, *5*, 9455.

(22) Filankembo, A.; Giorgio, S.; Lisiecki, I.; Pileni, M. P. **2003**, *107*, 7492.

(23) Chen, M.; Wu, B.; Yang, J.; Zheng, N. *Adv. Mater.* **2012**, *24*, 862.

(24) Xin, H.; Holewinski, A.; Linic, S. *ACS Catal.* **2012**, *2*, 12.

(25) Dai, Y.; Mu, X.; Tan, Y.; Lin, K.; Yang, Z.; Zheng, N.; Fu, G. *J. Am. Chem. Soc.* **2012**, *134*, 7073.

(26) Kawasaki, H.; Yamamoto, H.; Fujimori, H.; Arakawa, R.; Inada, M.; Iwasaki, Y. *Chem. Comm.* **2010**, *46*, 3759.

(27) Wu, B.; Zheng, N. *Nano Today* **2013**, *8*, 168.

(28) Joseyacaman, M.; Avalosborja, M. *Cat. Rev - Sci. Eng.* **1992**, *34*, 55.

(29) Li, X.; Wei, J.; Aifantis, K. E.; Fan, Y.; Feng, Q.; Cui, F. **2016**, *104A*, 1285.

(30) Benn, T. M.; Westerhoff, P. *Environ. Sci. Technol.* **2008**, *42*, 4133.

(31) Morita, T.; Kojima, K. In *Proton Exchange Membrane Fuel Cells 8, Pts 1 and 2*; 2008; pp 185–198.

(32) Stumper, J.; Stone, C. *J. Power Sources* **2008**, *176*, 468.

(33) Shao, Y.; Cheng, Y.; Duan, W.; Wang, W.; Lin, Y.; Wang, Y.; Liu, J. *ACS Catal.* **2015**, *5*, 7288.

(34) Aricò, A. S.; Bruce, P.; Scrosati, B.; Tarascon, J.-M.; van Schalkwijk, W. *Nat. Mater.* **2005**, *4*, 366.

(35) Smith, A. M.; Nie, S. *Acc. Chem. Res.* **2010**, *43*, 190.

(36) Jin, R. *Nanoscale* **2010**, *2*, 343.

(37) Chen, A.; Holt-Hindle, P. *Chem. Rev.* **2010**, *110*, 3767.

(38) Debe, M. K. *Nature* **2012**, *486*, 43.

(39) Powering the future: Hydrogen fuel cell vehicles could change mobility forever. http://www.toyota-global.com/innovation/environmental_technology/fuelcell_vehicle/ (accessed Nov 5, 2015).

(40) Yu, X.; Ye, S. *J. Power Sources* **2007**, *172*, 145.

(41) Marquis, J.; Coppens, M. O. *Chem. Eng. Sci.* **2013**, *102*, 151.

(42) Chumillas, S.; Busó-Rogero, C.; Solla-Gullón, J.; Vidal-Iglesias, F. J.; Herrero, E.; Feliu, J. M. *Electrochem. commun.* **2011**, *13*, 1194.

(43) Wang, S.; Jiang, S. P.; White, T. J.; Guo, J.; Wang, X. *J. Phys. Chem. C* **2009**, *113*, 18935.

(44) Kaidanovych, Z. *Adv. Nanoparticles* **2013**, *2*, 32.

(45) Dahl, J. A.; Maddux, B. L. S.; Hutchison, J. E. *Chem. Rev.* **2007**, *107*, 2228.

(46) Shao, M.; Odell, J.; Humbert, M.; Yu, T.; Xia, Y. *J. Phys. Chem. C* **2013**, *117*, 4172.

(47) Stamenkovic, V. R.; Fowler, B.; Mun, B. S.; Wang, G.; Ross, P. N.; Lucas, C. A.; Marković, N. M. *Science* **2007**, *315*, 493.

(48) Loukrakpam, R.; Luo, J.; He, T.; Chen, Y.; Xu, Z.; Njoki, P. N.; Wanjala, B. N.; Fang, B.; Mott, D.; Yin, J.; Klar, J.; Powell, B.; Zhong, C.-J. *J. Phys. Chem. C* **2011**, *115*, 1682.

(49) Poudyal, N.; Chaubey, G. S.; Nandwana, V.; Rong, C.-B.; Yano, K.; Liu, J. P. *Nanotechnology* **2008**, *19*, 355601.

(50) Park, S.; Xie, Y.; Weaver, M. J. *Langmuir* **2002**, *18*, 5792.

(51) Chen, D.-J.; Tong, Y. J. *Angew. Chemie Int. Ed.* **2015**, *54*, 9394.

(52) Zhong, W.; Zhang, D. *Catal. Commun.* **2012**, *29*, 82.

(53) Wu, B.; Zheng, N.; Fu, G. *Chem. Comm.* **2011**, *47*, 1039.

(54) Liu, X.; Wang, D.; Li, Y. *Nano Today* **2012**, *7*, 448.

(55) Wang, D.; Li, Y. *Adv. Mater.* **2011**, *23*, 1044.

(56) Parr, J. M. P.; Kim, Y. *Environ. Sci. Water Res. Technol.* **2016**, *2*, 304.

(57) Peretyazhko, T. S.; Zhang, Q.; Colvin, V. L. *Environ. Sci. Technol.* **2014**, *48*, 11954.

(58) Hokita, Y.; Kanzaki, M.; Sugiyama, T.; Arakawa, R.; Kawasaki, H. *ACS Appl. Mater. Interfaces* **2015**, *7*, 19382.

(59) Patterson, A. L. *Phys. Rev.* **1939**, *56*, 978.

(60) Gabano, E.; Marengo, E.; Bobba, M.; Robotti, E.; Cassino, C.; Botta, M.; Osella, D. *Coord. Chem. Rev.* **2006**, *250*, 2158.

(61) Marbella, L. E.; Millstone, J. E. *Chem. Mater.* **2015**, *27*, 2721.

(62) Bertagnolli, H.; Ertel, T. S. *Angew. Chemie Int. Ed.* **1994**, *33*, 45.

(63) Frenkel, A. I. *Chem. Soc. Rev.* **2012**, *41*, 8163.

(64) Sinfelt, J. H.; Meitzner, G. D. *Acc. Chem. Res.* **1993**, *26*, 1.

(65) Fouras, A.; Kitchen, M. J.; Dubsky, S.; Lewis, R. A.; Hooper, S. B.; Hourigan, K. *J. Appl. Phys.* **2009**, *105*, 102009.

(66) Cnudde, V.; Boone, M. N. *Earth Sci. Rev.* **2013**, *123*, 1.

(67) Lytle, F. W. *J. Synchrotron Radiat.* **1999**, *6*, 123.

(68) Prestipino, C.; Mathon, O.; Hino, R.; Beteva, A.; Pascarelli, S. *J. Synchrotron Radiat.* **2011**, *18*, 176.

(69) Rehr, J. J. *Rev. Mod. Phys.* **2000**, *72*, 621.

(70) Gullikse, E. In *X-ray Data Booklet*; 2009; pp 1–38.

(71) Rehr, J. J.; Ankudinov, A. L. *Coord. Chem. Rev.* **2005**, *249*, 131.

(72) Jablonski, A. *Surf. Sci. Rep.* **2002**, *47*, 33.

(73) Mottana, A. *J. Electron Spectros. Relat. Phenomena* **2014**, *196*, 14.

(74) de Groot, F. *Chem. Rev.* **2001**, *101*, 1779.

(75) Gräfe, M.; Donner, E.; Collins, R. N.; Lombi, E. *Anal. Chim. Acta* **2014**, *822*, 1.

(76) Ressler, T. *J. Synchrotron Radiat.* **1998**, *5*, 118.

(77) Ravel, B.; Newville, M. *J. Synchrotron Radiat.* **2005**, *12*, 537.

(78) Ankudinov, A. L.; Ravel, B.; Rehr, J. J.; Conradson, S. D. *Phys. Rev. B* **1998**, *58*, 7565.

(79) Kohn, S. C. *Terra Nov.* **1995**, *7*, 554.

(80) Kelly, S. D.; Ravel, B. In *AIP Conf. Proc.*; Stanford, CA, 2006; p 132.

(81) Abd El All, N.; Thiodjio Sendja, B.; Grisenti, R.; Rocca, F.; Diop, D.; Mathon, O.; Pascarelli, S.; Fornasini, P. *J. Synchrotron Radiat.* **2013**, *20*, 603.

(82) Curis, E.; Bénazeth, S. *J. Synchrotron Radiat.* **2005**, *12*, 361.

(83) Newville, M.; Boyanov, B. I.; Sayers, D. E. *J. Synchrotron Radiat.* **1999**, *6*, 264.

(84) Penner-Hahn, J. E. *Coord. Chem. Rev.* **2005**, *249*, 161.

(85) Bobyr, E.; Lassila, J. K.; Wiersma-Koch, H. I.; Fenn, T. D.; Lee, J. J.; Nikolic-

Hughes, I.; Hodgson, K. O.; Rees, D. C.; Hedman, B.; Herschlag, D. *J. Mol. Biol.* **2012**, *415*, 102.

(86) Cormier, Z. R.; Andreas, H. A.; Zhang, P. *J. Phys. Chem.* **2011**, *4*, 19117.

(87) Trudel, S.; Daryl Crozier, E.; Gordon, R. A.; Budnik, P. S.; Hill, R. H. *J. Solid State Chem.* **2011**, *184*, 1025.

(88) Zhang, W.; Duchesne, P. N.; Gong, Z.; Wu, S.; Ma, L.; Jiang, Z.; Zhang, S.; Zhang, P.; Mi, J.; Yang, Y. *J. Phys. Chem. C* **2013**, *117*, 11498.

(89) Heald, M. A.; Marion, J. *Classical Electromagnetic Radiation*, 3rd Ed.; Brooks Cole: Pacific Grove, CA, 1994.

(90) van Putten, E.; Akbulut, D.; Bertolotti, J.; Vos, W.; Lagendijk, A.; Mosk, A. *Phys. Rev. Lett.* **2011**, *106*, 1.

(91) Dan, D.; Yao, B.; Lei, M. *Chinese Sci. Bull.* **2014**, *59*, 1291.

(92) Knoll, M.; Ruska, E. *Ann. Phys.* **1932**, *12*, 641.

(93) Leung, K. N.; Pincosy, P. A.; Ehlers, K. W. *Rev. Sci. Instrum.* **1984**, *55*, 1064.

(94) Williams, D. B.; Carter, C. B. *Transmission Electron Microscopy: A Textbook for Materials Science, Volume 2*, 2nd ed.; Springer Science & Business Media: New York, NY, 2009.

(95) Busch, H. *Ann. Phys.* **1926**, *81*, 974.

(96) Giancoli, D. C. In *Physics for Scientists and Engineers with Modern Physics*; Corey, P. F., Fisher, S., Reeves, A., Chelton, D., Mullaney, R., Phillips, J., Eds.; Prentice Hall: Upper Saddle River, NJ, 2000; p 961.

(97) Skoog, D. A.; Holler, F. J.; Nieman, T. A. *Principles of Instrumental Analysis*, 5th Ed.; Vondeling, J., Pecuilis, V., Sherman, M., Bortel, J., Messina, F., Eds.; Belmont, CA, 1998.

(98) Smith, A. F.; Weiner, R. G.; Bower, M. M.; Dragnea, B.; Skrabalak, S. E. *J. Phys. Chem. C* **2015**, *119*, 22114.

(99) Knappett, B. R.; Abdulkin, P.; Ringe, E.; Jefferson, D. a; Lozano-Perez, S.; Rojas, T. C.; Fernández, A.; Wheatley, A. E. H. *Nanoscale* **2013**, *5*, 5765.

(100) Hunger, M.; Weitkamp, J. *Angew. Chem. Int. Ed.* **2001**, *40*, 2954.

(101) Hostetler, M. J.; Wingate, J. E.; Zhong, C.-J.; Harris, J. E.; Vachet, R. W.; Clark, M. R.; Londono, J. D.; Green, S. J.; Stokes, J. J.; Wignall, G. D.; Glish, G. L.; Porter, M. D.; Evans, N. D.; Murray, R. W. *Langmuir* **1998**, *14*, 17.

(102) Pena-Pereira, F.; Costas-Mora, I.; Romero, V.; Lavilla, I.; Bendicho, C. *Trends Anal. Chem.* **2011**, *30*, 1637.

(103) Pavia, D. L.; Lampman, G. M.; Kriz, G. S. *Introduction to Spectroscopy*, 3rd ed.; Vondeling, J., Kiselica, S., Eds.; Nelson Thomson Learning: Toronto, 2001.

(104) Svanberg, S. *Atomic and Molecular Spectroscopy: Basic Aspects and Practical Applications*, 4th ed.; Springer-Verlag: New York, NY, 2004.

(105) Jentoft, F. C. *Chapter 3 Ultraviolet-Visible-Near Infrared Spectroscopy in Catalysis. Theory, Experiment, Analysis, and Application Under Reaction Conditions*, 1st ed.; Elsevier Inc., 2009; Vol. 52.

(106) Sanyal, U.; Davis, D. T.; Jagirdar, B. R. *Dalt. Trans.* **2013**, *42*, 7147.

(107) Laider, K. J.; Meiser, J. H.; Sanctuary, B. C. *Physical Chemistry*, 4th ed.; Stratton, R., Ed.; Houghton Mifflin Company: Boston, 2003.

(108) Clark, B. J.; Frost, T.; Russell, M. A. *UV Spectroscopy: Techniques, instrumentation and data handling, Volume 4*, 1st ed.; Chapman & Hall: London, UK, 1993.

(109) Chevrier, D. M.; Chatt, A.; Zhang, P. *J. Nanophotonics* **2012**, *6*, 64504.

(110) Qian, H.; Zhu, M.; Wu, Z.; Jin, R. *Acc. Chem. Res.* **2012**, *45*, 1470.

(111) Rand, D. A. J.; Woods, R. *J. Electroanal. Chem. Interfacial Electrochem.* **1972**, *36*, 57.

(112) Li, W.; Zhou, W.; Li, H.; Zhou, Z.; Zhou, B.; Sun, G.; Xin, Q. **2004**, *49*, 1045.

(113) Pletcher, D. *A First Course in Electrode Processes*, 2nd ed.; Royal Society of Chemistry: Cambridge, 2009.

(114) Wu, J.; Yang, H. *Accounts Chem. Res. Receiv. January* **2013**, *46*, 1848.

(115) Shinozaki, K.; Zack, J. W.; Richards, R. M.; Pivovar, B. S.; Kocha, S. S. *J. Electrochem. Soc.* **2015**, *162*, F1144.

(116) Waleed Shinwari, M.; Zhitomirsky, D.; Deen, I. A.; Selvaganapathy, P. R.; Jamal Deen, M.; Landheer, D. *Sensors* **2010**, *10*, 1679.

(117) El-Nagar, G. A.; Mohammad, A. M.; El-Deab, M. S.; El-Anadouli, B. E. *Int. J. Electrochem. Sci.* **2014**, *9*, 4523.

(118) Jiang, K.; Zhang, H.; Cai, W. *Phys. Chem. Chem. Phys.* **2014**, *16*, 20360.

(119) Batchelor-McAuley, C.; Katelhon, E.; Barnes, E. O.; Compton, R. G.; Laborda, E.; Molina, A. *ChemistryOpen* **2015**, *4*, 224.

(120) Ramaswamy, N.; Mukerjee, S. **2012**, *2012*, 491604.

(121) Attard, G. A.; Brew, A. *J. Electroanal. Chem.* **2015**, *747*, 123.

(122) Wang, R.; Jia, J.; Wang, H. **2013**, *17*, 1021.

(123) Duchesne, P. N.; Zhang, P. *Nanoscale* **2012**, *4*, 4199.

(124) Hyotanishi, M.; Isomura, Y.; Yamamoto, H.; Kawasaki, H.; Obora, Y. *Chem. Comm.* **2011**, *47*, 5750.

(125) Kawasaki, H.; Yamamoto, H.; Fujimori, H.; Arakawa, R.; Iwasaki, Y.; Inada, M. *Langmuir* **2010**, *26*, 5926.

(126) Lin, C. A. J.; Lee, C. H.; Hsieh, J. T.; Wang, H. H.; Li, J. K.; Shen, J. L.; Chan, W. H.; Yeh, H. I.; Chang, W. H. *J. Med. Biol. Eng.* **2009**, *29*, 276.

(127) Bertsch, S.; Braunschweig, H.; Forster, M.; Gruss, K.; Radacki, K. *Inorg. Chem.* **2011**, *50*, 1816.

(128) Müller, T. E.; Ingold, F.; Menzer, S.; Mingos, D. M. P.; Williams, D. J. *J. Organomet. Chem.* **1997**, *528*, 163.

(129) Johnston, R. L. *Atomic and Molecular Clusters*; Taylor and Francis: London, 2002.

(130) Pastoriza-Santos, I.; Liz-Marzán, L. M. *Pure Appl. Chem.* **2000**, *72*, 83.

(131) Takao, K.; Takao, S.; Scheinost, A. C.; Bernhard, G.; Hennig, C. *Inorg. Chim. Acta* **2010**, *363*, 802.

(132) Jalilehvand, F.; Laffin, L. J. *Inorg. Chem.* **2008**, *47*, 3248.

(133) Provost, K.; Bouvet-Muller, D.; Crauste-Manciet, S.; Moscovici, J.; Olivi, L.; Vlaic, G.; Michalowicz, A. *Biochimie* **2009**, *91*, 1301.

(134) Spieker, W. A.; Liu, J.; Miller, J. T.; Kropf, A. J.; Regalbuto, J. R. *Appl. Catal., A* **2002**, *232*, 219.

(135) Teo, B. K. In *EXAFS: Basic Principles and Data Analysis*; Berlin, 1986; p 21.

(136) Meissler, G. L.; Tarr, D. A. *Inorganic Chemistry*, 3rd ed.; Folchetti, N., Ed.; Pearson Education, Inc.: Upper Saddle River, NJ, 2004.

(137) Sham, T. K.; Naftel, S. J.; Coulthard, I. *J. Appl. Phys.* **1996**, *79*, 7134.

(138) Mattheiss, L. F.; Dietz, R. E. *Phys. Rev. B* **1980**, *22*, 1663.

(139) Xu, J.; Zhao, T.; Liang, Z.; Zhu, L. *Chem. Mater.* **2008**, *20*, 1688.

(140) MacDonald, M. A.; Zhang, P.; Qian, H.; Jin, R. *J. Phys. Chem. Lett.* **2010**, *1*, 1821.

(141) MacDonald, M. A.; Chevrier, D. M.; Zhang, P. *J. Phys. Chem.* **2011**, *25*, 15282.

(142) Koshevoy, I. O.; Haukka, M.; Pakkanen, T. A.; Tunik, S. P.; Vainiotalo, P. *Organometallics* **2005**, *24*, 3516.

(143) Rappoport, Z.; Kaspi, J.; Apeloig, Y. *J. Am. Chem. Soc.* **1974**, *96*, 2614.

(144) Longoni, G.; Chini, P. *J. Am. Chem. Soc.* **1976**, *98*, 7225.

(145) Osakada, K.; Tanabe, M. *Bull. Chem. Soc. Jap.* **2005**, *78*, 1887.

(146) Cucciolito, M. E.; De Felice, V.; Roviello, G.; Ruffo, F. *Eur. J. Inorg. Chem.* **2011**, *2011*, 457.

(147) Krause, J.; Cestaric, G.; Haack, K.-J.; Seevogel, K.; Storm, W.; Pörschke, K.-R. *J. Am* **1999**, *121*, 9807.

(148) Beletskaya, I.; Moberg, C. *Chem. Rev.* **1999**, *99*, 3435.

(149) Hermann, D.; Näther, C.; Ruschewitz, U. *Solid State Sci.* **2011**, *13*, 1096.

(150) Zypman, F.; Byriel, K. A.; Garrett, J. M.; Hall, J. R.; Kennard, C. H. L.; Mathieson, M. T.; Stranger, R. *Inorg. Chem.* **1995**, *34*, 5646.

(151) Alexander, K. A.; Bryan, S. A.; Fronczek, F. R.; Fultz, W. C.; Rheingold, A. L.; Roundhill, D. M.; Stein, P.; Watkinsic, S. F. *Inorg. Chem.* **1985**, *24*, 2803.

(152) Bercaw, J. E.; Durrell, A. C.; Gray, H. B.; Green, J. C.; Hazari, N.; Labinger, J. A.; Winkler, J. R. *Inorg. Chem.* **2010**, *49*, 1801.

(153) Henderson, W.; Nicholson, B. K.; Rickard, C. E. F. *Inorg. Chim. Acta* **2001**, *320*, 101.

(154) Jansen, B. A. J.; Wielaard, P.; Kalayda, G. V; Ferrari, M.; Molenaar, C.; Tanke, H. J.; Brouwer, J.; Reedijk, J. *J. Biol. Inorg. Chem.* **2004**, *9*, 403.

(155) Matsumoto, K.; Arai, S.; Ochiai, M.; Chen, W.; Nakata, A.; Nakai, H.; Kinoshita, S. *Inorg. Chem.* **2005**, *44*, 8552.

(156) Rochon, F. D.; Robert, J.; Monique, M.; Butlerlb, I. S. *Inorg. Chem.* **1994**, *33*, 4485.

(157) Yip, H. K.; Che, C. M.; Zhou, Z. Y.; Mak, C. W. *J. Chem. Soc., Chem. Comm.* **1992**, 1369.

(158) Roundhill, D. M.; Gray, H. B.; Che, C. M. *Acc. Chem. Res.* **1989**, *22*, 55.

(159) Bayindir, Z.; Duchesne, P. N.; Cook, S. C.; MacDonald, M. A.; Zhang, P. *J. Chem. Phys.* **2009**, *131*, 244716.

(160) Simms, G. A.; Padmos, J. D.; Zhang, P. *J. Chem. Phys.* **2009**, *131*, 214703.

(161) Shimazaki, Y.; Yajima, T.; Tani, F.; Karasawa, S.; Fukui, K.; Naruta, Y.; Yamauchi, O. *J. Am. Chem. Soc.* **2007**, *129*, 2559.

(162) Atzei, D.; De Filippo, D.; Rossi, A.; Porcelli, M. *Spectrochim. Acta, Part A* **2001**, *57A*, 1073.

(163) Xing, R.; Wang, X.; Zhang, C.; Wang, J.; Zhang, Y.; Song, Y.; Guo, Z. *J. Mater. Chem.* **2011**, *21*, 11142.

(164) McNeillie, A.; Brown, D. H.; Smith, W. E.; Gibson, M. *J. Chem. Soc., Dalt. Trans.* **1980**, 767.

(165) Jermakowicz-Bartkowiak, D.; Kolarz, B. N.; Tylus, W. *Polymer* **2003**, *44*, 5797.

(166) Kozlova, A. P.; Kozlov, A. I.; Sugiyama, S.; Matsui, Y.; Asakura, K.; Iwasawa, Y. *J. Catal.* **1999**, *48*, 37.

(167) Pilśniak, M.; Trochimczuk, A. W.; Apostoluk, W. *Sep. Sci. Technol.* **2009**, *44*, 1099.

(168) Zhao, M.; Crooks, R. M. *Adv. Mater.* **2001**, *34*, 181.

(169) Kirner, U. K.; Schierbaum, K. D.; Göpel, W. *Fresen. J. Anal. Chem.* **1991**, *341*, 416.

(170) Tanaka, S.-I.; Miyazaki, J.; Tiwari, D. K.; Jin, T.; Inouye, Y. *Angew. Chem. Int. Ed.* **2011**, *50*, 431.

(171) Huang, X.; Li, B.; Li, L.; Zhang, H.; Majeed, I.; Hussain, I.; Tan, B. *J. Phys. Chem. C* **2012**, *116*, 448.

(172) Duchesne, P. N.; Chen, G.; Zheng, N.; Zhang, P. *J. Phys. Chem. C* **2013**, *117*, 26324.

(173) Scrosati, B.; Garche, J. *J. Power Sources* **2010**, *195*, 2419.

(174) Simon, P.; Gogotsi, Y. *Nat. Mater.* **2008**, *7*, 845.

(175) Carrette, L.; Friedrich, K. A.; Stimming, U. *ChemPhysChem* **2000**, *1*, 162.

(176) Cericola, D.; Kötz, R. *Electrochim. Acta* **2012**, *72*, 1.

(177) Stamenkovic, V. R.; Mun, B. S.; Arenz, M.; Mayrhofer, K. J. J.; Lucas, C. A.; Wang, G.; Ross, P. N.; Markovic, N. M. *Nat. Mater.* **2007**, *6*, 241.

(178) Borup, R.; Meyers, J.; Pivovar, B.; Kim, Y. S.; Mukundan, R.; Garland, N.; Myers, D.; Wilson, M.; Garzon, F.; Wood, D.; Zelenay, P.; More, K.; Stroh, K.; Zawodzinski, T.; Boncella, J.; McGrath, J. E.; Inaba, M.; Miyatake, K.; Hori, M.; Ota, K.; Ogumi, Z.; Miyata, S.; Nishikata, A.; Siroma, Z.; Uchimoto, Y.; Yasuda, K.; Kimijima, K.-I.; Iwashita, N. *Chem. Rev.* **2007**, *107*, 3904.

(179) Kettler, P. B. *Org. Process Res. Dev.* **2003**, *7*, 342.

(180) Wang, H.-F.; Liu, Z.-P. *J. Am. Chem. Soc.* **2008**, *130*, 10996.

(181) Santra, A. K.; Goodman, D. W. *Electrochim. Acta* **2002**, *47*, 3595.

(182) Greeley, J.; Stephens, I. E. L.; Bondarenko, A. S.; Johansson, T. P.; Hansen, H. A.; Jaramillo, T. F.; Rossmeisl, J.; Chorkendorff, I.; Nørskov, J. K. *Nat. Chem.* **2009**, *1*, 552.

(183) Zaera, F. *Appl. Catal., A* **2002**, *229*, 75.

(184) Bing, Y.; Liu, H.; Zhang, L.; Ghosh, D.; Zhang, J. *Chem. Soc. Rev.* **2010**, *39*, 2184.

(185) Wanjala, B. N.; Fang, B.; Shan, S.; Petkov, V.; Zhu, P.; Loukrakpam, R.; Chen, Y.; Luo, J.; Yin, J.; Yang, L.; Shao, M.; Zhong, C.-J. *Chem. Mater.* **2012**, *24*, 4283.

(186) Luo, J.; Yin, J.; Loukrakpam, R.; Wanjala, B. N.; Fang, B.; Shan, S.; Yang, L.; Nie, M.; Ng, M. S.; Kinzler, J.; Kim, Y.-S.; Luo, K. K.; Zhong, C.-J. *J. Electroanal. Chem.* **2013**, *688*, 196.

(187) Malheiro, A. R.; Perez, J.; Villullas, H. M. *J. Electrochem. Soc.* **2009**, *156*, B51.

(188) Liu, Z.; Ma, L.; Zhang, J.; Hongsirikarn, K.; Goodwin, J. G. *Catal. Rev. Sci. Eng.* **2013**, *55*, 255.

(189) Chen, G.; Tan, Y.; Wu, B.; Fu, G.; Zheng, N. *Chem. Comm.* **2012**, *48*, 2758.

(190) Xu, Y.; Hou, S.; Liu, Y.; Zhang, Y.; Wang, H.; Zhang, B. *Chem. Comm.* **2012**, *48*, 2665.

(191) Pachón, L. D.; Rothenberg, G. *App. Organomet. Chem.* **2008**, *22*, 288.

(192) Garsany, Y.; Baturina, O. A.; Swider-Lyons, K. E.; Kocha, S. S. *Anal. Chem.* **2010**, *82*, 6321.

(193) Chen, W.; Ghosh, D.; Sun, J.; Tong, M. C.; Deng, F.; Chen, S. *Electrochim. Acta* **2007**, *53*, 1150.

(194) Mino, L.; Agostini, G.; Borfecchia, E.; Gianolio, D.; Piovano, A.; Gallo, E.; Lamberti, C. *J. Phys. D Appl. Phys.* **2013**, *46*, 423001.

(195) Liu, F.; Wechsler, D.; Zhang, P. *Chem. Phys. Lett.* **2008**, *461*, 254.

(196) Thomson, J. W.; Cademartiri, L.; MacDonald, M.; Petrov, S.; Calestani, G.; Zhang, P.; Ozin, G. a. *J. Am. Chem. Soc.* **2010**, *132*, 9058.

(197) Dash, P.; Bond, T.; Fowler, C.; Hou, W.; Coombs, N.; Scott, R. W. J. *J. Phys. Chem. C* **2009**, *113*, 12719.

(198) Scott, R. W. J.; Wilson, O. M.; Oh, S.; Kenik, E. A.; Crooks, R. M. *J. Am. Chem. Soc.* **2004**, *126*, 15583.

(199) Schneider, C. A.; Rasband, W. S.; Eliceiri, K. W. *Nat. Methods* **2012**, *9*, 671.

(200) Wang, Y.; Zhang, H.; Yao, X.; Zhao, H. *J. Phys. Chem. C* **2013**, *117*, 1672.

(201) Kayana, K.; Okayama, S. *J. Phys. D Appl. Phys.* **1972**, *5*, 43.

(202) Cao, J.; Chen, Z.; Xu, J.; Wang, W.; Chen, Z. *Electrochim. Acta* **2013**, *88*, 184.

(203) Mountjoy, G. *J. Non-Cryst. Solids* **2001**, *295*, 458.

(204) Schlögl, R. *Adv. Catal.* **2009**, *52*, 5.

(205) Kaneko, K.; Kosugi, N.; Kuroda, H. *J. Chem. Soc., Farady Trans.* **1989**, *85*, 869.

(206) Siani, A.; Captain, B.; Adams, R. D.; Alexeev, O. S.; Amiridis, M. D. *Top. Catal.* **2011**, *54*, 318.

(207) Mukerjee, S.; Srinivasan, S.; Soriaga, M. P.; Mcbreen, J. *J. Electrochem. Soc.* **1995**, *142*, 1409.

(208) Gasteiger, H. A.; Kocha, S. S.; Sompalli, B.; Wagner, F. T. *App. Catal., B* **2005**, *56*, 9.

(209) Gómez, R.; Orts, J. M.; Álvarez-Ruiz, B.; Feliu, J. M. *J. Phys. Chem. B* **2004**, *108*, 228.

(210) Srejić, I.; Smiljanić, M.; Rakočević, Z.; Štrbac, S. *Int. J. Electrochem. Sci.* **2011**, *6*, 3344.

(211) Duchesne, P. N.; Chen, G.; Zhao, X.; Zheng, N.; Zhang, P. *J. Phys. Chem. C* **2014**, *114*, 28861.

(212) Toda, T.; Igarashi, H.; Watanabe, M. *J. Electroanal. Chem.* **1999**, *460*, 258.

(213) Liu, G. C.-K.; Sanderson, R. J.; Vernstrom, G.; Stevens, D. A.; Atanasoski, R. T.; Debe, M. K.; Dahn, J. R. *J. Electrochem. Soc.* **2010**, *157*, B207.

(214) Atkins, P.; de Paula, J. In *Physical Chemistry*; W.H. Freeman and Company: New York, 2006; pp 1005–1006.

(215) Zhang, P. *J. Phys. Chem. C* **2014**, *118*, 25291.

(216) Lingane, J. J. *J. Am. Chem. Soc.* **1939**, *61*, 2099.

(217) Bonakdarpour, A. A Combinatorial Study of Pt-Based Oxygen Reduction Electrocatalysts for Hydrogen Fuel Cells, Dalhousie University, 2007.

(218) Song, C.; Zhang, J. In *PEM Fuel Cell Electrocatalysts and Catalyst Layers*; Springer: London, 2008; pp 91, 113.

(219) Mehta, V.; Cooper, J. S. *J. Power Sources* **2003**, *114*, 32.

(220) Takasu, Y.; Ohashi, N.; Zhang, X.-G.; Murakami, Y.; Minagawa, H.; Sato, S.; Yahikozawa, K. *Electrochim. Acta* **1996**, *41*, 2595.

(221) Duchesne, P. N.; Zhang, P. *J. Phys. Chem. C* **2014**, *118*, 21714.

(222) Huber, G. W.; Iborra, S.; Corma, A. *Chem. Rev.* **2006**, *106*, 4044.

(223) Wasmus, S.; Ku, A. *J. Electroanal. Chem.* **1999**, *461*, 14.

(224) Wanjala, B. N.; Fang, B.; Luo, J.; Chen, Y.; Yin, J.; Engelhard, M. H.; Loukrakpam, R.; Zhong, C.-J. *J. Am. Chem. Soc.* **2011**, *133*, 12714.

(225) Wang, X.; He, B.; Hu, Z.; Zeng, Z.; Han, S. *Sci. Technol. Adv. Mater.* **2014**, *15*, 43502.

(226) Zhang, Q.; Xie, J.; Liang, J.; Lee, J. Y. *Adv. Funct. Mater.* **2009**, *19*, 1387.

(227) Zhang, Q.; Lee, J. Y.; Yang, J.; Boothroyd, C.; Zhang, J. *Nanotechnology* **2007**, *18*, 245605.

(228) Verbruggen, S. W.; Keulemans, M.; Martens, J. A.; Lenaerts, S. *J. Phys. Chem. C* **2013**, *117*, 19142.

(229) Liz-Marzán, L. M. *Mater. Today* **2004**, *7*, 26.

(230) Wu, C. W.; Mosher, B. P.; Lyons, K.; Zeng, T. F. *J. Nanosci. Nanotechnol.* **2010**, *10*, 2342.

(231) Padmos, J. D.; Langman, M.; MacDonald, K.; Comeau, P.; Yang, Z.; Filiaggi, M.; Zhang, P. *J. Phys. Chem. C* **2015**, *119*, 7472.

(232) Wawro, A.; Sobańska, M.; Petroutchik, A.; Baczewski, L. T.; Pankowski, P. *Nanotechnology* **2010**, *21*, 335606.

(233) Finetti, P.; Dhanak, V. R.; Binns, C.; Edmonds, K. W.; Baker, S. H.; D'Addato, S. *J. Electron Spectros. Relat. Phenomena* **2001**, *114–116*, 251.

(234) Kong, D.; Wang, G.; Pan, Y.; Hu, S.; Hou, J.; Pan, H.; Campbell, C. T.; Zhu, J. *J. Phys. Chem. C* **2011**, *2*, 6715.

(235) Zhong, X.; Yu, H.; Wang, X.; Liu, L.; Jiang, Y.; Wang, L.; Zhuang, G.; Chu, Y.; Li, X.; Wang, J. *Appl. Mater. Interfaces* **2014**, *6*, 13448.

(236) Dai, Y.; Wang, Y.; Liu, B.; Yang, Y. *Small* **2015**, *11*, 268.

(237) Wang, C.; Yang, M.; Flytzani-Stephanopoulos, M. *AIChE J.* **2016**, *62*, 429.

(238) Kim, J.; Jung, C.; Rhee, C. K.; Lim, T. *Langmuir* **2007**, *23*, 10831.

(239) Kraft, S.; Stümpel, J.; Becker, P.; Kuetgens, U. *Rev. Sci. Instrum.* **2001**, *67*, 681.

(240) Bearden, J. A. *Rev. Mod. Phys.* **1967**, *39*, 78.

(241) Blizanac, B. B.; Arenz, M.; Ross, P. N.; Markovic, N. M. *J. Am. Chem. Soc.* **2004**, No. 15, 10130.

(242) Hamelin, A.; Ho, Y.; Chang, S.; Gao, X.; Weaver, M. J. *Langmuir* **1992**, *8*, 975.

(243) Spendelow, J. S.; Xu, Q.; Goodpaster, J. D.; Kenis, P. J. A.; Wieckowski, A. *J. Electrochem. Soc.* **2007**, *154*, F238.

(244) Cheng, J.; Hu, P. *J. Am. Chem. Soc.* **2008**, *130*, 10868.

(245) Neurock, M.; Janik, M.; Wieckowski, A. *Faraday Discuss* **2008**, *140*, 363.

(246) Cuesta, A.; Lanova, B.; Baltruschat, H. *Langmuir* **2009**, *25*, 6500.

(247) Liu, J.; Lucci, F. R.; Yang, M.; Lee, S.; Marcinkowski, M. D.; Therrien, A. J.; Williams, C. T.; Sykes, E. C. H.; Flytzani-Stephanopoulos, M. *J. Am. Chem. Soc.* **2016**, *138*, 6396.

(248) Liu, H.; Ye, F.; Yao, Q.; Cao, H.; Xie, J.; Lee, J. Y.; Yang, J. *Sci. Rep.* **2014**, *4*, 3969.

(249) Yuge, K.; Koyama, Y.; Kuwabara, A.; Tanaka, I. *J. Phys. Condens. Matter* **2014**, *26*, 355006.

(250) Atienza, D. O.; Allison, T. C.; Tong, Y. J. *J. Phys. Chem. C* **2012**, *116*, 26480.

(251) Zhang, J.; Asakura, H.; van Rijn, J.; Yang, J.; Duchesne, P.; Zhang, B.; Chen, X.; Zhang, P.; Saeys, M.; Yan, N. *Green Chem.* **2014**, *16*, 2432.

(252) Chen, G.; Zhao, Y.; Fu, G.; Duchesne, P. N.; Gu, L.; Zheng, Y.; Weng, X.; Chen, M.; Zhang, P.; Pao, C.-W.; Lee, J.-F.; Zheng, N. *Science* **2014**, *344*, 495.